Óbuda University

PhD Thesis

Investigation of optrodes for infrared stimulation in the deep tissue

HORVÁTH, Ágoston Csaba MSc electrical engineer

Supervisor: FEKETE, Zoltán PhD

Doctoral School on Materials Sciences and Technologies

Head of the Doctoral School: RÉGER, Mihály, Dsc

Budapest, April 2020.

Contents

1 Preface

1.1 Motivation and goals

The development of deep-brain implants that are simultaneously able to monitor neural activity and to stimulate the same tissue environment is advantageous to gain comprehensive information on the behaviour of cooperating neuronal population. Means of modulation of neuronal activity are acting through electrical [1], [2], [3], [4], [5], pharmacological [6], [7], [8], [9], [10] or optical intervention [11], [12], [13]. Among clinically relevant stimulation methods [1], [14], [15], photo stimulation is a promising tool, since electrical crosstalk effects, which contaminates recorded brain signals during electrical stimuli, are limited [16]. The most often used technical term for these devices, which can deliver light to neurons and can record evoked potentials, is optrode [17], [18]. A special field of optical neuromodulation applies infrared (IR) light for several beneficial reasons [19]. It is simple, as does not require any genetic transformation [20]; its longer wavelength provides superior penetration in tissues [21] and facilitates artefact-free recording of electrophysiological signals [22], [23]. During my PhD work, I developed a single-crystalline silicon-based, Michigan-type (in-plane) IR optrode capable for simultaneous deep-brain electrophysiological recording and temperature sensing (see Fig.1.). Although the discovery of IR-induced modulation of cellular activity dates back to the early 2000s, such an integrated, multimodal, long neural probe has never been created. Thanks to this compact investigation tool, further knowledge about the interaction of IR light and deeper regions of the neural tissue can be extended *in vivo* in a minimally invasive way.

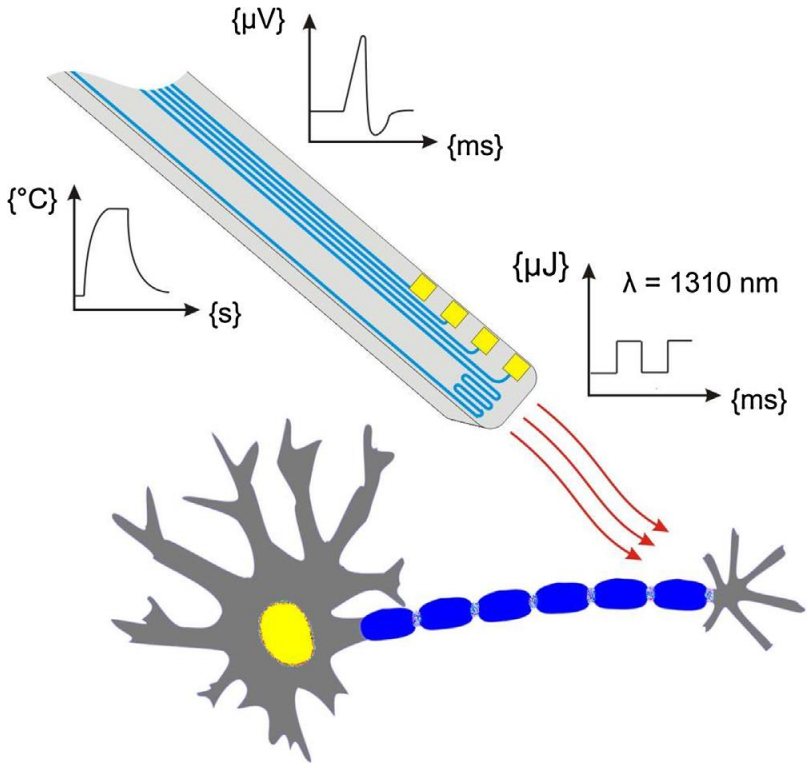

Figure 1: Concept of the multimodal optrode developed during my PhD work. [24]

1.2 Structure of the dissertation

At the beginning of my dissertation I give an overview of related fields in the literature of neural microdevices. I briefly introduce some neuroscientific aspects of the applications and the contemporary opportunities of the rich field of implantable neural microdevices with integrated optics. Then I sum up the mechanism of optical and thermal stimulation methods of the nervous system. I introduce the optrode device through the description of its expected functionalities and the details of its design and fabrication process. All of the fulfilled test methods of the optrode's functionalities are also introduced: benchtop tests of the device development, calibrations of individual products, functional tests *in vitro* and *in vivo* validation as well. I discuss the results in separate subchapters comparing to the literature, and my related theses are highlighted at the end of the chapters. Another separate chapter is devoted to the application opportunities and benefits related to the optrode in question. At the end of the dissertation there are the lists of the cited literature, my publications and appendices containing supplementary figure and data, and the explanation of the used acronyms.

2 Introduction to neural microdevices

Neural microdevices can be classified based on various aspects: e.g. human or animal purpose; central or peripheral nervous system is targeted; chronic or acute, cortical or deep-tissue application. They can provide sensing or stimulating functions or both. The final applications mentioned below require different approaches relying on the use of a wide variety of materials and structural layout. The following literature overview of implantable microdevices will focus on some of the relevant efforts from literature that are closely related to the topic of my PhD work.

2.1 Biomedical MEMS and neuromodulation

MEMS is the acronym of micro electro-mechanical systems. MEMS devices are manufactured using semiconductor technology, which is also used to produce integrated circuits. MEMS devices are often made of silicon (Si) or at least their fabrication process relies on silicon microtechnology. MEMS technology offers high precision, and therefore fine features in device layout due to advances in processes like photolithography, thin film deposition and etching [25], [26], [27], [28], [29]. Further advantage of such micromachining approach is that batch fabrication provides several devices with low variability in characteristics at relatively low unit cost [28], [29]. Before the advent of MEMS in the biomedical field, several material and manufacturing process were proposed depending on the targeted surgical application. First deep-brain implants were made from metal wires (like tungsten or stainless steel) to monitor the extracellular electrical activity in neurophysiology experiments [30]. Since then, additional technologies have emerged in this field, e.g. silicon-based microelectrodes [31], [32], [33] and polymer electrode arrays [34], [35]. The essential capability of these microimplants is the interrogation of neurons through tiny arrays of recording sites (e.g. circular, 15 μm diameter [36], [35] or 10×10 μm^2 rectangular Au recording sites [33]). Brain functions have been researched for many decades and although amazing results have been achieved in many areas, a number of mechanisms inside this complex organ remained unclear. Neural signals that are usually recorded by the most commonly applied probes are interrogating a couple dozens of neurons, however there are billions of neurons in the brain. In order to get more detailed knowledge especially about more comprehensive, general brain functionalities and

correlations, larger number of individual neurons needs to be simultaneously monitored. That is the reason why the combination of CMOS and MEMS technologies have been proposed to construct high-density electrode arrays [37], [38]. Beyond this important neurophysiological functionality, integrated modalities like drug delivery [39], [40], neurochemical sensing [41], [42] and optical stimulation [43], [44] are emerging extensions on such devices, which offer a novel toolset in the microscale investigation of cellular process. Local drug delivery is used for example to treat a tumour [45], meningitis, ventriculitis, and central nervous system associated infections [46]. Neurochemical sensing focuses on the observation and investigation of neurotransmitters (e.g. dopamine) to gain useful information also for further treatments [41], [47], [48], [42]. Optical neuromodulation methods also represent an emerging technology, and will be introduced in more details in later chapters. Although not all of the followings can be integrated into needle-like microdevices, I briefly refer to additional neuromodulation techniques. Electrical neuromodulation as a symptomatic treatment of Parkinson's disease (PD), called deep brain stimulation (DBS), is a success story of the field. The technique relies on a stimulator probe implanted permanently into the brain tissue, and an external device, which delivers current pulses in a pre-defined sequence to terminate tremor [49]. The implanted electrodes of DBS devices cause a potential gradient across a neuron, which leads to intracellular ionic current flow and localized depolarization and hyperpolarization of the cell membrane. This way, a region of cell membrane hyperpolarization is created, which is sufficient to block action potential propagation, thereby achieving neural inhibition. Briefly, stimulation appears to block the signals that cause disabling motor symptoms, and so helps to provide greater control over movement. In case of transcranial magnetic stimulation (TMS) potential gradients are induced in the tissue by a rapidly changing strong magnetic field (>1 T). The design of a micro-TMS system has been recently reported which reduces the spatial resolution by an order of magnitude [50]. Nevertheless, the large power consumption is still a limitation not yet overcome by fully implantable stimulator. Several other experiments have indicated that temporally modulated ultrasound waves can elicit action potentials in brain cells [51]. Their method is called transcranial ultrasound stimulation. Up to now, very little is understood about mechanobiology of affected cells, although proposed mechanisms have included cavitation and thermal effects. Of course,

each approach has advantages and disadvantages, so to make a reasonable solution for a particular neuromodulation, one is facing with trade-off.

2.2 Implantable microdevices with integrated optics

In literature, the comprehensive name of implantable devices what can deliver light to neurons and electrically recording them is ‘optrode’ [17], [18]. Before optrodes have been introduced, bulky optical fibres implanted in the tissue were only used to stimulate neuronal population using light in spatially confined manner [52], [53], [54], [55]. The key advantage of optrodes is that they provide multiple functions in a single device, which helps to mitigate the extent of cellular damage otherwise induced using standalone recording and stimulation devices. Such multifunctional tool also provides precise relative location of recording and stimulation spots eliminating the complicated positioning of individual devices [56]. The state-of-the-art optrodes can be divided in two main groups: passive and active optrodes (cf. Fig. 2. A-B and C-D, respectively). Passive optrodes contain a passive microoptical element, which delivers light coupled into the system from an external light source (optical fibre, waveguide). In active optrodes, light is generated through integrated sources (like microLEDs) located on the probe [57], [13], or even on its shaft [58], [59], [60]. In this chapter, technology of passive optrodes is briefly described using specific examples from the literature. Figure 2 depicts main constituent parts of optrode devices in schematics.

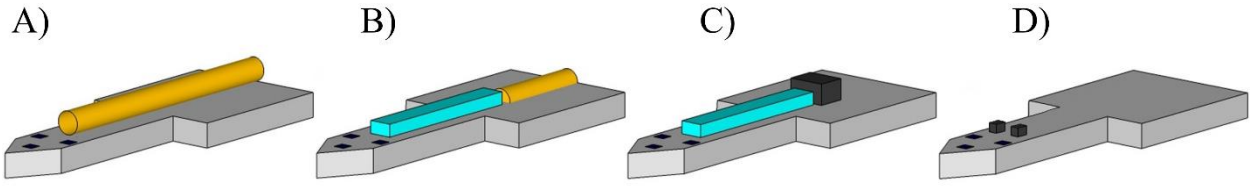

Figure 2: (a) Optical fibre (yellow) affixed to the substrate (grey) of the passive optrode. (b) Optical fibre coupled to the surface waveguide (cyan) structure of the passive optrode. (c) Integrated light source (black) coupled to the surface waveguide structure of the active optrode. (d) Light sources integrated on the penetrating shaft of the active optrode. Based on the Fig. 4. in [30].

The aim of the first approaches was to supplement conventional in-plane (Michigan-type) silicon microelectrodes with secondary waveguiding structures. Royer et al. combined multiple-shank silicon probes with thinned optical fibres fixed on each shank [61]. Their

method incorporates standard glass optical fibres into the technology of planar silicon microelectrodes to form integrated waveguides on the probe shaft (see Figure 3 a&b). The inherent drawback of this technique was that the overall size of the implant was pretty bulky. To circumvent this, wet chemical (with KOH [62]) or dry (deep reactive ion etching – DRIE [63]) etching techniques were used to form a groove in the Si substrate to embed the fibre into the bulk (see Figure 3 c).

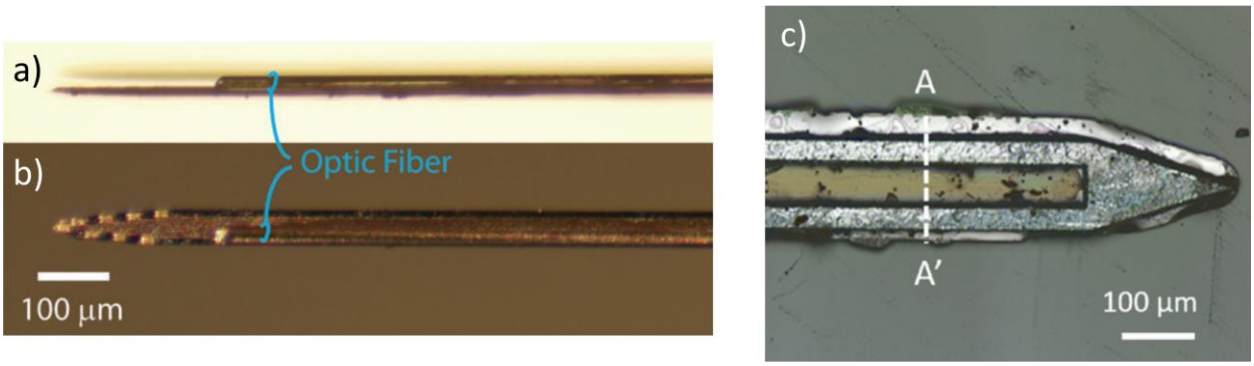

Figure 3: (a) Side and (b) front view images of electrode shanks with a glued optical fibre [61]. *(c) Photograph of the fabricated Si optoneural probe tip with the optical fibre embedded in a probe shank* [63].

Cho et al. used SU-8 polymer as the core of the integrated micro-waveguide on the top of the conventional passivation SiO_2 layer on the microelectrode's shaft (Figure 4 [64]). The advantages of this method were to downscale the waveguide dimensions and to provide a more accurate positioning with respect to the probe tip and to the recording sites. Kobayashi et al. used silicon-nitride as the core of the integrated micro-waveguide similarly on the top of the SiO_2 passivation layer [65], however, in this case, the top cladding was also a SiO_2 layer, not only the surrounding air. Although, they applied thinner layers even for the core and for the cladding, the entire implant diameter was wider, because their probe was designed with a longer shaft, which required more robust substrate. Wu et al. chose silicon-oxynitride as core material instead of SU-8 polymer or SiN (Figure 5 [66]). They also applied SiO_2 as cladding layer completely surrounding the core. All group realized the coupling between the light source and the integrated waveguide with butt-coupling of an optical fibre [64]–[66] or simply butt-coupled a laser diode right to the embedded fibre [62]. The precise positioning of the coupling fibre in the first cases was ensured by a DRIE-etched fibre guiding groove.

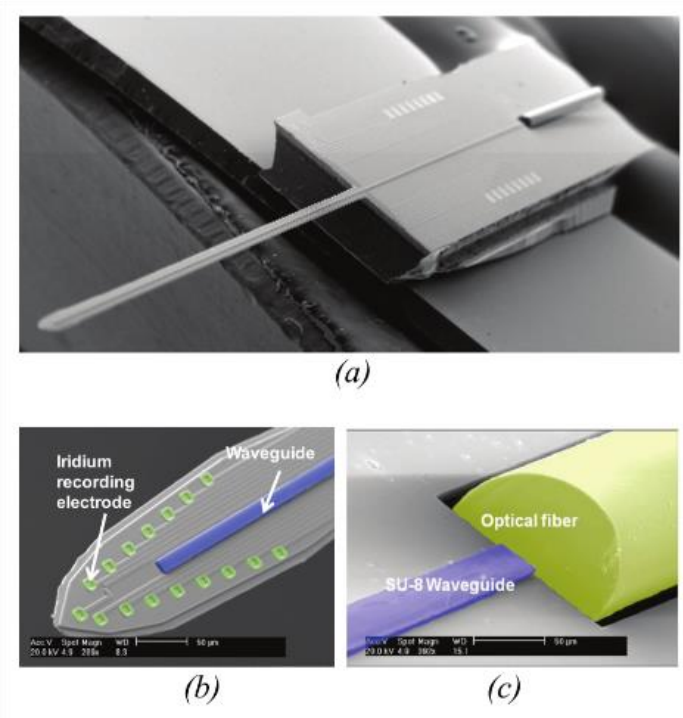

Figure 4: (a) SEM overview of the neural probe with optical fibre mounted at the end of the SU-8 waveguide. (b) Iridium electrode array around stimulation site. (c) Coupling between optical fibre and waveguide [64]

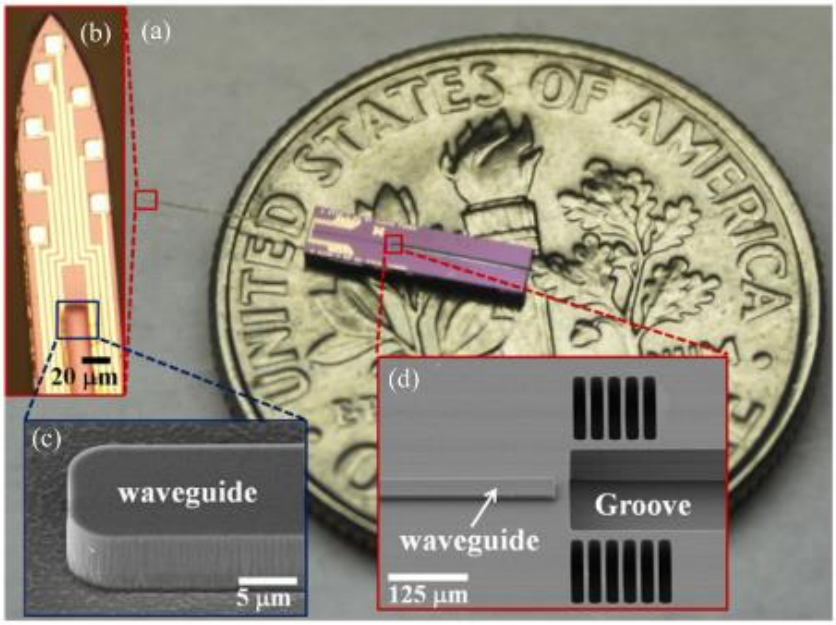

Figure 5: (a) Relative size in contrast with a US quarter. (b) Microscope image of probe tip showing the electrode array and the SiON waveguide. (c) SEM image of the waveguide magnified at the distal end. (d) SEM image of the waveguide at the proximal end and the optical fibre groove [66].

Lee's and Abaya's work present another approach: out-of-plane microprobe arrays [67], [68]. Lee et al. chose ZnO as the substrate material because of its physical properties, suitability for device microfabrication and biocompatibility. ZnO is transparent across the visible spectrum into the near-infrared range, nontoxic and biocompatible. They generated square pillar arrays by means of mechanical dicing. Later, they tapered these square pillars by a custom developed multistep chemical etching process. For electrical isolation, first they sawed trenches into the substrate and filled them with medical-grade polymer adhesive, then each pillar was coated with Parylene C. The refractive indices of these two materials are $n_{ZnO} \approx 2.0$ and $n_{Parylene} \approx 1.6$. To form electrical contact to the brain tissue, they removed the Parylene C to expose the tips of the optoelectrodes, then finally they sputtered a thin transparent conductive layer of indium-tin-oxide (see Fig. 6.). This device is able to perform simultaneous light delivery and electrical readout thanks to the optically transparent and electrically highly conducting semiconductor behaviour of the ZnO crystal. Note, that this waveguide optrode array is used for optogenetic application with a 473 nm blue laser.

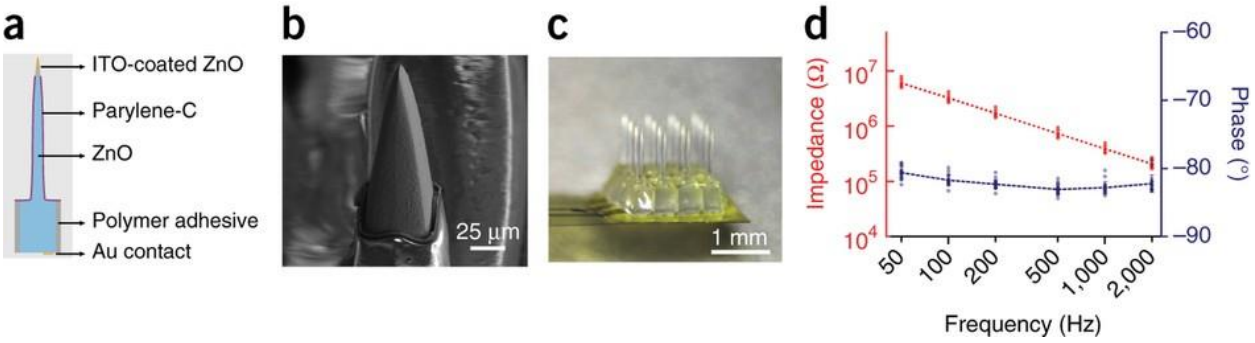

Figure 6: Transparent, electrically conductive ZnO micro-optoelectrode array (MOA device) for multichannel intracortical neural recording and optical stimulation. (a) A single optoelectrode structure. The ZnO shank is electrically isolated by Parylene-C except for the active tip area, and shanks are isolated from each other by polymer adhesive. (b) Electron microscope image of the microscopically smooth tip with the recording area, covered by a final ITO conducting overlayer. (c) A 4 × 4 MOA device flip-chip bonded on thin, flexible and semitransparent polyimide electrical cable. (d) Electrical impedance spectroscopy of MOAs (n = 18) with uniform impedance across the arrays. [67]

Abaya et al. took advantage of the experience gathered during the development of the Utah Slant Electrode Array (USEA). They tapered the pre-sawed silicon pillars with wafer-scale wet chemical etching in a 1:19 acid mixture of HF (49%) and HNO_3 (69%). They also

realized the coupling between the light source and each waveguiding silicon cone with butt-coupling of an optical fibre. In most cases, refractive index matching material is also used between the fibre's end and the polished (flat) backside of the silicon array. Note, that this device is the first written development of an optrode array made for deep brain infrared neural stimulation (INS), however, their system is only a technological demonstration, and was never applied in living tissue.

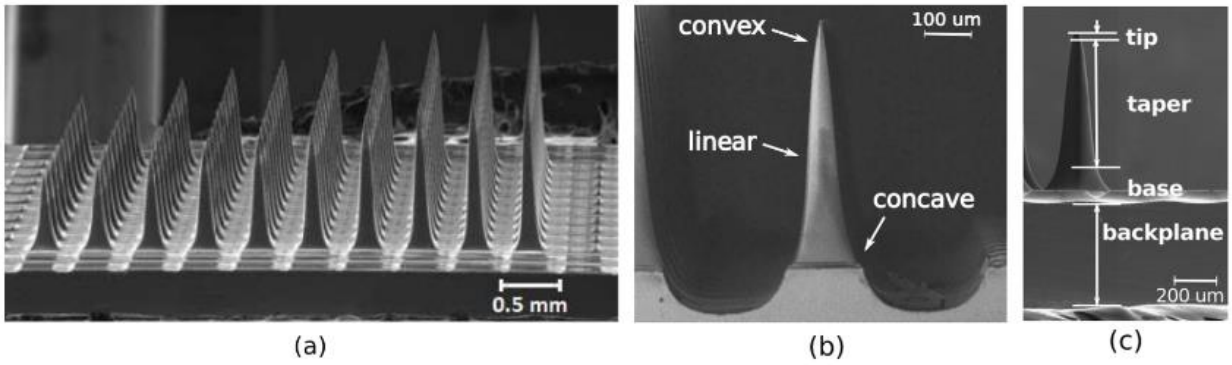

Figure 7: SEM images of a Utah Slant Optrode Array. The array is bulk-micromachined from intrinsic (100) silicon. (a) Optrode lengths vary from 0.5 to 1.5 mm. (b) Taper profile of the shortest optrode. (c) Definition of optrode sections along the path of light propagation: 500 µm backplane, base extending 120 µm into linearly tapered shank, and ~50 µm tip. [68]

2.3 Optical stimulation methods

Typically, optrode devices are used for optogenetic applications (see Fig. 8.). This method incorporates genetic modification of specified neurons making them sensitive to certain coloured (visible) light radiation [18]. The popular set of wavelength used in optogenetic applications: 405 nm [44] or 473 nm [52], [61], [69] (blue), 561 nm [61] (yellow-green) or 635 nm [44] (red).

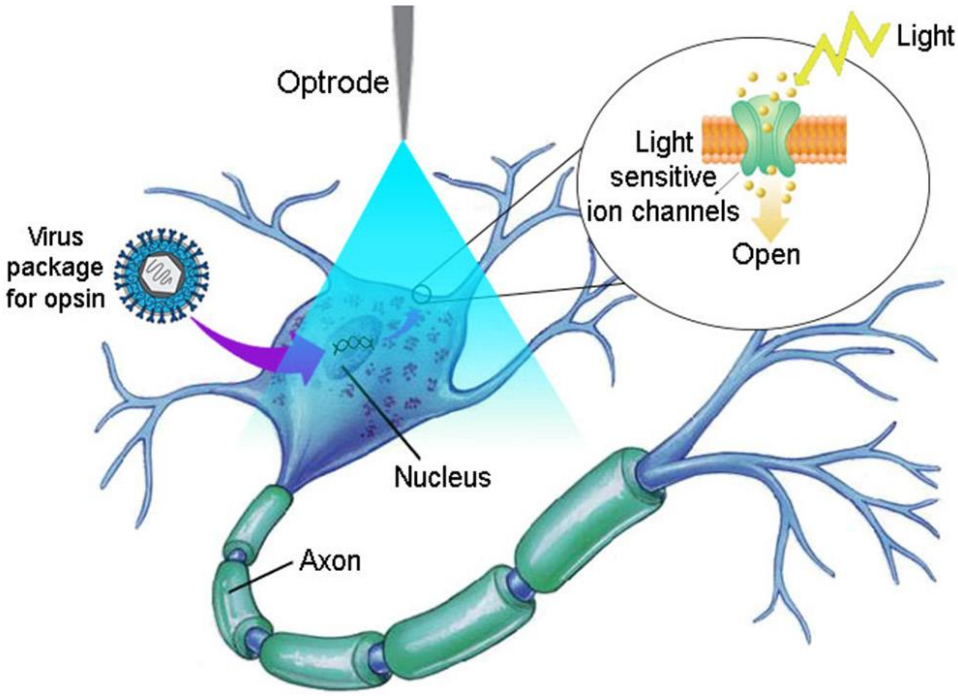

Figure 8: Illustration of the optogenetic technique using a blue light, which activates ChR2-expressing neuron cells by opening light sensitive ion channels [18].

Generally, optogenetics integrates light-sensitive proteins (opsins) into the cell membrane of specific cell types to form light-sensitive ion channels that can modulate action potential generation. Controlled operation of specific ion channels can be realized by illumination with a suitable coloured light depending on the opsin's type. Simply, one can 'switch' on and off specified neurons by specified light. The main advantages of this method are its temporal and spatial precision: it is a fast, local and selective investigation tool in cellular level. However, its application in human targets is still challenging. However, there are ethical concerns because of the risks of genetical modification, there are few pioneering research of translational aims. There is an active clinical study on optogenetic vision restoration (NCT02556736) in the USA. Besides ethical issues, optogenetics entails the disadvantage of complexity of an additional time consuming and expensive procedure using genetic tools. Optogenetics has also another disadvantageous property: the typically used visible wavelength light causes artefact (noise) in the recorded neurophysiological signals [69]. It is originated from the photoelectric effect (Becquerel effect), when photons of a suitable frequency light eject an electron from a metal by striking it. The presence and movement of these generated electrons are similarly detected as electrical signal

superimposed on the electrophysiological recording. Alexandre Edmond Becquerel was who first observed the phenomenon in 1839, but Albert Einstein was who explained it in 1905. When light of a particular frequency strikes a metal surface, electrons are ejected. In that case, increasing the intensity only increases the number of electrons ejected. If the frequency is increased, the ejected electrons will travel faster. This is described by the equation:

$$E = h \cdot \nu \geq h \cdot \nu_0 = \Phi \qquad (1)$$

where E is the energy of the incident photon, h is Planck constant, ν is frequency of the light, ν_0 is the light frequency threshold necessary to generate photocurrents and Φ is the photoelectric work function. For most biomedical applications and neural technologies, frequency (ν) and wavelength (λ) can be equated through the formula ν = c/λ, where c is the speed of light. [70].

A special method, exploiting the produced light-sensitivity of neurons, is a widespread example of the application field known as two-photon imaging. The method is based on a quantum mechanical phenomenon: the energy of the light-matter interaction required for excitation can be obtained not only from a single photon, but also from two photons absorbed at the same time, each having half (or even less) of the energy required [71]. In case of multi-photon events, equation (1) can be rewritten as:

$$E_N = (N + S) \cdot h \cdot \nu \qquad (2)$$

where N is the number of photons colliding with the electron at the same time and S is a positive integer [72]. For example, 11 Hz two-photon raster scanning with a 30 mW, 920 nm laser increased the spiking activity of soma-targeted ChR2-expressing neurons in the mouse neocortex *in vivo* [73].

Another optical method, that does not need any genetical modification induces change in the thermal conditions in the tissue to modulate neurons [74]. This method uses longer wavelength light in the infrared regime (1400–2100 nm). Its one advantage is that the use of longer wavelength reduces the possibility of photoelectric effect [70]. Another key advantage is that IR stimulation does not require any genetic modification [20]. High

energy (0.3–0.4 J/cm^2 at 1.87 and 2.1 μm [75]) IR light pulses (micro- to milliseconds) generate temperature transients (spatial and temporal) in neurons depolarizing their cell membrane and making them firing action potential [20]. Besides, the application of IR light in neural subjects has further capabilities: lower energy IR illumination was described as a mean of neural inhibition. Its background is summarized in next chapter.

2.4 Thermal stimulation

Infrared neural stimulation was initially achieved through the generation of spatial and temporal gradient in tissue temperature, which required high energy, custom designed lasers with low repetition rate. Later, it was discovered that low energy (0.050±0.012 J/cm^2 [76]) irradiation can be also efficiently used. The effect of lower energy IR light is different than that of the high energy IR pulses. It is proved that IR illumination with lower radiant exposure than applied for stimulation caused reversible inhibition of action potentials, both their propagation and their generation [77]. Its mechanism is supposed as an effect of elevated background temperature [78]. The non-uniform rate increases in temperature-dependent Hodgkin-Huxley gating mechanism is the hypothesis proposed recently [79] suggesting that higher temperature activates the voltage-dependent K^+ channels faster, resulting sufficiently greater hyperpolarizing current to overcome depolarization [80]. Another experiment proves that the thermal sensitivity of certain ion channels of neurons (TRPV4) plays a fundamental role in stimulating effect of IR illumination [81]. Although, the ion channels from the TRP family of cation channels are expressed in almost every tissue and cell type [82], another method, called thermogenetics, also plans transgenic application of foreign temperature-sensitive ion channels for controlling neurons' behaviour. Despite the promising results already reported in Drosophila [83], in mouse [84] and in zebrafish [85], thermogenetics is still in its infancy. There is already a limited variety of ion channels suitable for application, especially in mammalian targets [85]. Besides the already mentioned disadvantage of genetic modification, thermogenetics is suitable in view of invasiveness of the stimulating method: as visible light required for optogenetics has to be delivered through a transcranial waveguide element, thermal "signals" can be delivered in a non-invasive way through external stimulus. Its simplest way is ambient warming which is lacking cell specific selectivity. Through the application of magnetic nanoparticles [86] what well absorb microwave/radiofrequency radiation, the spatial resolution of the

externally forced local tissue heating can be improved. The main disadvantages of these types of thermal stimulation methods are their temporal resolution and power consumption. IR illumination is still promising, because rapid heating can be achieved and its penetration depth in tissues is more favourable than visible light's one [21], [87]. Although penetration depth of light is strongly wavelength-dependent [88] and also depending on the examined tissue, effective deep-brain application of IR light still needs penetrating waveguides (cf. Fig. 9.).

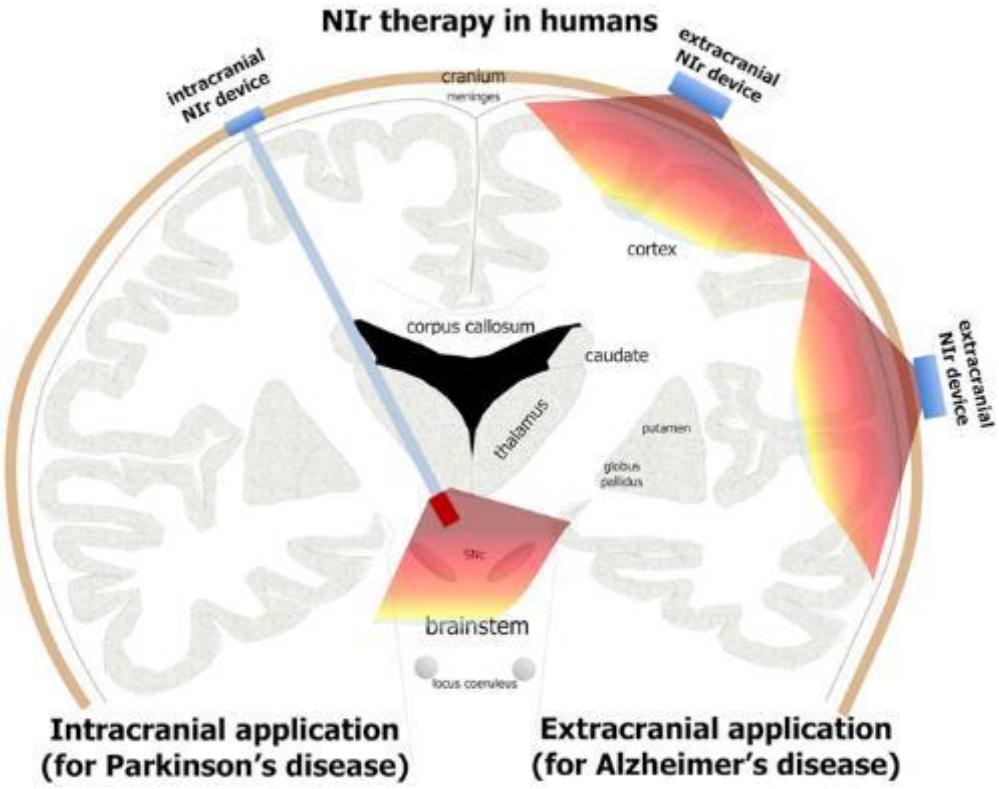

Figure 9: Potential applications of near infrared (NIr) illumination in Alzheimer's and Parkinson's patients. Cortical layers can be reached extracranially, deep regions require intracranial devices. [89]

Since we discussed above heat induced neuromodulation techniques, we should not miss to mention thermal issues of the introduced optical methods. It was already mentioned above in this section that IR irradiation is purposefully applied for elevating the background temperature of the target tissue to achieve neuromodulation effect [76], [90], [91]. In cases where IR light is used for multi-photon excitation or imaging, so not for the purpose of heating, IR irradiation still has heating effect: in a study, where 920 nm CW

(continuous wave) illumination was probed, a ~1.8 °C/100 mW peak temperature increase was experienced [92]. Similarly, optical neuromodulation techniques that use visible light also have a thermal effect on the irradiated volume. A $\Delta T = 2$ °C general limit is defined for the temperature rise of the outer surface of an implanted (medical) device with respect to the surrounding body temperature of 37 °C (cf. ISO 14708-1 standard). To meet this requirement, Schwaerzle et al. operated the red light-emitting (650 nm) integrated laser diode of their two-shank Si implant in pulsed mode. During a 25 s long 35 mA laser drive with a 100 kHz pulsing (duty cycle = 5%) the maximum temperature rise was 1 °C [57]. For the same purpose, Wang et al. also tested the driving parameters of the blue light-emitting (445 nm) laser diode integrated in their neuro-implantable device. They stated that the temperature rise increased with duty cycle and its upper limit is 10% when the driving current and the frequency are 100 mA and 10 Hz, respectively [13]. Although a standard acceptable heating limit has been set, brain researchers dealing with optical radiation of the tissue should also consider whether the effects induced / observed are indeed (only) a consequence of photosensitivity or perhaps a rise in temperature or the combined effect of the two.

3 Experimental

3.1 Design

The aim of the present device development was to create an implantable optical stimulation device, which is able to deliver IR light through its embedded bulk waveguide and holds sensors, which monitor the optically evoked electrical and thermal response of the irradiated tissue. Device concept is shown in Figure 10. IR light is coupled from an optical fibre positioned close to a cylindrical coupling lens integrated in the optrode chip. After coupling, IR light is propagating through total internal reflection inside the probe shaft and exits the shaft at the end facet. The absorbed light is converted to heat, and the evoked change in cellular activity and tissue temperature is recorded through integrated sensors. Since this goal requires a complex approach in view of microtechnology, I first addressed this issue by testing individual functionalities in two particular dummy structures. Electrical recording sites and temperature sensors without optical functionality was realized and will be referred to as thermoelectrode [93]. The waveguiding modality of the device concept was first tested using optical dummy samples, where the silicon substrate

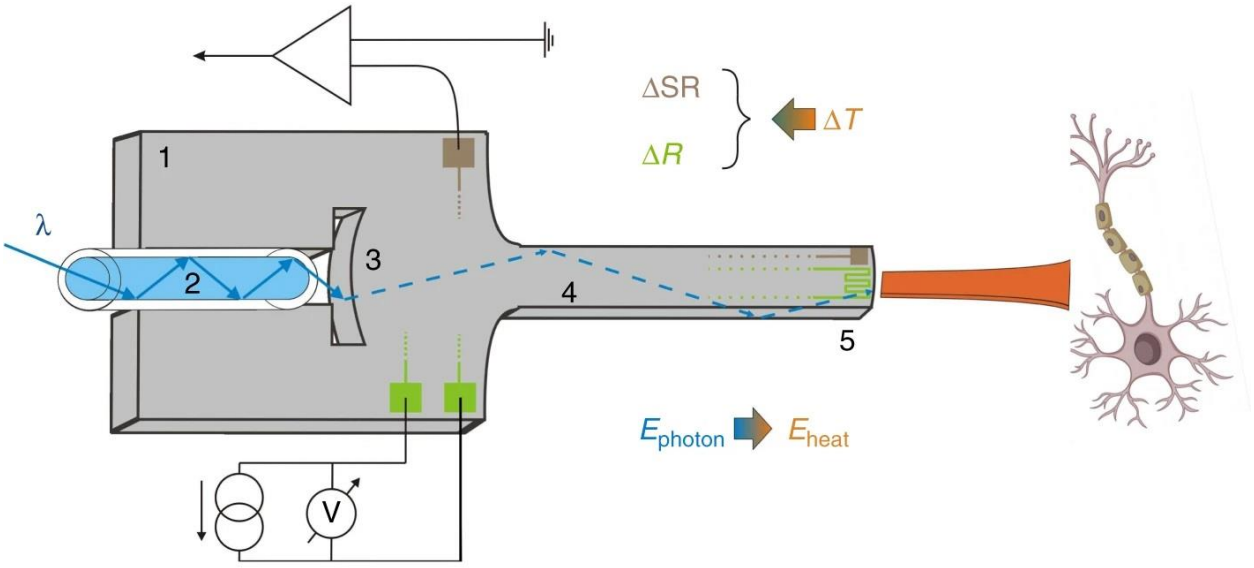

Figure 10: Schematic of the multimodal IR neural microsystem. Marked components: 1: Si substrate, 2: multimode optical fibre, 3: cylindrical coupling lens, 4: shaft with multiple functionalities, 5: probe tip. Figure is not to scale. ΔSR and ΔR mean that optically induced temperature elevation changes the detectable spike rate of the affected neurons and the ohmic resistance of the integrated temperature sensor. [95]

itself is used not only as the mechanical carrier, but also as an infrared waveguide thanks to special wet etching process developed by group members in a prior work [94].

To test the waveguide efficiency of the optrode two types of dummy samples were fabricated. Bare silicon chips without any thin film layer on top and with a 200 nm thick silicon-nitride layer on one (top) side. This pair of sample enables the investigation of the effect of the passivating layer on waveguiding efficiency, since prior work was only limited to Si optrode chips without dielectric thin films. Relevant parameters of the dummy chips are shown on Figure 11 A&B:

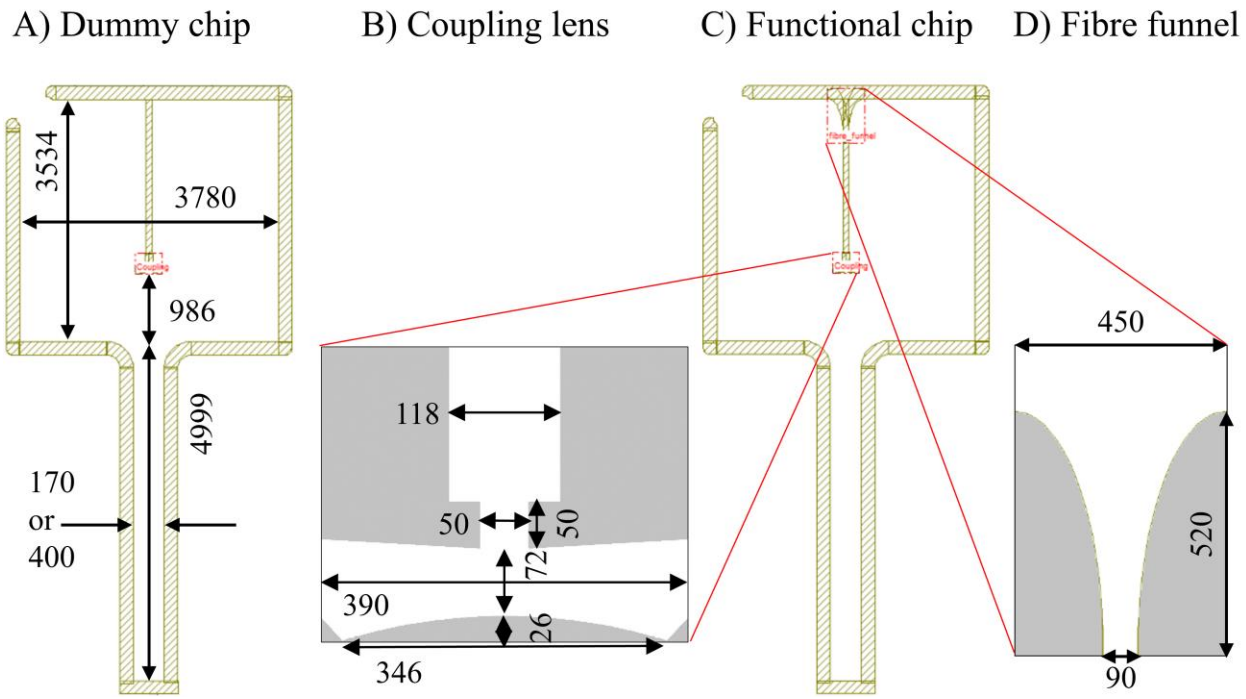

Figure 11: Schematics of optrode chip designs. A) Contour of optical dummy chip with coupling lens. B) Design of coupling lens. C) Contour of functional optrode chip with coupling lens and funnel-shape extension of fibre guide groove. All geometric dimensions are the same as in case of optical dummies (A), but only with thinner shaft (170 µm). D) Design of funnel-shape extension of fibre guide groove's inlet. All marked geometric dimensions are in [µm].

Based on the experiences and results I composed these aforementioned devices into one multimodal microsystem. The contour of optical dummy samples (Figure 11 A) and functional optrode chips (Figure 11 C) is the same. Both have a quadratic backbone and an elongated shaft. The backbone part will hold the bonding pads ensuring further connection of measuring wires and it incorporates a linear groove with a cylindrical lens ending (Figure

11 B). This groove is for embracing the optical fibre which delivers IR light from the source. The cylindrical lens ending is intended to support good efficiency light coupling from optical fibre to Si waveguide: two fenders help keeping the proper distance between the end facet of optical fibre and the front of the lens which focuses the incident light beams to the shaft. Functional optrode chip version's layout is supplemented with a funnel shape (Figure 11 D) at the beginning of the fibre guide groove: it makes optical fibre insertion easier in practice. Unlike optical dummy samples, on the top side of functional chips there is not only a SiN layer (as in certain cases), but a sputtered platinum (Pt) thin-film packaged within a dielectric layer structure of silicon-dioxide and silicon-nitride (see Fig. 12.). The electrophysiological recording sites are formed as 30×30 μm^2 Pt squares placed nearby the tip of the shaft, at a distance of 100 or 300 µm from each other. The thermal sensor, which is a meander-shape Pt wire on the same layer, is placed as close as possible to the recording sites ensuring true local thermal information during experiments (see Figure 13 & 33).

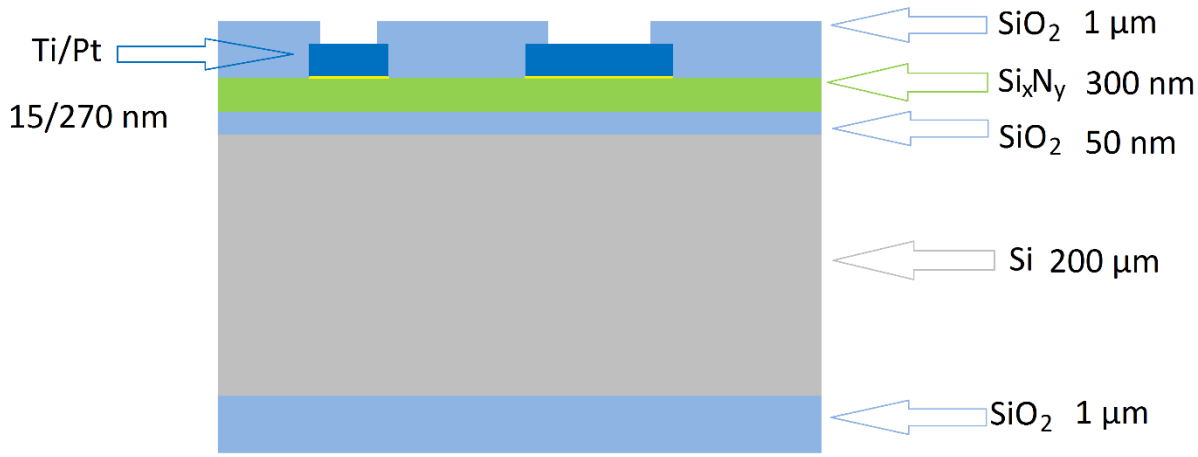

Figure 12: Cross sectional schematic of a functional optrode chip showing the layer structure with corresponding thicknesses (cf. Fig. 15.). Image is not to scale. [96]

The blunt tip of above design is advantageous regarding the optical characterization of the device, as the relevant optical information comes from a single plane and makes preliminary measurements easier to implement. Obviously, the penetration of the final device into the tissue is easier and induces less tissue damage if sharp tip design is applied, but in my initial experiments this particular shape was sufficient to test all functionalities in a reproducible manner either before or during *in vivo* application.

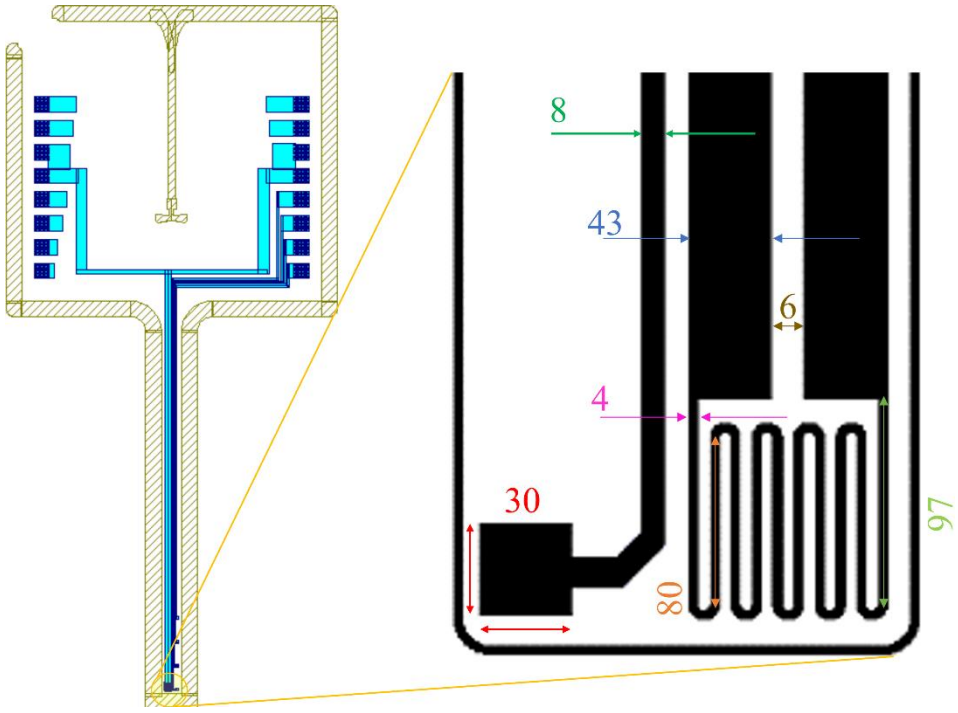

Figure 13: Schematic of the design of functional chip with magnified view of the tip. All marked geometric dimensions are in [µm].

3.2 Microfabrication

In the following section, the process steps of engineering three particular samples will be describe: dummy samples that do not hold any other functionalities on top of light delivery; thermoelectrodes that hold all integrated functionalities except for light delivery; fully functional optrodes capable of light delivery, electric and thermal recording. However, each approach contains some similarities in certain phases of technology, I explain all details at each device configuration to give a comprehensive information, which helps to understand the underlying procedures of microfabrication. Si MEMS technology was chosen since it has been developed and improved for decades. Besides its many advantages, it may have inherent properties, that are not so beneficial for device fabrication. For instance, the sidewalls of out of plane structure are difficult to fine-tune. To overcome this drawback, wet chemical methods provide additional freedom to polish these surfaces. That is why I complemented the fabrication sequences going to be described in the followings with further wet chemical steps.

3.2.1 Optical dummy samples

The initial substrate was a 200 µm thick single-crystalline silicon wafer. Double-side polished wafers were used to maximize the efficiency of the integrated Si waveguide by maintaining the atomic smoothness of the wafer surface. A 200 nm thick low-stress silicon nitride (SiN_x) film was deposited in an LPCVD chamber (Tempress Systems, Inc., Netherlands) at 830 °C and 200 mTorr. This single layer was chosen to anticipate the effect of the further functional layer structure on IR waveguiding. The gas flow rate of H_2SiCl_2 and NH_3 was 160 sccm and 20 sccm, respectively. Residual contaminants were removed in a rinser dryer. Then a 400 nm thick APCVD oxide (SiO_2) layer was deposited as a masking layer of further patterning of the nitride. After a 30 min annealing, the oxide was patterned by photolithography on the front side to open windows for nitride etching. After the etching of SiO_2 by diluted HF, the photoresist (PR) was removed in acetone bath (step 1 in Fig. 14.).

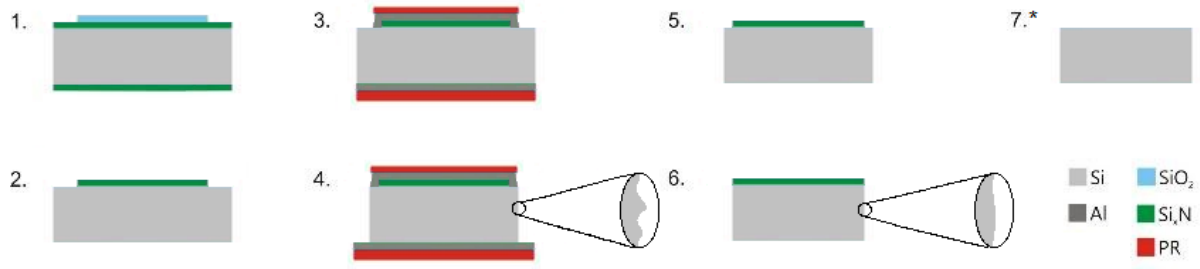

Figure 14: Micromachining steps of optical dummy samples. (1) Si_xN deposition, CVD SiO_2 masking Si_xN patterning; (2) Nitride etching; (3) Al mask photolithography for DRIE; (4) Through-wafer DRIE forms the chip's contour and the fibre guide groove; (5) Removal of Al and PR layers; (6) Wet chemical polishing. (7) Optional nitride etching. Top-side nitride-covered dummies made by applying steps (1)–(6). Bare Si optical dummy samples made by applying steps (1)–(7*).*

The non-masked nitride surfaces were removed by wet etching in phosphoric acid, then the SiO_2 mask was also removed (step 2 in Fig. 14.). Wet etching was used in both cases of oxide and nitride etching instead of dry etching to maintain the smoothness of the backside surface of the Si wafer, because wet etching removes materials selectively while dry etching is less selective and its mechanism of action includes physical 'bombing' of accelerated ions which does not respect material boundaries. A 300 nm electron-beam evaporated Al layer and additional PR cover (1.8 and 4.5 µm on front and backside,

respectively) were used as hard mask and etch stop of the electrode-shape release technique, the dry etching, using Bosch recipe in an Oxford Plasmalab System 100 DRIE chamber (Oxford Instruments Plc, UK). Chamber pressure was 30 mTorr, inductively coupled plasma power (ICP) was set to 750 W, C_4F_8 and SF_6 flow rate were 100 sccm and 150 sccm, respectively. The duration of etch and passivation cycles were 4 and 9 s, respectively (step 3-4 in Fig. 14.). Finally, masking layers were removed in acetone and in nitric acid (step 5 in Fig. 14.). Fluorocarbon polymer inherently deposited on the trench sidewall during Bosch-process was removed in a high-temperature oven at 600 °C in O_2. The planarization of the probe sidewall was achieved by immersing the wafer in a polishing mixture of HF : HNO_3 : H_3PO_4 in a ratio of 1 : 8 : 1 at 20 °C for 2 min 40 s (etch rate: 9-10 µm/min) (step 6 in Fig. 14.). This microfabrication process was supplemented with another nitride etching in phosphoric acid, only in case of bare Si samples (step 7* in Fig. 14.).

3.2.2 IR optrodes

The initial substrate was a 200 µm thick p-type (100) single-crystalline silicon wafer. Double-side polished wafers were used to maximize the efficiency of the integrated Si waveguide by maintaining the atomic smoothness of the wafer front- and backside surface. Wet oxidation of silicon wafers was performed at 1100 °C. 50 nm thick thermal SiO_2 layer was grown on the substrate surface. To further isolate the recording sites from the bulk Si, a 300 nm thick low-stress silicon nitride (SiN_x) film was deposited in an LPCVD chamber (Tempress Systems, Inc., Netherlands) at 830 °C and 200 mTorr (step 1 in Fig. 15.). The gas flow rate of H_2SiCl_2 and NH_3 was 160 sccm and 20 sccm, respectively. The SiN_x and SiO_2 were removed from the backside of the wafer by wet etching in phosphoric acid and diluted HF, while front side layers were protected by low temperature oxide and SPR 4.0 photoresist (step 2–4 in Fig. 15.). Wet etching was used instead of dry etching to maintain the smoothness of the backside surface. A sacrificial Al layer was used to define the pattern of the TiO_x/Pt recording sites, temperature monitoring filament and wires via a standard lift-off process (step 5 in Fig. 15.). First, a 300 nm thick sacrificial Al layer was deposited by electron beam evaporation. This was followed by the first photolithography step using Microposit 1818 photoresist (Rohm and Haas Company, USA), and etching steps defining the inverse pattern of the conductive layers. The conductive layers consisted of a 15 nm

thick adhesion layer of TiO_x formed by reactive sputtering of Ti in an Ar/O_2 atmosphere (Ar/O_2 ratio was 80 : 20). 270 nm thick Pt was sputtered on top of TiO_x. The deposition of the two layers was performed in a single vacuum cycle using a DC Magnetron sputtering equipment (Leybold GmbH, Germany). To complete the lift-off process step, photoresist and Al were removed in acetone and in nitric acid, respectively. In the next fabrication step, the top passivation layer of 1000 nm thick SiO_2 layer was deposited using LPCVD at 430 °C in a gas mixture of SiH_4 and O_2 (step 6 in Fig. 15.). Contact and bonding sites were exposed by additional photolithography (Microposit 1818 photoresist) and dry etching step through a 100 nm thick aluminium hard mask (step 7 in Fig. 15.). Dry etching of the $SiO_2/SiN_x/SiO_2$ dielectric stack was performed in an Oxford Plasmalab 100 DRIE chamber using fluorine chemistry (step 8 in Fig. 15.). 200 nm SiN_x as a masking layer for wet chemical polishing was deposited again in the LPCVD system using the above parameters (step 9 in Fig. 15.). The probes were then micromachined by dry etching using Bosch recipe in an Oxford Plasmalab System 100 DRIE chamber (Oxford Instruments Plc, UK). Masking layer was e^--beam evaporated aluminium on the front side, while bottom SiO_2/SiN_x stack acted as etch stop layer. A protective 4 μm thick photoresist layer was also utilized on the backside of the wafer (step 10–11 in Fig. 15.). Chamber pressure was 30 mTorr. ICP power was set to 750 W, C_4F_8 and SF_6 flow rate were 100 sccm and 150 sccm, respectively. The duration of etch and passivation cycles were 4 and 9 s, respectively. Finally, masking layers were removed in acetone and in nitric acid (step 12 in Fig. 15.). Fluorocarbon polymer inherently deposited on the trench sidewall during Bosch-process was removed in a high-temperature oven at 600 °C in O_2. The planarization of the probe sidewall was achieved by immersing the wafer in a polishing mixture of $HF : HNO_3 : H_3PO_4$ in a ratio of 1 : 8 : 1 at 20 °C for 2.5 min (etch rate: 9-10 μm/min) (step 13 in Fig. 15.). The low-temperature oxide membrane at the bottom of the trenches was dissolved in buffered oxide etchant, then top and bottom SiN_x protective layer was also removed completely in phosphoric acid (step 14 in Fig. 15.).

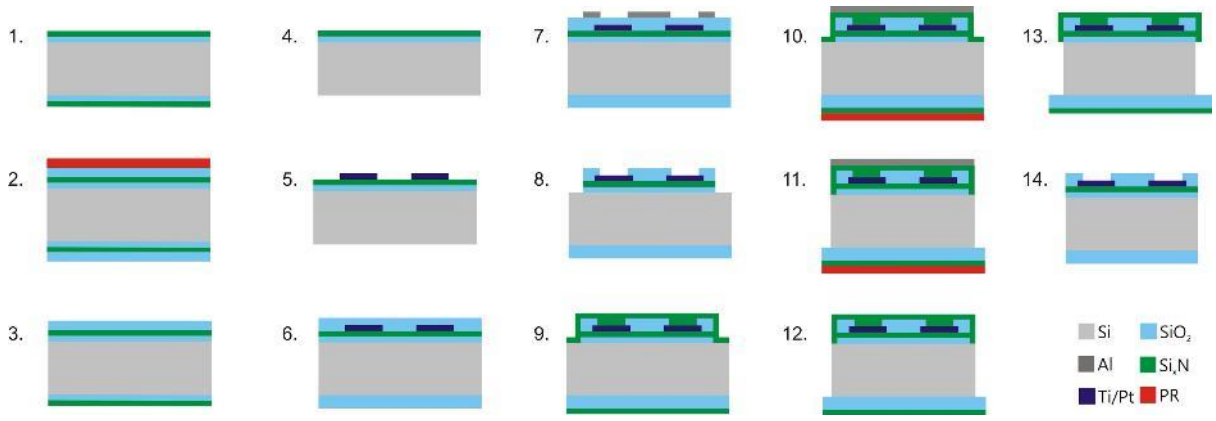

Figure 15: Fabrication sequence of fully functional optrodes. (1) SiO_2 and SiN deposition, (2) LTO deposition and front-side photoresist protection, (3) HF etch and PR removal, (4) Backside nitride and oxide removal, (5) Ti/Pt deposition and lift-off, (6) LTO deposition, (7) Deposition, photolithography and etching of Al mask for DRIE, (8) Dielectric stack removal in DRIE and Al removal in wet etchant, (9) SiN deposition, (10) Deposition, photolithography and etching of Al mask for DRIE with backside PR protective layer, (11) Deep silicon etching in DRIE, (12) Removal of Al mask and protective PR layer, (13) Wet chemical polishing, (14) HF etch and SiN removal in phosphoric acid. [24], [97]*suppl.*

3.3 Packaging

After the microfabrication process, individual optrode chips were packaged to make optical and electrical connections to external light sources for stimulation and to amplifiers for neuronal recording and temperature monitoring on a custom-designed PCB, manufactured by Solutions System Ltd. First, in the middle line of the PCB a 400 μm deep trench was milled (step 2 in Fig. 16.). The aim of this trench is to bridge the height difference between the middle axis of the silicon chip and that of the optical fibre. This trench also helps to position the core of the stripped optical fibre into the guiding groove of the chip in a well-aligned fashion. The Si chip was then fixed with a double-sided adhesive tape (step 3 in Fig. 16.). It makes wire bonding and later the precise fibre positioning easier. Connection between the electrode bonding pads and the PCB leads was made using ultrasonic wire bonding (Kulicke-Soffa Industries, Inc., Singapore) utilizing 25 μm thick gold microwires (step 4 in Fig. 16.). The properly stripped and polished fibre was inserted into the chip's groove (step 5 in Fig. 16.). In the groove, the fibre facet was fixed with index-matching glue (n = 1.56; Norland Products Inc., Cranbury, NJ, USA) which, in addition, helps to prevent contamination of the coupling area (step 6 in Fig. 16.) and improves the overall waveguiding efficiency. After UV light cure of the optical adhesive (25 min) the PCB was

mounted with PreciDip connector (Preci-dip SA, Switzerland) for providing electrical connection to external amplifiers to be used during electrochemical impedance spectroscopy tests and *in vivo* experiments. This through-hole socket also helps to keep the fibre along the PCB in a fixed position, and also reduces the sensitivity of the fibre to external mechanical impacts during surgery. Remaining gaps and connection points are filled with Araldite® 2014 adhesive (Huntsman Advanced Materials, Switzerland) to increase mechanical strength of the device (step 7 in Fig. 16.).

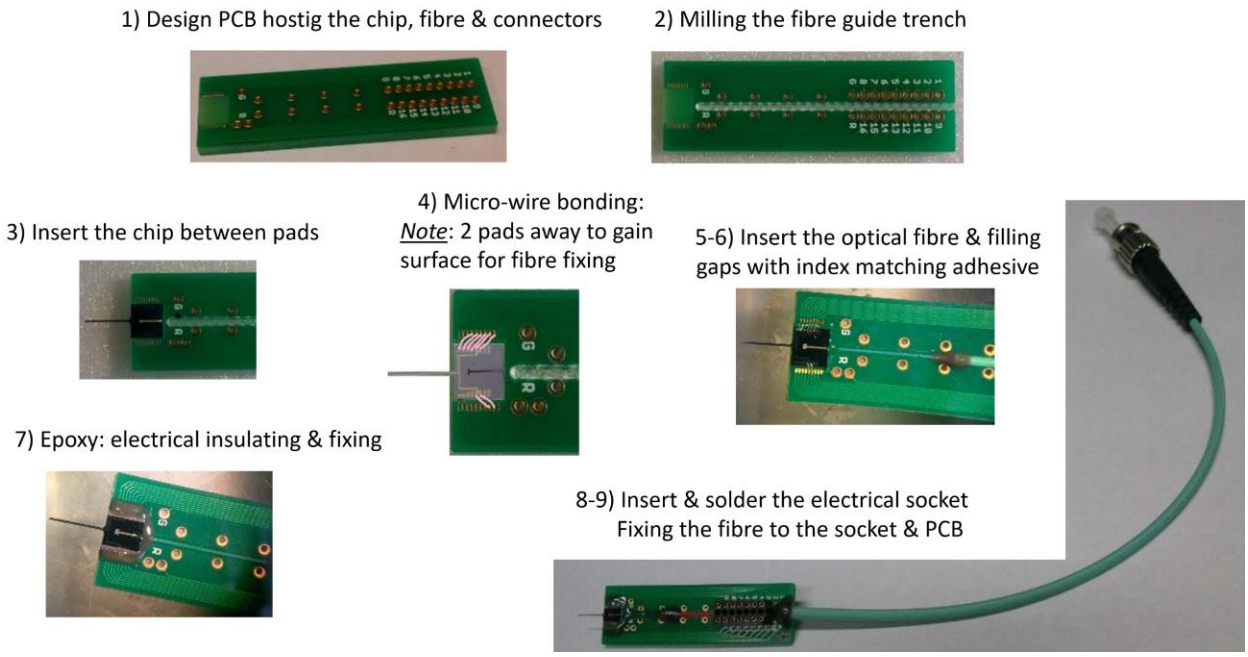

Figure 16: Main steps of IR optrode assembly.

As it was mentioned above, the selected optical fibre must be prepared properly preceding the assembly. First, the fibre is cleaved to the desired length. Then, most importantly, we must polish the fibre's end facet to create a perfect light emitting surface. Another task is to strip the fibre's furcation tubing and inner tube (protective polymer coatings around the fibre) to provide sufficient amount of stripped fibre protrusion for the insertion into the groove of the chip. During the project related to the device development, I tested three different optical fibre types. All of them was multimode optical fibre (NA = 0.22). I started working with one mounted with an LC connector, with 50 µm core and about 120 µm overall diameter (NewNetwork Ltd., Hungary). This connector type was found too prone to wobble what adversely affected the waveguiding measurements. So, I changed it with

another one mounted with an ST connector, with the same core/cladding ratio and diameter (FibreFab Ltd., UK). Later, I changed it with a fibre type with a wider, 105 µm core and about 125 µm overall diameter mounted with an SMA connector (Thorlabs Inc., USA). These latter types of fibre have a wider furcation tubing to bear the heavier bayonet style (ST) or screw-type (SMA) connector. To avoid an unintended crack of optical fibres, the electrical socket was inserted in a distance of two pins (raster: 1.27 mm) from the edge of the PCB. Thanks to this additional surface, the furcation tubes can be adhered directly to the surface of the PCB and to the orthogonal side of the socket (step 9 in Fig. 16.). This robust fixing helps to avoid the bending of the fibres around a too short radius. Because of the mentioned positioning of the socket, the microwire bonding also had to follow the modification of the pinout (cf. step 4 in Fig. 16.). During the application of the first run of optrode chips, I noticed that depending on the etch time of wet chemical polishing of the chip's sidewall, not all the optical fibres fitted to the guiding groove of the chip perfectly. To circumvent this issue, I thinned the cladding of the fibres to the desired diameter before polishing their end facet. Using 50±1% buffered HF at room temperature (21–21.9 °C), I determined the etch of the cladding material, and performed the thinning of the cladding, if demanded. Relevant etch rates were 3.1 µm/min for FibreFab OM3 fibres, and 4.4 µm/min for Thorlabs M15 fibres. Because this HF etching not only thinned the cladding, but etched a bit the core material as well, it had to precede the abovementioned essential polishing of the fibre's end facet.

3.4 Compliance with the requirements and constraints

- Acute *in vivo* functional test of the optrode device in rat somatosensory cortex and hippocampus: shaft length = 5 mm
- Easy pre-calibration of individual modalities (waveguiding, temperature sensing, neural recording)
    - Optical aspects
        - Symmetry: square waveguide cross section
        - Acceptable efficiency
            - Smooth sidewalls: double-side polished wafer + wet chemical polishing

        - A lens focusing the light emitted from the fibre on the waveguiding shaft
      - Easy optical characterization → single emitted beam → blunt tip
    - Thermal aspects
      - Local temperature measurement
      - Simple, but robust construction

      → Single resistance thermometer as close to the tip as possible
    - Aspects of neural recording
      - Small dimensions
      - Multi-channel recording capability

      → 4 rectangular recording sites as close as possible to the tip, made of the same material as the integrated thermometer, within the same technological layer
      - Reduction of signal-to-noise ratio: reduction of the impedance of the recording sites
- Reasonable minimization of the cost of all constituents at this early stage of research
    - Si wafer: double-side polished, sufficiently thin (not too thick), available in the market by default → 3", p-type, 200 μm thick, double-side polished wafers with <100> crystallographic orientation, produced by the Czochralski method
    - Connectors and sockets for measurement wirings: not too small for frequent manual handling, not too large for *in vivo* use, available in the market by default: PreciDip
    - Optical fibre: not too thick / thin, not too fragile, multimode, available in the market by default → with different connectors: 1.: LC, 2.: ST, 3.: SMA

3.5 Electrochemical characterization

Before *in vivo* investigations, it is essential to analyse the electrical performance of devices. On one hand, the long-term integrity of the layer structures should be tested in wet environment. This is usually referred as soaking test in the literature. On the other hand, the characteristic property of the recording sites is investigated using Bode plots recorded

in the frequency range relevant to applications in the brain tissue (1 Hz – 10 000 Hz) [98]: the typical range of local field potential (LFP) is 1–300 Hz [99], while spikes (often referred as single or multiunit activity (SUA/MUA)) are detected at higher frequencies between 300–10 000 Hz. Electrochemical impedance spectroscopy is a popular tool to provide information in this respect [100], [101], [102].

3.5.1 Electrochemical impedance spectroscopy

Electrochemical impedance spectroscopy (EIS) method uses a three-electrode cell. The schematic and a photo of the arrangement can be seen in Fig. 17.B&A, respectively. When voltage is applied between the reference (R) electrode (maintained at a constant potential) and the so-called working electrode (W/WS), it generates charge transport (electric current) between the W/WS and the so-called counter (C) electrode, and EIS measurement computes impedance values using these two measures, the present voltage and current.

After the immersion of an electrode in an electrolyte, the arrangement seems electroneutral, because the immediately occurred chemical reactions quickly reaches a steady state equilibrium. EIS method slightly moves away the arrangement from this equilibrium because of an applied AC excitation. The aim of it is that the expected ion and solvent transport from the electrolyte to the conductive film is not significant, so the morphological and electrochemical transformation of the film is negligible. Common evaluation of EIS is finding the lumped-parameter equivalent circuit model of the observed setup [103], [104], [105]. Another practice refers the hole characteristic with one measure, the amplitude value of the impedance at 1 kHz [106], [107].

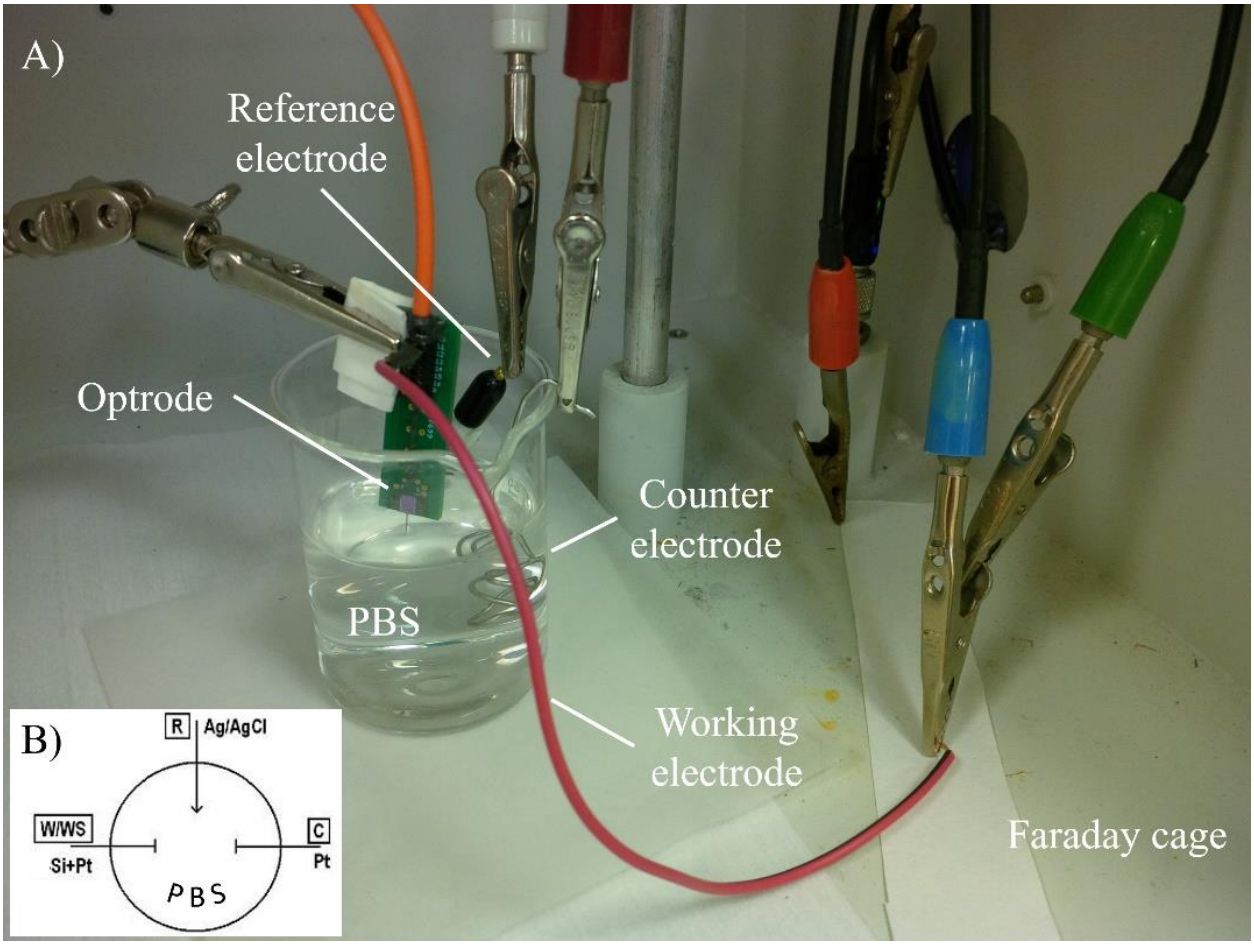

Figure 17: (A) Photo and (B) schematic of 3-electrode setup for electrochemical inspection of recording sites.

In the lab of the Institute of Technical Physics & Material Sciences, Centre for Energy Research (EK MFA) I used a Gamry Reference 600 potentiostat (Gamry Instruments, PA, USA). The applied electrolyte medium of my experiments made in a Faraday cage was phosphate buffered saline (PBS; 0.01 M). The reference electrode was a leakless Ag/AgCl (3.4 mol/L KCl) electrode, the counter electrode was a Pt wire and each of the Pt electrophysiological recording sites was connected as a working electrode. Gamry Framework 6.02 software was used for automated control of measurement and recording, and Gamry Echem Analyst 6.02 was used for data evaluation. The applied AC voltage was 25 mV_{RMS}, the frequency range was set between 1 Hz to 10 kHz.

3.5.2 Electroplating

Just before *in vivo* application, the impedance of the electrophysiological recording sites was reduced by electroplating porous Pt (or sometimes referred as black-Pt). This

additional porous layer on the top of the Pt recording sites increases their specific surface area. The aim of it is to improve the SNR performance of the recording modality. Thermal noise is one of the most common sources of noise in recordings [108], [109]. It is caused by the thermally induced random motion of charge carriers (mainly electrons) in the conductor material [110], [111]. Its calculation formula is:

$$V_{RMS} = \sqrt{\sum_{freq.} 4kTR\Delta f}, \qquad (3)$$

where k is Boltzmann constant, T is absolute temperature, R is the resistive component of the impedance and Δf is the bandwidth of frequencies to be considered. As the formula implies, reduction of the impedance may have beneficial effect on noise reduction, consequently on SNR.

The schematic and a photo of the arrangement of electroplating can be seen in Fig. 18.B&A, respectively. I used the same Gamry Reference 600 potentiostat in galvanostatic mode. The electrolyte medium was a solution of lead free 1 m/m% chloroplatinic acid (H_2PtCl_6; source of extra Pt atoms on recording sites' surface) and povidone ($(C_6H_9NO)_n$; PVP; improving wettability of flat Pt surfaces). The counter electrode – refilling Pt atoms in the solution – was a Pt plate. The reference electrode was the same leakless Ag/AgCl electrode. The electroplating process lasted 60 seconds, whilst the current density was maintained at 10 mA/cm^2. Each recording site to coat was connected individually to the cell as working electrode. The aim of it was to reduce the variability of site impedances as low as possible. During electroplating the parallel position of the plane of the Si chip (recording sites) and the Pt plate results similar even deposited layer thickness on each site. The resulted black-Pt coverage was kept in aqueous medium (like PBS) to maintain the beneficial characteristics along the further experiments. On one hand its wet character is essential to retain the increased specific surface area, on the other hand dry black-Pt structure easily peels off from the device surface.

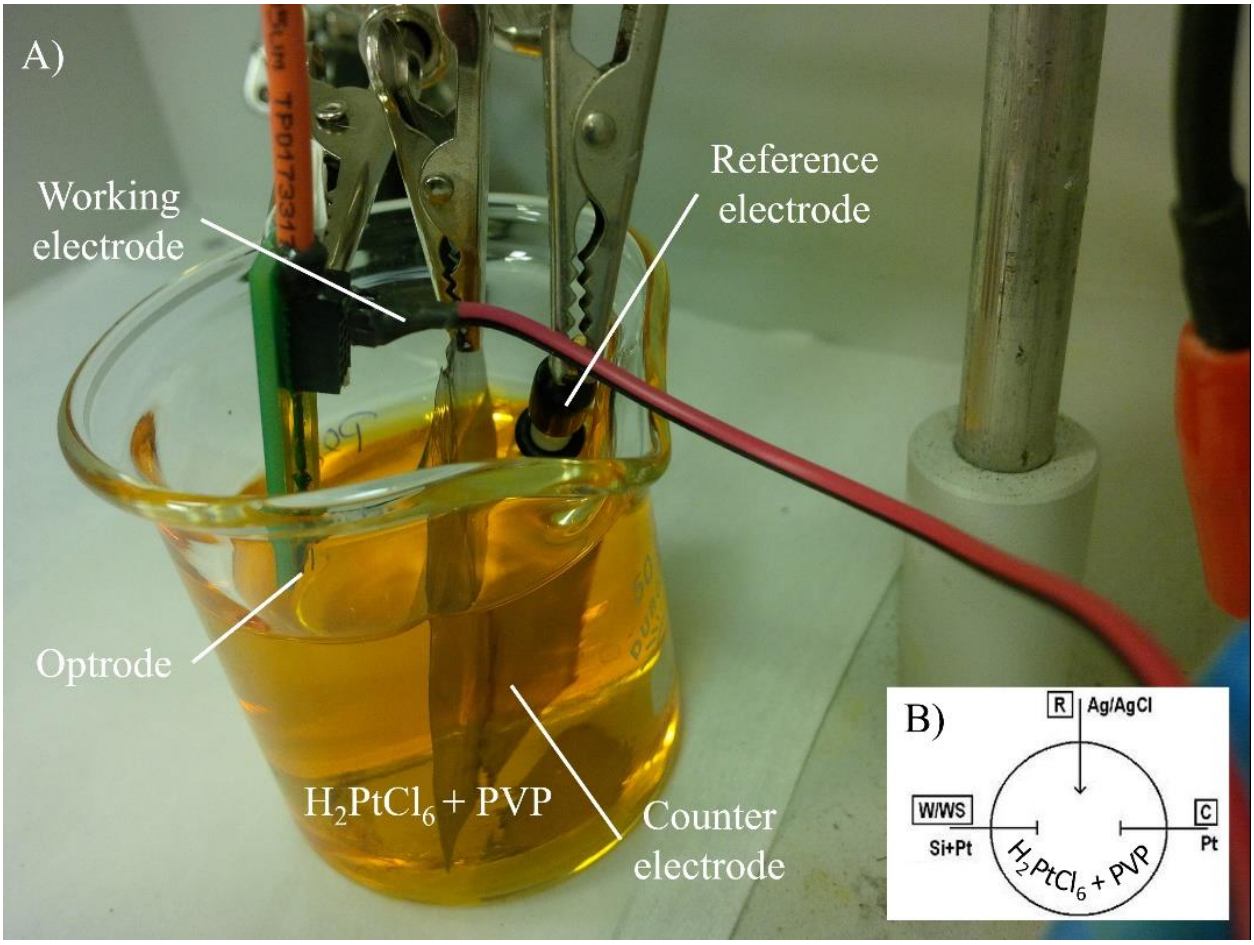

Figure 18: (A) Photo and (B) schematic figure of 3-electrode setup for electroplating platinum-black layer on top of recording sites. Platinum recording sites represent the working electrodes, while a platinum sheet is used as counter electrode.

3.6 Optical characterization

In this chapter, I introduce the experiments to determine the optical properties of the optrode. During my work, I used two measurement setups. One of them relies on a CMOS beam profiler (CinCam CMOS-1.001-Nano, CINOGY Technologies GmbH, Germany), which was used to evaluate the shape of the IR light emitted from the tip of the optrode. The other one comprises of a laser power meter (FieldMaxII-TOP with an OP-2 IR Ge sensor head, Coherent Inc, CA, USA), which provided quantitative information on optical power. During the four years of my PhD work, I used four different types of IR laser light sources. All of them was a laser diode operated in constant current (continuous wave, CW) mode. In the initial stages an un-cooled, 5 mW diode (S1300-5MG-FW, Roithner LaserTechnik GmbH, Austria) was chosen. Later, when higher light intensity was required,

it was replaced with a 30 or 40 mW Roithner laser diode (RLT1300-30G, RLT1300-40G). The latter types needed cooled environment, so they were placed in a custom designed Al holder (see Fig. 19.C), which also supported the focusing and collimation of IR light to the front facet of the optical fibre. All Roithner laser diodes operate at wavelength of 1310 nm. The fourth IR light source is a pigtailed laser diode (LPSC-1550-FG105LCA-SMA, Thorlabs Inc., USA) with 50 mW and 1550 nm operating power and wavelength, respectively. Pigtailed laser diode means that one gets the laser diode assembled with an optical fibre. The appropriate alignment of fibre and diode is carried out in the fab, and this best position was fixed. This type of laser also needs cooling, which was realized in this case by a simple, custom Al cooling flag. The opposite end of the fibre of this light source is mounted with an SMA optical connector to facilitate the coupling to another fibre.

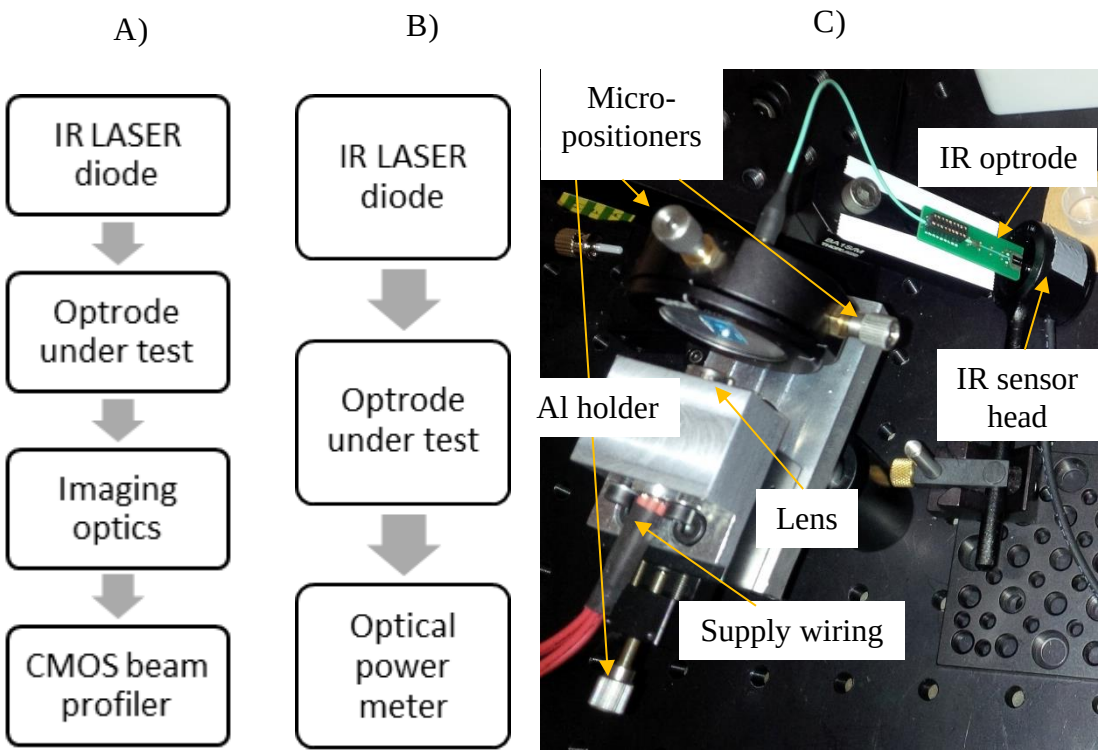

Figure 19: Schematics highlighting the main components of an optical setup used to determine (A) beam profile and (B) optical power [96]. *(C) Photo on the custom designed Al holder of laser diode built in an optical power measurement setup of (B). The Al holder provides proper cooling of the diode, focusing and collimating the IR light, and support the positioning of the fibre.*

3.6.1 Waveguide efficiency

My first optical experiment was focused on the waveguide efficiency of IR optrode chips through relative laser beam power measurements. Figure 20. shows a photo of the custom designed measurement setup. This measurement is especially sensitive to any background noise therefore it should be performed in completely dark environment. After an initial background noise acquisition and compensation, the IR light emitted from a properly polished optical fibre was measured by the beam profiler and set as reference intensity (I_{fibre}). Then this fibre was inserted into the fibre guide groove of a Si chip (optical dummies or functional optrode samples) so the IR light was coupled into the Si shaft. A similar measurement of the power emitted from the blunt tip was taken (I_{chip}).

Waveguide efficiency of the Si chips (η_{chip}) was derived in view of these two measurement values as follows:

$$\eta_{chip} = \left(\frac{I_{chip}}{I_{fibre}}\right) \qquad (4)$$

To prevent the beam profiler's sensor surface from scratch and to facilitate the replacement of samples during the series of measurements, a microscope objective with 50× magnification and 0.8 numeric aperture (Carl Zeiss, Jena) was placed in the light path, which provided a bit longer sensor-subject distance.

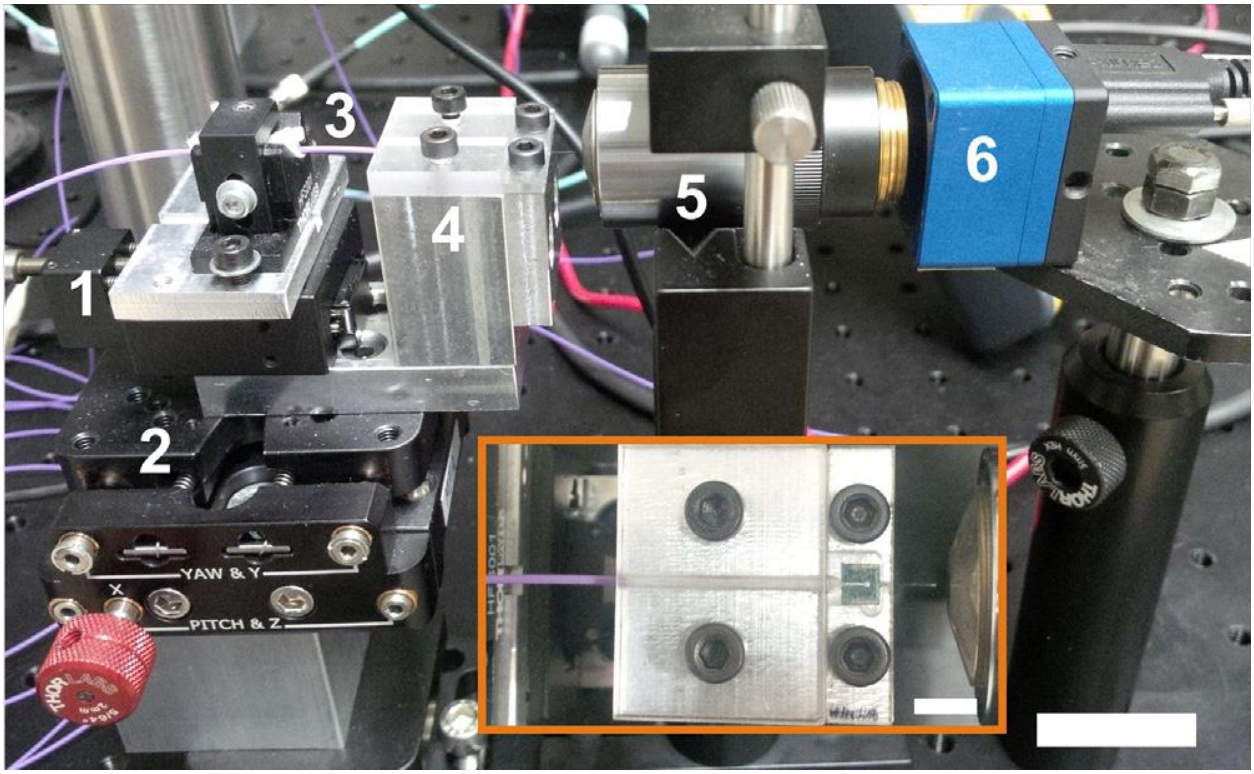

Figure 20: Photo of the waveguide efficiency measurement setup for chip scale optical characterization. The chip under test is inserted in a custom designed PMMA sample holder (4) fastened on a 3D translation stage (2). IR light (λ = 1310 nm) is delivered via a multimode fibre (3). The position of the fibre can be adjusted by a linear translation stage (1). Imaging (5) is made by a microscope objective (50×, NA = 0.8). All measured data are registered by a CMOS beam profiler (6). Scale bar shows 2 cm. The inset shows the top view of the fixed optrode chip in the PMMA sample holder. Scale bar of the inset picture shows 5 mm. [24]

The waveguide efficiency of assembled, fully functional IR optrode devices was also observed. Figure 21. shows a photo of the setup of this measurement (cf. Fig. 19.A.):

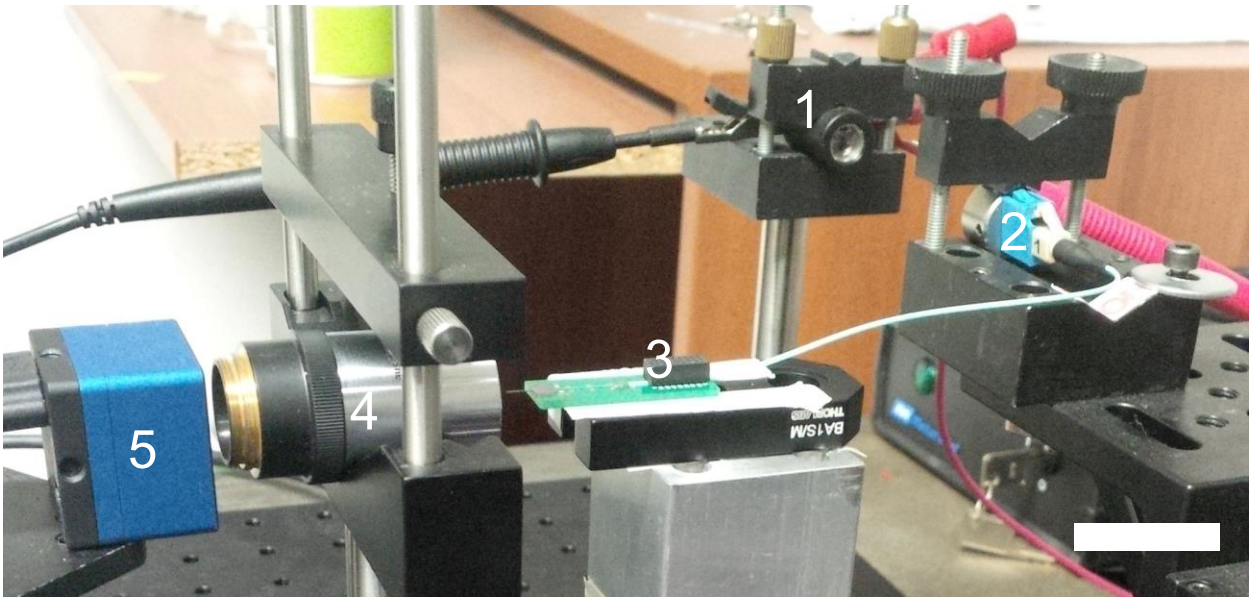

Figure 21: Photo of the measurement setup to characterize waveguiding efficiency of fully packaged optrodes. Collimated IR light (λ = 1310 nm) emitted from a laser diode (1) is focused on the front facet of the multimode fibre (2), which is part of the optrode device. The PCB (3) of the optrode under test is fastened on a 3D translation stage. Imaging (4) the plane of the optrode end facet is made by a microscope objective (50×, NA = 0.8). All measured data are registered by a CMOS beam profiler (5). Scale bar shows 2 cm. [96]

Similarly, the light emitted from a properly polished optical fibre was measured by the beam profiler first and set as reference intensity (I_{fibre}) after the background noise acquisition and compensation. Then this fibre was connected to an assembled IR optrode in the light path, and a similar measurement was taken ($I_{electrode}$). The ratio of these measurements ($I_{electrode}$ / I_{fibre}) was considered as the overall waveguide efficiency of the optrode device ($\eta_{electrode}$):

$$\eta_{electrode} = \left(\frac{I_{electrode}}{I_{fibre}}\right) \qquad (5)$$

The measurement setups introduced here (cf. Fig. 20 & 21.) provided images of the IR light beam profile emitted from the blunt tip of the Si chip (Fig. 23.A.). Through these images the incident beam spot size can be investigated according to ISO 11146 standard.

3.6.2 Far field diffraction

If the microscope objective is removed from the light path (see Fig. 22.), we get far field diffraction image (Fig. 23.B.) of the IR light emitted from the blunt tip of the Si chip. We

can call it as far field, because the distance between the plane of observation and the aperture of light scattering surface is large enough (much larger than the wavelength and the characteristic size of the aperture). The surface of the end facet of Si waveguide (shaft of the optrode) is considered as a scattering surface covered with apertures of diffraction. Although the initial scalloping caused by the DRIE etching was remarkably reduced (by step 13. on Fig. 15.), the sidewalls are not perfectly smooth (cf. [94]). Far field images were taken to evaluate beam divergence, because beam divergence depends primarily on diffraction present at the site of emission. These data were considered as practical initial conditions for a multiphysical modelling what was implemented to investigate the absorbed IR light's thermal effect in the tissue. Csanád Örs Boros and colleagues first built the optical ray-tracing model of the IR optrode's waveguiding modality concerning its surrounding ambience as air. My experiments validated the precision of this model [24]. Based on these experiences, they continued the development of the optical model concerning the possible effects of the brain tissue in case of implantation. Besides this optical model, they also built the finite element thermal model of the IR optrode in case of implantation. Later, they combined these two models into a coupled multi-physical (optical and thermal) model [112]. The outcomes of this combined model aided the design and the preparation of the *in vivo* experiments, which eventually validated both the thermal and the optical models concerning the brain tissue ambience [95].

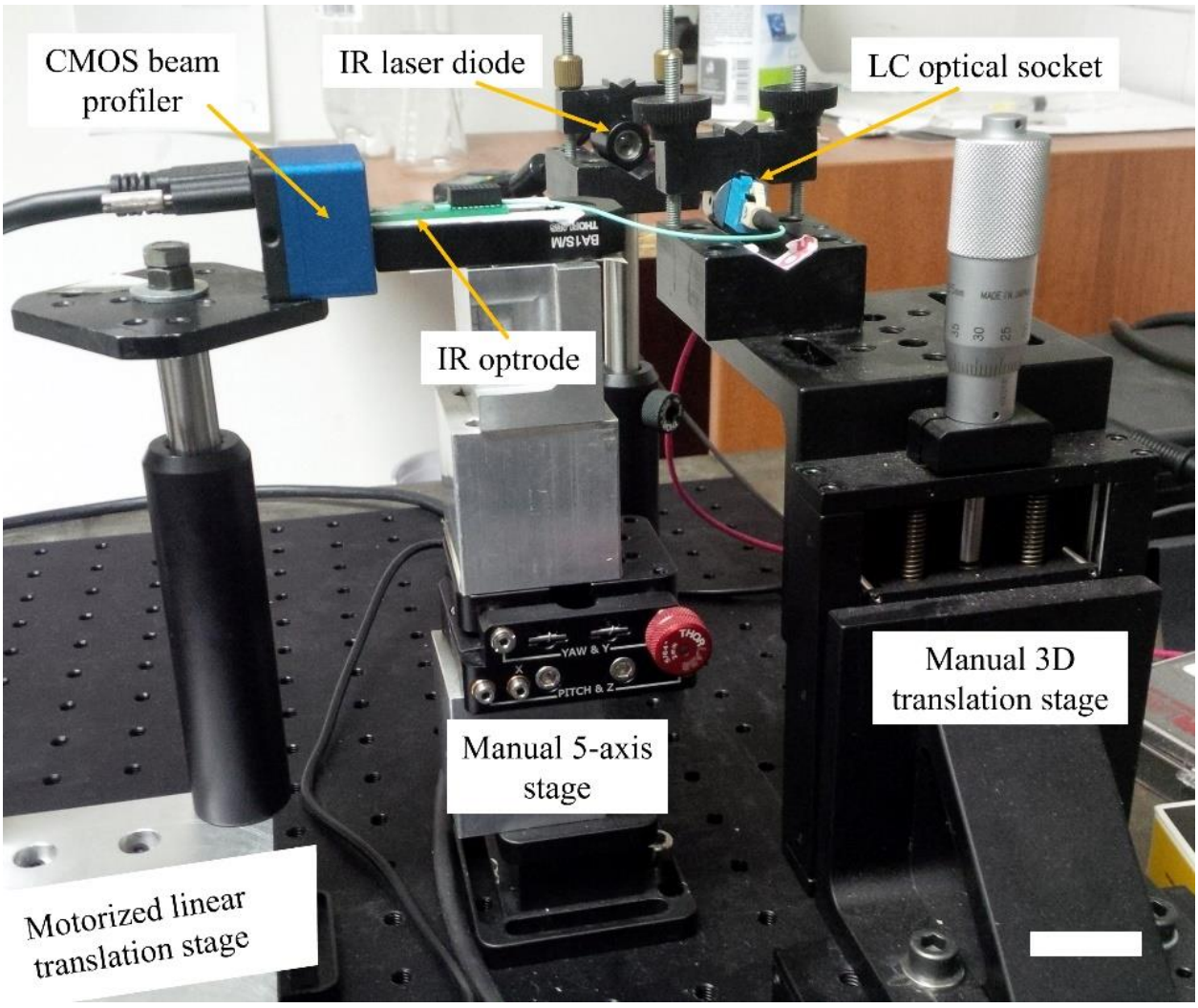

Figure 22: Photo of the measurement setup to characterize beam divergence of fully packaged optrodes. Collimated IR light (λ = 1310 nm) emitted from a laser diode is focused on the front facet of the multimode fibre, which is part of the optrode device. The PCB of the optrode under test is fastened on a 5-axis stage. All measured data of far field images are registered by a CMOS beam profiler fastened on a remotely controlled motorized linear translation stage. Scale bar shows 2 cm.

The same CMOS beam profiler was used to record far field diffraction pattern. It was fastened on a remotely operated precision linear translation stage (MTS50/M-Z8, Thorlabs Inc., USA), that provided acquisition at equidistant positions. The initial distance between the optrode's blunt tip and the beam profiler's sensor was set to 1 mm. After the background noise acquisition and compensation, sequential acquisitions with a 0.5 mm step-distance resolution were started (cf. Fig. 24.). Later, in chapter 4.3.2, the following

notations are used to quantify the angle of beam divergence (see Fig. 23.B.). Number of far field images used for evaluation are in brackets.

- Vertical: V1 pairs (n = 8)
  V2 pairs (n = 8)
- Horizontal: H1 pairs (n = 17)
  H2 pairs (n = 2)

The V1,V2 and H1,H2 labels do not represent exact maxima – which can be determined by the diffraction formula – only mark observable spots on each far field image acquired at equidistant positions, belonging to the same angle of beam divergence.

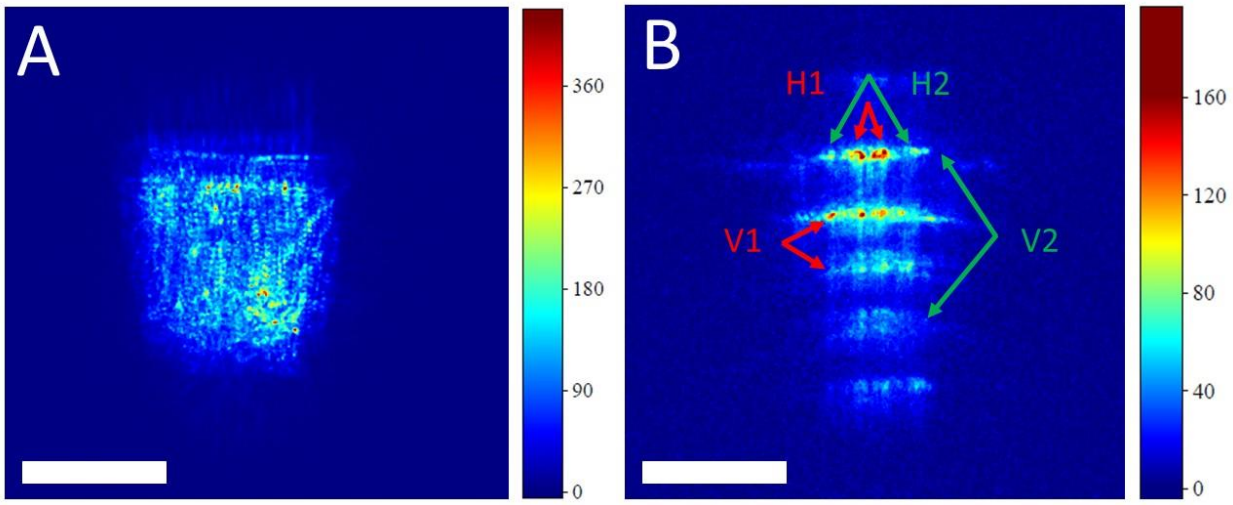

Figure 23: (A) IR light intensity distribution emitted from the blunt tip of the Si chip and (B) far field IR light intensity detector images recorded in the case of a representative optrode. The pixel intensity acquired with a CMOS beam profiler is in the same arbitrary units. Scale bars show 100 µm. Colours of the arrows on (B) represent pairs of diffraction maxima belonging to the same angle of divergence. [24]

3.6.2.1 Calculation of beam divergence

Beam divergence characteristics is derived from analysis of the positions of diffraction maxima (see Fig. 23.B.). Using the notation of Fig. 24. the equation of a line is:

$$y = a \cdot z + b, \qquad (6)$$

where a is the slope or gradient of the line; b is the y-intercept of the line; and z is the independent variable of the function y = f(z). Consider b as zero, then from basic geometrical considerations equation (6) can be rewritten as:

$$a = \frac{\Delta y}{\Delta z}, \tag{7}$$

where Δy is the difference of the vertical coordinates of the position of the same certain diffraction maximum on different detector image and Δz is the distance between two detector positions. In equation (7), a is to consider as the tangent of a theoretical right triangle with angle φ,

$$tan\,\varphi = \frac{\Delta y}{\Delta z} \tag{8}$$

where Δy and Δz are the opposite and the adjacent leg of angle φ. This φ angle is used to identify the angle of beam divergence, δ:

$$\delta = \varphi_L - \varphi_U \tag{9}$$

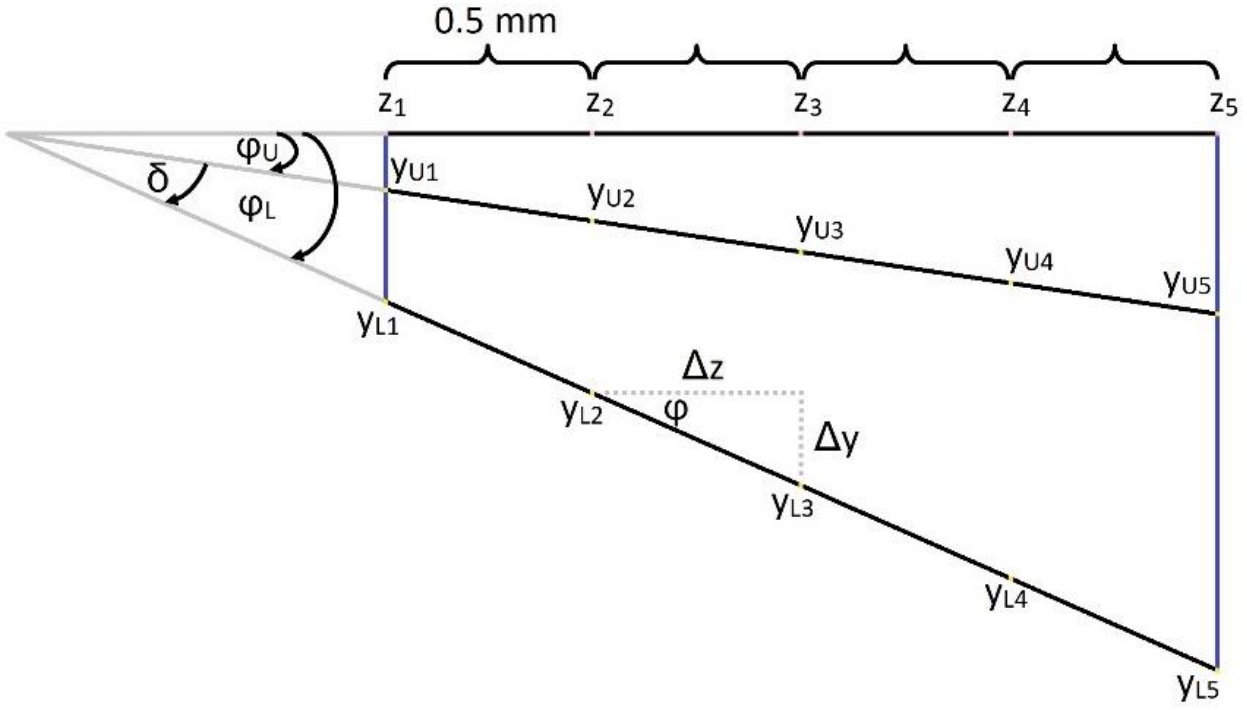

Figure 24: Explanation of beam divergence measurement (cf. Eqs. 6-9). [24]*suppl.*

3.6.3 Absolute power

I used an arrangement for absolute optical power measurement similar to that of the waveguiding efficiency measurement. The measuring instrument was replaced with an IR sensor (OP-2 IR Ge sensor head, Coherent Inc, CA, USA) connected to a laser power meter (FieldMaxII-TOP, Coherent Inc, CA, USA), and there was no imaging optic in the light path. Figure 25. shows a photo on the measurement setup (cf. Fig.19.B):

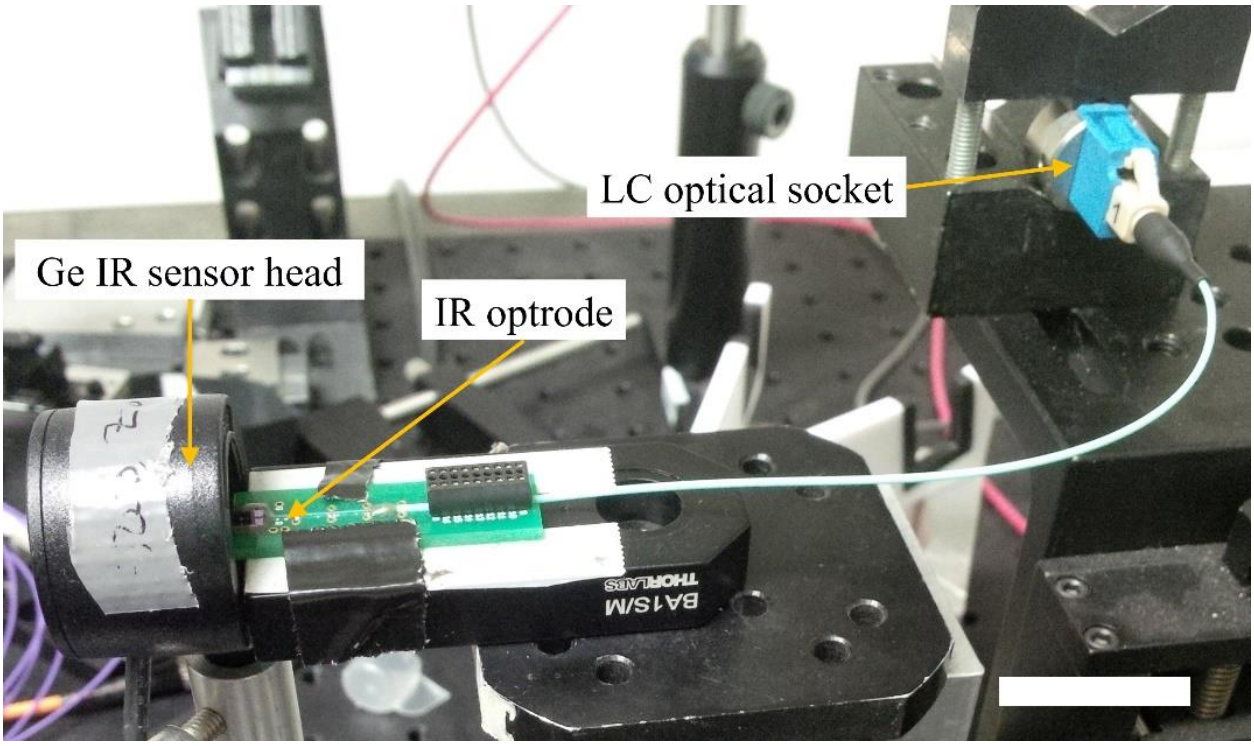

Figure 25: Photo of the measurement setup to characterize the absolute optical power emitted by the optrode device. Collimated IR light (λ = 1310 nm) emitted from a laser diode is focused on the front facet of the multimode fibre. The PCB of the optrode under test is fastened on a 3D translation stage. Absolute optical power is measured by a calibrated Ge IR detector directly without any imaging optic. Scale bar shows 2 cm. [96]

The IR light guided through the optical fibre part and emitted from the connected Si chip illuminates the detector surface of IR sensor head directly. The optical power value of the IR light emitted from the optrode's tip is computed by the instrument. To maintain repeatability of the experiments, I set the distance between the optrode's tip and the sensor's surface about 100 µm (see Fig. 26.). Besides this distance adjusting, I provided the orthogonality of the detector surface and the axis of the shaft to achieve perpendicular

light incidence on the detector. In cases, when optical power exceeds the range of the sensor (10 mW), an attenuator – mounted on the sensor housing – was used.

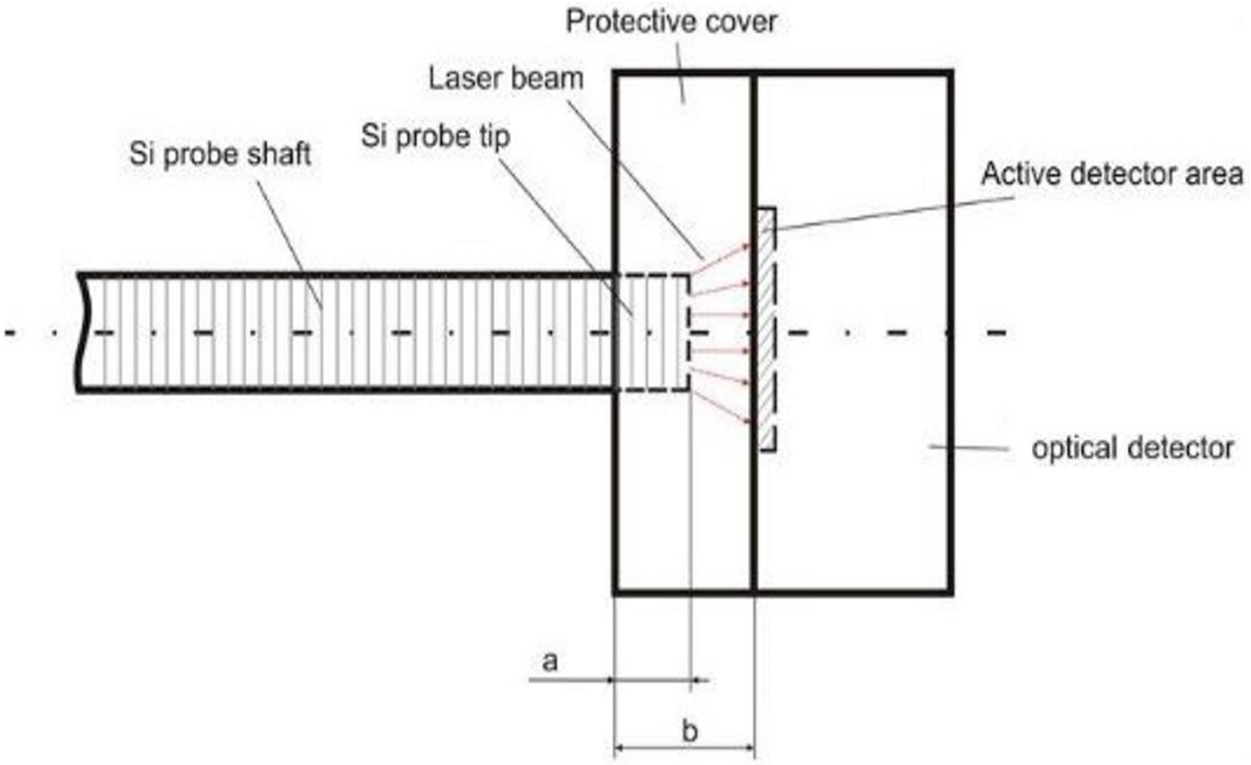

Figure 26: Schematic of the relative position of the optrode shaft and the IR detector's active surface. (a = 7 mm; b = 7.1 mm) [95]*suppl.*

3.7 Thermal characterization

In this chapter, all *in vitro* and *in vivo* experimental efforts to characterize the performance of the integrated temperature sensor are summarized.

3.7.1 Calibration of integrated temperature sensor

The optrode's integrated temperature sensor is a meander-shape Pt filament encapsulated in-between the passivation layer structure of the shaft. The main reason behind this implementation is the simplicity of manufacturing, since this configuration can be realized with a single metallization layer in the same step as the electrophysiological recording sites [24], [93]. Further advantage is the reliability, precision and linear response of Pt resistance thermometers [113]. This thermal sensor is located at the probe tip and is connected to four bonding pads used for 4-wire resistance measurement, which provides adequate accuracy.

Generally, by the application of resistance thermometers (also called as resistance temperature detectors, RTDs) the temperature dependence of their electrical resistance is exploited [113], [114]. The temperature dependence of resistance of conductive materials can be derived from the temperature dependence of specific resistivity:

$$\rho_m = \rho_0 \cdot [1 + \alpha \cdot (t - t_0)], \qquad (10)$$

where t is the temperature, t_0 = 0 °C, ρ_m is the specific resistivity at temperature t, ρ_0 is the specific resistivity at t_0 and α is the temperature coefficient of resistivity. Using the Pouillet's law:

$$R = \rho \cdot \frac{l}{A}, \qquad (11)$$

where l is the length and A is the cross-sectional area of the conductor, we can get to the following expression, the first-order approximation of the Callendar–Van Dusen equation:

$$R_t = R_0 \cdot [1 + \alpha \cdot (t - t_0)], \qquad (12)$$

where R_t and R_0 are the resistances of the conductor at t and t_0 temperatures, respectively. The international standard IEC 60751 formulates recommendations on the properties of platinum RTDs regarding the Callendar–Van Dusen equation [114]. It is advisable to use RTDs due to their accuracy and wide measuring range [113]. In case of platinum, its temperature characteristics can be considered as linear between -200 to +800 °C.

There are two typical procedures to calibrate a thermometer: taking measurements at temperature reference points [115] or making a series of simultaneous measurement with an already calibrated etalon, which has a suitable accuracy [116]. The applicable temperature reference points are related to phase equilibrium of pure materials (99.9999% or better), when the supplied heat is consumed by the material's phase transition, hence its temperature remains constant. For example, the triple point of water is one of the most common temperature reference point (0.01 °C, according to ITS-90).

I fulfilled the calibration of the optrode's integrated temperature sensor through a series of simultaneous measurement with an industrial aluminium-oxide negative temperature coefficient thermistor (NTC, Semitec 223Fu5183-15U004, Mouser Electronics, TX, USA)

used as reference [93]. Its accuracy of ±0.5% provided a ±0.14 °C measurement error in my experiments. During the calibration procedure, I controlled experimental conditions to be similar to that of *in vivo* surgery (cf. Fig. 27.). The measurement medium was 5 cl of physiological saline. Both the NTC thermistor and the optrode was lowered to the same depths as during *in vivo* recordings. The distance between the two sensors was set to 1 mm (see Fig. 28.). The medium was heated up to 50 °C, and then it was left to cool down to room temperature, while the simultaneous temperature measurements were performed using the thermistor and the integrated Pt RTD. The 4-wire resistance measurement of the Pt RTD was realized by 1 mA DC driving current of the filament according to literature recommendations [117] to avoid artefacts of self-heating. The temperature-dependent voltage was recorded with 20 Hz sampling rate. The current source was a Keithley 6221 precision current generator and a Keithley 2000MM multimeter (Keithley Instruments Inc, OH, USA) recorded the voltage data.

Based on the measurements, the temperature of the Pt RTD was estimated by fitting a first-order polynomial on the correlation of its voltage to the actual temperature values of the NTC thermistor measured between 33 and 39 °C in the cooling phase. The temperature coefficient of our integrated platinum filament (α) was then calculated based on the parameters of the regression, according to Eq. 12.

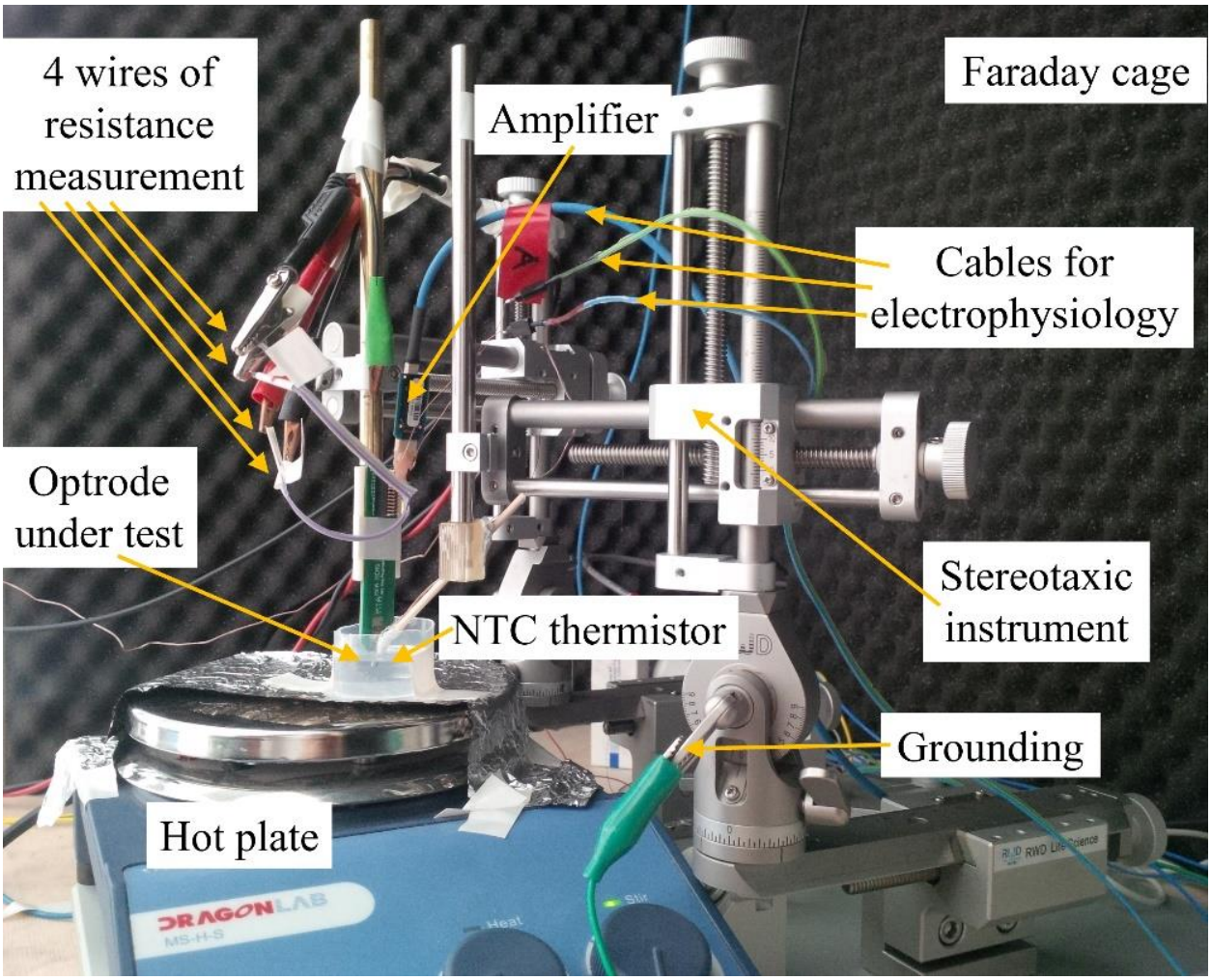

Figure 27: Measurement setup to perform calibration of the integrated thermal sensor.

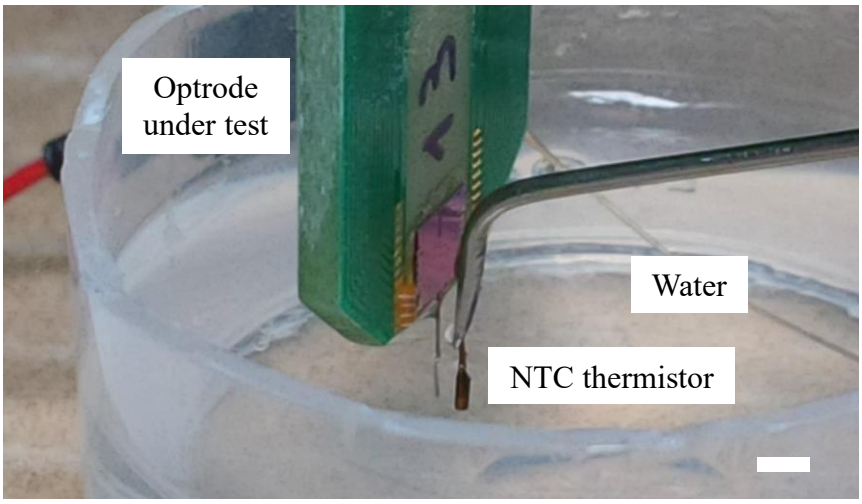

Figure 28: Relative position of the optrode and the reference NTC thermistor during thermal calibration. Scale bar shows 1 mm.

3.7.2 *In vitro* testing of heat distribution

The test of temperature distribution due to optical heating was performed in a 2 ml polyethylene cylinder filled with 1.7 ml room temperature saline [95]. It was essential to determine this spatial distribution of heat around the tip of the illuminating optrode to avoid any harmful overheating of the tissue in later *in vivo* conditions. Figure 29. shows the measurement setup. The shaft of two Si probes were immersed in the liquid medium. One was the heating source (optrode) and another one was used to measure the temperature change in different positions from the end facet of the optrode (reference point of the coordinate system). The IR light source was a pigtailed laser diode (LPSC-1550-FG105LCA-SMA, Thorlabs Inc., USA) with 50 mW and 1550 nm operating power and wavelength, respectively. IR illumination emitted from the optrode's tip was absorbed in the liquid medium, caused elevation in the temperature of that. This change in temperature was recorded by the 4-wire resistance measurement of the integrated Pt filament of the opposite Si probe. The spatial change of temperature was recorded at multiple locations along the axis of the shaft (x) and also in perpendicular direction (y) with 100 μm resolution set by a micropositioner.

First, the heating power (the level of supply current of the IR laser diode) was changed at a fixed position of the immersed shafts. This calibration procedure provided relation between temperature elevation and coupled optical power (see Fig. 48.), which is an essential input information to design *in vivo* tests. After that, the spatial distribution measurements were made at a selected optical power level.

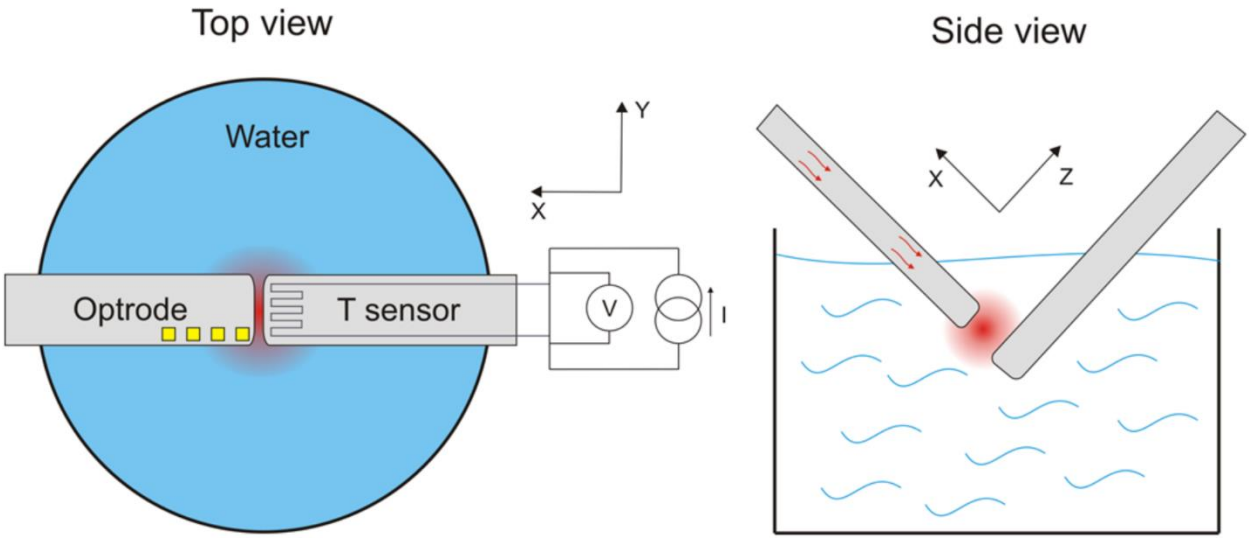

Figure 29: Schematics of the in vitro *experimental setup for the characterization of spatial temperature distribution. IR light is emitted from the end facet of the Si waveguide of the optrode (left). IR light absorbed in the surrounding medium (water) and spatial profile of effective cross-section can be characterized. The optically elicited temperature elevation can be measured by either the integrated Pt RTD of the illuminating optrode or alternatively by the one positioned in the close vicinity.* [95]

3.8 *In vivo* validation of the functional optrode

In this chapter the experimental details of the validation of device functionality in animal model is described.

3.8.1 Design of experiments

The primary aim of the *in vivo* experiment was to test concurrent IR stimulation and electrical recording in the deep neural tissue. The introduced dimensions of the Si shaft and the proposed packaging make the optrode usable in acute experiments in anesthetized rat. Urethane anesthetic agent was chosen because under urethane anesthesia, a similar activity was experienced like natural brain activity during sleep [118]. During my work in cooperation with colleagues in the Research Centre for Natural Sciences (RCNS), the somatosensory cortex and the hippocampus were the targeted brain regions. Figure 30. is the schematic of the position of the implanted devices in the brain. The optrode was implanted in the targeted depths from the superficial layer of the cortex down to the CA1 region of the hippocampus. Another commercial linear silicon probe was implanted in 18° as a calibration tool for neural activity recording modality of the optrode.

The source of IR stimulation was a pigtailed laser diode (LPSC-1550-FG105LCA-SMA, Thorlabs Inc., USA) with 50 mW and 1550 nm operating power and wavelength, respectively. The optically induced local tissue heating was monitored by 4-wire resistance measurement of the integrated Pt RTD of the optrode by a multimeter (Keithley Instruments Inc, OH, USA). The thermally evoked neural response was recorded by Intan amplifiers, connected to an Evaluation Board (Intan Technologies Llc., Los Angeles, CA, USA).

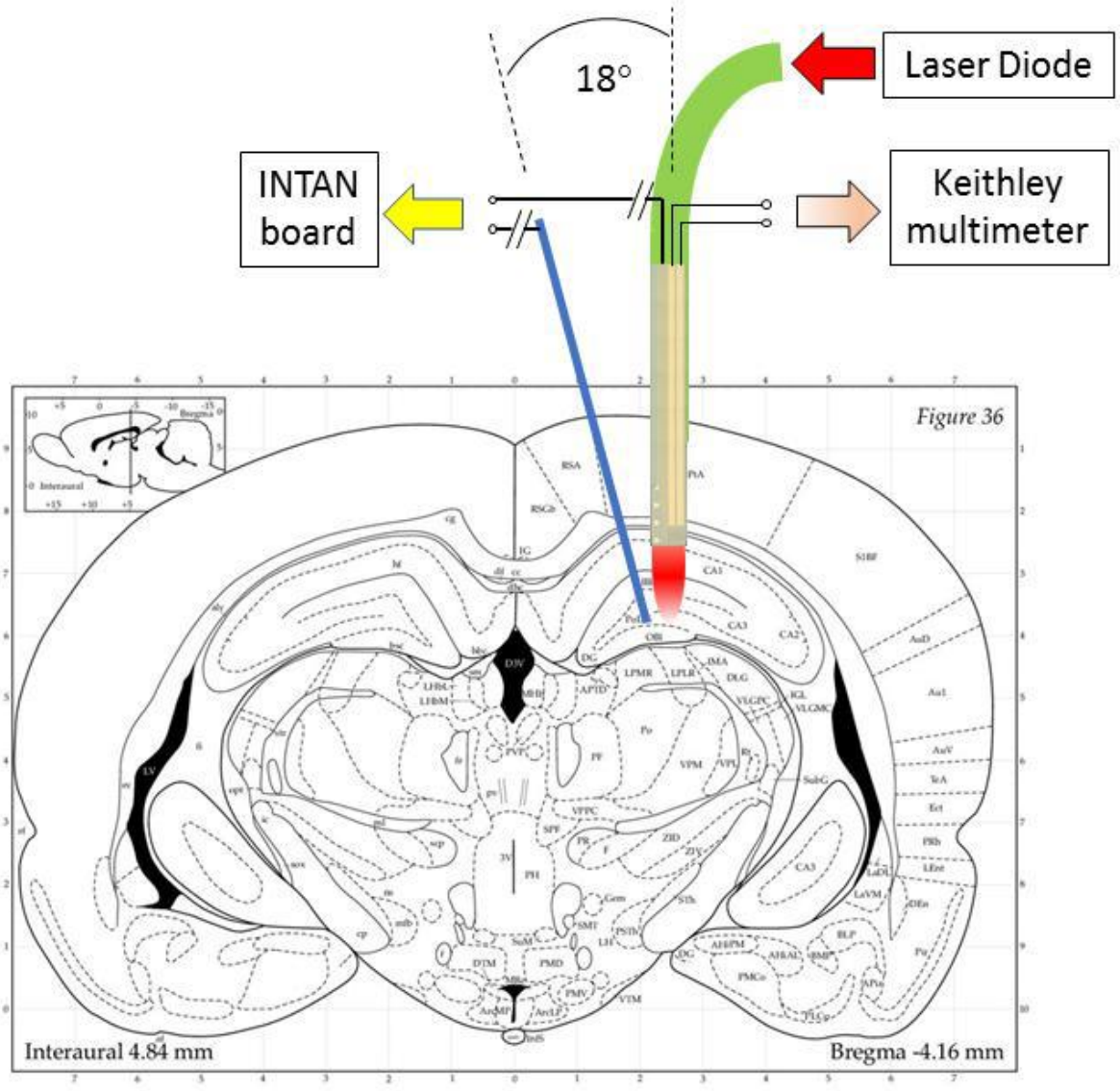

Figure 30: Experimental arrangement for the in vivo *validation of spatially controlled heating in the deep tissue. The blue line represents a commercial silicon probe used as control for the evaluation of electrophysiological response of the heated tissue. An INTAN preamplifier board is used to record the evoked activity through both the optrode and the reference silicon probe.* [95]*suppl.*

3.8.2 Measurement automation

Figure 31 shows the schematic of the *in vivo* experimental setup. The applied IR light source was a pigtailed laser diode (LPSC-1550-FG105LCA-SMA, Thorlabs, Inc., USA) coupled to the optical connector of the implanted optrode. Its light emission was controlled by a Keithley 2635A System SourceMeter device (Keithley Instruments Inc, OH, USA) in current source mode. The series of stimulating light signals was triggered using a square pulse generated by an NI-USB 6211 data acquisition system (National Instruments, TX, USA). Temperature monitoring was realized by 4-wire resistance measurement of the integrated Pt RTD of the optrode by a Keithley 2100 6½-digit multimeter (Keithley Instruments Inc, OH, USA). The extracellular neural activity was recorded by Intan RHD2132 16-channel amplifiers, connected to an RHD2000 Evaluation Board (Intan Technologies Llc., Los Angeles, CA, USA). Rectal temperature of the experimental animal was measured by a TH-5 Thermalert Monitoring Thermometer (Physitemp; Clifton, USA) and recorded using the analog inputs of the Intan RHD2000 system. All instruments were connected to x86 based PC, which ran the control software. Remote control of current supply and current signal waveform were realized by a custom developed code in the Keithley instrument's own programming languages (TSP, Lua). Its external triggering was controlled by a Matlab script of my colleague in RCNS. The program code which records the resistance values and transforms them to temperature was implemented by me also in Matlab. Data recording of the analog and digital channels of the Intan board was realized by its own software. The processing of the neural signal data was also realized in Matlab codes. My above-mentioned contributions for the automation and computer control of the measurements were awarded by a 10-month scholarship of the New National Excellence Program of the Ministry of Human Capacities of Hungary.

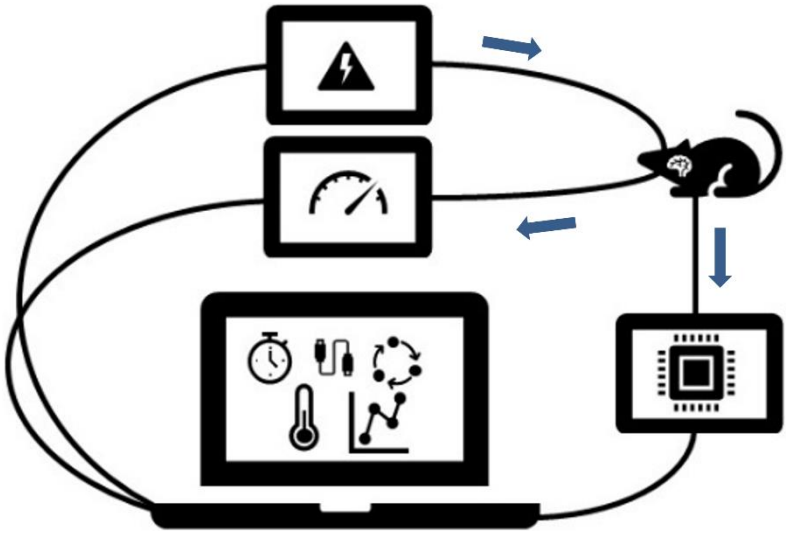

Figure 31: Schematic idea of the setup of in vivo *application of multimodal deep brain optrode. IR stimulation is remotely operated. The evoked neural activity and the corresponding temperature data are recorded simultaneously using the same computer interface.*

3.8.3 Surgery

The acute *in vivo* experiments were made in accordance with the Hungarian Act of Animal Care and Experimentation (1998, XXVIII) and with the directive 2010/63/EU of the European Parliament and of the Council of 22 September 2010 on the protection of animals used for scientific purposes. Experimental protocol was consented by the regional ethical committee (license number PEI/001/2290-11/2015 for *in vivo* experiments in question). The group of my neuroscientist colleagues, Sándor Borbély and Péter Barthó from RCNS, made efforts to minimize the number of animals used.

Our acute experiments were carried out on 3 male Wistar rats (Toxicoop, Budapest, Hungary) kept under a 12:12 h light : dark cycle (lights-on at 7:00 a.m.) in a temperature-controlled room at 22±2 °C. Standard food-pellets and tap water were available for them. Each animal, weighing between 230 and 440 g at the time of the surgery, was intraperitoneally anesthetized with urethane (1 g/kg), then placed in a stereotaxic instrument (RWD Life Science; Shenzhen, China). A single large craniotomy and durotomy were made over the somatosensory cortical region. After the implantation of the optrode and the reference electrode, we waited at least for 30 minutes before recording.

3.8.4 Stimulation protocols

One stimulation cycle was composed of 2 min long laser-ON, and 4 min long laser-OFF periods. The latter was aimed to provide enough time for the temperature of the stimulated region to return to baseline temperature. Based on the *in vitro* tests of the temperature distribution and the literature, we used the following stimulation power levels for CW irradiation at 1550 nm: 2.8, 6.9, 7.1, 8.5, 10.5, 10.7 and 13.4 mW. To check the reproducibility of the stimulation patterns in the electrophysiological traces, 10-15 trials were performed in a random fashion for each power (temperature). Furthermore, to check the stability of the stimulating power and to ensure the validity of the evoked neural and temperature response, absolute optical power measurements were performed before and after the *in vivo* implantation, similarly as explained in chapter 3.6.3.

3.8.5 Electrophysiology

Extracellular electrophysiological recording was performed through the integrated Pt sites of the optrode and those of the commercial linear silicon probe (Linear 16-channel silicon probe, A1x16-5mm-100-703, NeuroNexus, Ann Arbor, USA) as well. An additional screw electrode implanted over the cerebellum served as a reference. All signals were sampled at 20 kHz by the Intan system. Raw local field potential (LFP) channels were band pass filtered between 0.4-7 kHz, and multi-units were detected with an absolute threshold. The unit activity was combined from multiple neighbouring channels, downsampled to 1 kHz and smoothed with a 10 ms moving average filter. This data was used for calculation of peri-stimulus time histogram (PSTH) of heating events. Single unit detection was made by a simple thresholding method, followed by a manual clustering.

4 Results

4.1 Evaluation of optrode technology through visual inspections

Figure 32 shows a photo of the four types of the optical dummy samples. In the left column, chips with 400 µm shaft width, in the right column chips with 170 µm shaft width are presented. In the top row, Si_xN_y-covered Si chips, in the bottom row bare Si chips are shown. The blue coloured Si_xN_y-covered chips shows that dielectric thin-film coverage is even throughout the chip surface.

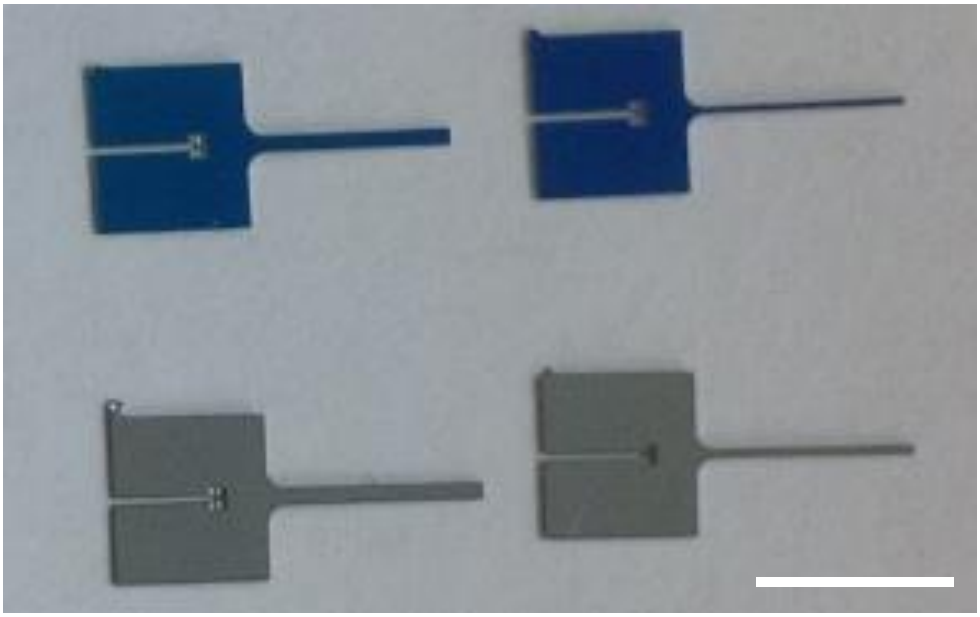

Figure 32: Photo on the dummy samples used for the preliminary optical characterization of waveguide efficiency. Top: Si chips covered with SiN (blue); bottom: bare Si chips (grey); left: chips with 400 µm shaft width; right: chips with 170 µm shaft width. Scale bar shows 5 mm.

Figure 33 shows scanning electron microscopy (SEM) and optical microscopy images of particular details of functional optrode chips. Figure 33(a) shows a close SEM view of the fibre guide groove, the fenders and the cylindrical lens. The first two parts ensure proper positioning of the optical fibre to the lens to achieve good efficiency light coupling into the waveguiding shaft. Fenders adjust the proper distance between the end facet of the optical fibre and the lens. The fibre guide groove supports the positioning of the optical fibre without angular error. Figure 33(b) and (c) are top view optical microscope images of a fully functional optrode tip with the Pt thermal sensor filament and electrophysiological recording sites before (b) and after (c) electroplating platinum-black

on the latter surfaces. These images show that the temperature sensor and the recording sites are placed as close as possible to the end of the tip and to each other to ensure recording true local information on temperature dependence of neural activity. Figure 33(d) and (e) are close SEM view of the fibre guide groove funnel-shape inlet and the polished sidewall of the shaft, respectively. The goodness of the smoothness of the sidewall anticipates little scattering and good efficiency waveguiding through the Si shaft.

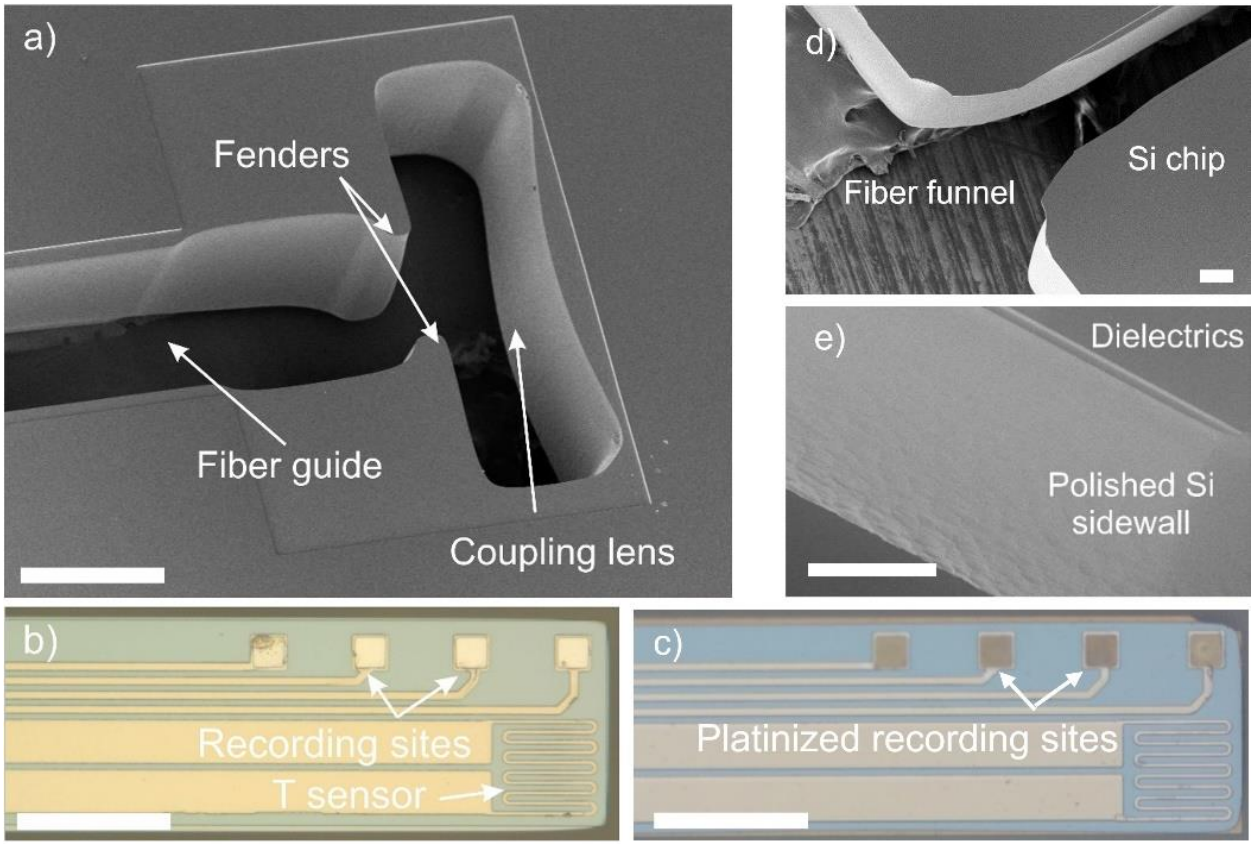

Figure 33: Microscopic investigations of the engineered microstructures of the optrode. (a) Close SEM view of the coupling region on the chip. Tip of a fully functional optrode (b) before and (c) after electroplating platinum-black on the recording sites. (d) Close SEM view of the funnel-shape inlet fibre guide groove. (e) Representative SEM view of the polished sidewall of the optrode shaft. Scale bar shows 100 µm on all figures.

Figure 34 (a) shows a labelled photo of an assembled IR optrode mounted with an LC optical connector (1). Figure 34 (b) is a magnified view of the fibre coupling part of the optrode chip (marked with (5) on Fig. 34. (a)).

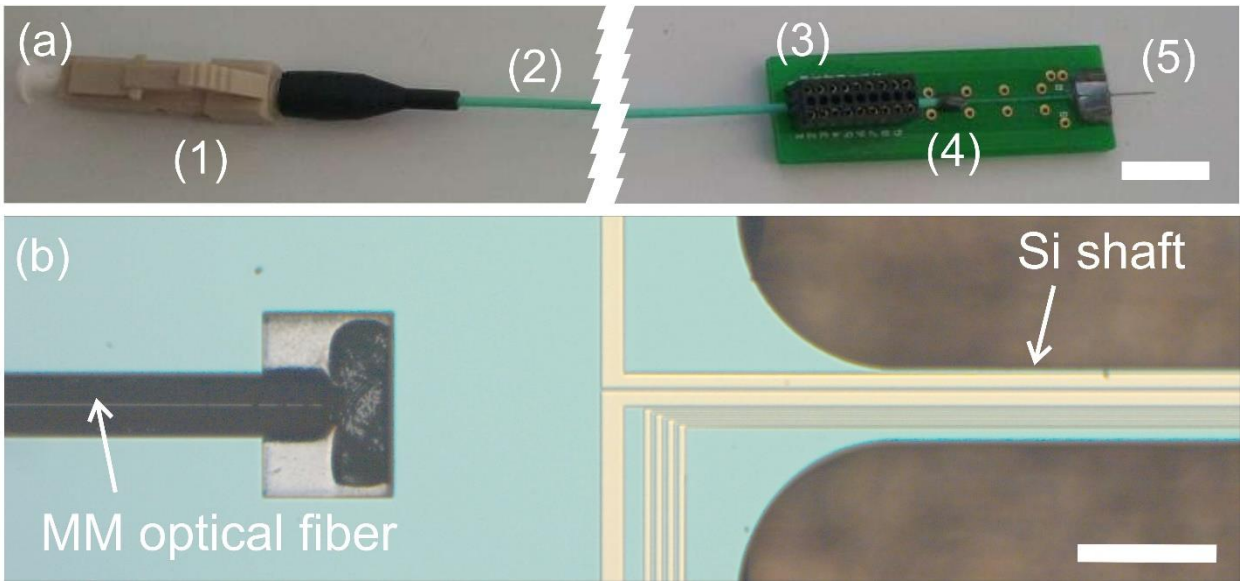

Figure 34: (a) Perspective view of the assembled IR optrode. Relevant components are numbered: (1) LC optical connector, (2) Multimode optical fibre, (3) PreciDip electrical socket, (4) PCB, (5) multimodal Si chip. (b) Close view of coupled fibre positioned to the focal point of the integrated coupling lens of the optrode. The airgap between the end facet of the fibre and the probe is filled up with index-matching glue. Scale bars represent 8 mm and 200 µm on picture (a) and (b), respectively. [24]

4.1.1 Thesis 1.

I developed a microfabrication process to create an implantable, multifunctional, silicon-based microprobe capable of both optical stimulation and interrogation of neural activity (infrared optrode, IR optrode). The optrode consists a monolithically integrated optical waveguide, a temperature sensor and four platinum sites. Platinum recording sites are integrated to record electrophysiological response evoked by the infrared irradiation delivered through the waveguide of the probe.

Related publications:

Á. C. Horváth, Ö. Sepsi, C. Ö. Boros, S. Beleznai, P. Koppa, and Z. Fekete, "Multimodal Neuroimaging Microtool for Infrared Optical Stimulation, Thermal Measurements and Recording of Neuronal Activity in the Deep Tissue," *Proceedings*, vol. 1, no. 4, p. 494, Aug. 2017., DOI: 10.3390/proceedings1040494

Á.C. Horváth, Ö.C. Boros, S. Beleznai, Ö. Sepsi, P. Koppa, Z. Fekete, "A multimodal microtool for spatially controlled infrared neural stimulation in the deep brain tissue,"

Sensors and Actuators B: Chemical, vol. 263, pp. 77-86, June 2018., DOI: 10.1016/j.snb.2018.02.034

4.2 Electrochemical performance of recording sites

As mentioned in chapter 3.5.1, the Pt recording sites of the optrode were characterized using electrochemical impedance spectroscopy (EIS). In the literature, the impedance of *in vivo* recording electrodes at 1 kHz typically range between 50 kΩ–1 MΩ [100]. A Portuguese-Chinese-Norwegian group demonstrated a multimodal silicon optrode device in [60]. The shaft of this microdevice holds ten 50×50 μm^2 rectangular Pt thinfilm electrophysiological recording sites around a blue light LED chip (470 nm peak-wavelength) on the top side and a meander-shape integrated Pt RTD on the bottom side. The impedance at 1 kHz of these recording sites was measured as |Z| = 371 kΩ. Figure 35 shows a representative Bode plot of the four sites of the IR optrode. This measurement was made using optrodes of flat Pt recording sites (cf. Figure 33(b)). The amplitude value of the impedance at 1 kHz is |Z| = 1031±95 kΩ. This average value with standard deviation is derived from the 12-times repeated EIS measurement of 8 different recording sites. It shows that the variability among the sites is less than 10%. Nevertheless, this impedance is sufficiently low for many *in vivo* applications, which aims to record the activity of single neurons. One objective reason of the difference between the 1 kHz impedance values shown here is the different size of the recording sites of the two mentioned devices.

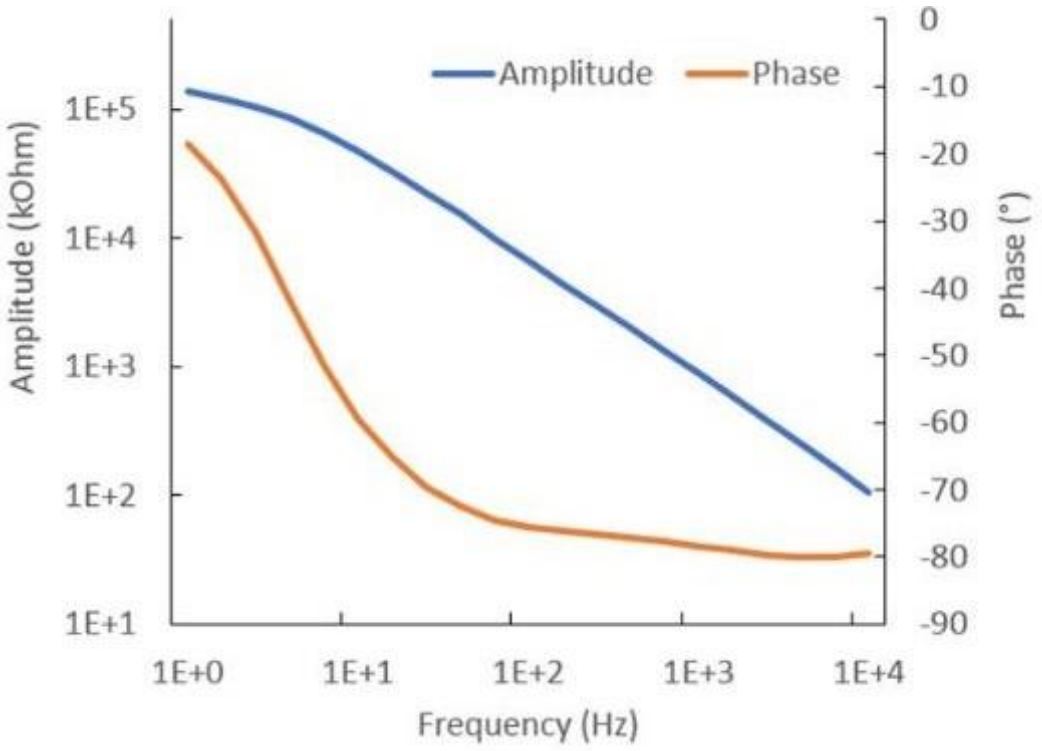

Figure 35: Representative Bode plot of the Pt recording sites of the optrode measured with electrochemical impedance spectroscopy. Primary and secondary ordinate represent the amplitude and phase values at various frequencies, respectively. The amplitude value of the impedance at 1 kHz is |Z| = 1031±95 kΩ. Number of sites: 8, repetition of measurement: 12 times with each site. [24]

4.2.1 Improvement in site impedance

Figure 36. shows the amplitude characteristic curves of the Bode plot of electrophysiological recording sites before (red) and after (yellow) electroplating porous Pt. In this case, the initial amplitude value of the impedance at 1 kHz of the pure platinum sites was |Z| = 678±198 kΩ (n=4). Due to the additional deposition of porous Pt it was reduced to |Z| = 46±9 kΩ (n=4). This reduced impedance is slightly better than the |Z| = 75.1 kΩ reported in [13]. This reduction is beneficial, since it reduces thermal noise of the electrodes, which is proportional to the square root of the real part of the impedance [119] (cf. Eq. 3.).

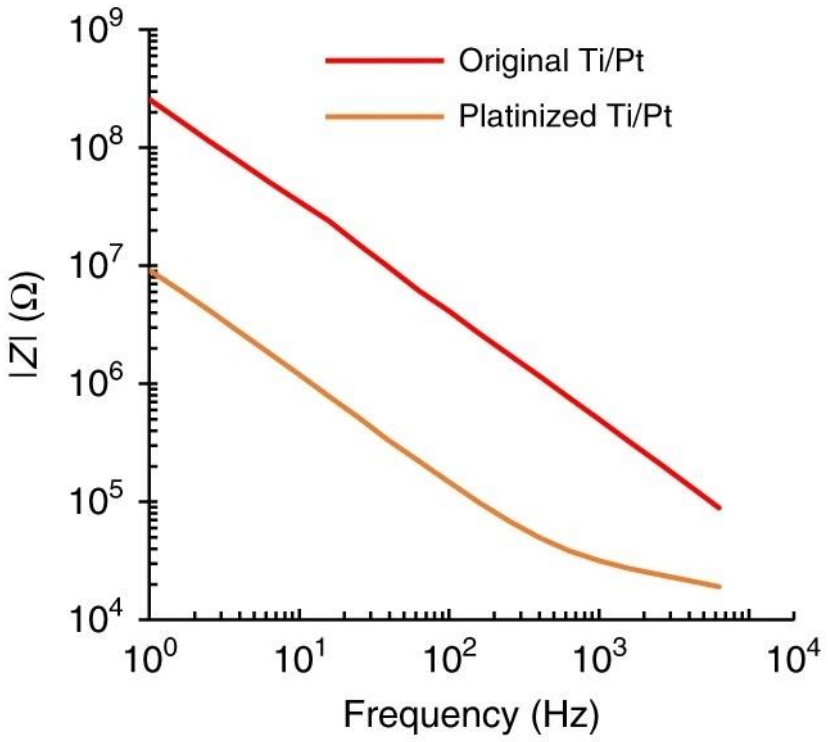

Figure 36: Amplitude characteristics of the electrophysiological recording sites recorded during EIS tests before (red) and after (yellow) porous Pt deposition. The initial impedance value at 1 kHz decreased from 678±198 kΩ to 46±9 kΩ (n=4). [95]

4.2.2 Soak tests

Besides the impedance measurement and electroplating, the experimental setup in Figure 17. was used to test the integrity of the passivating layer structure of the optrode chips in the long run. The observed specimens were permanently immersed in PBS. During 16 days of EIS test introduced in chapter 3.5.1, potential changes in electrical characteristics were monitored. Figure 37. shows average amplitude values of the impedances at 1 kHz measured at four consecutive recording sites. Results show no remarkable impedance decrease, which proves the fact that the applied technology is suitable for fabricating optrodes appropriate for long-term *in vivo* experiments. The application of saline solution to observe the stability of the recording sites [120], their impedance [64], [121], [60] or to simulate long-term *in vivo* behaviour [122] is prevalent in the literature. In our case the 1 kHz impedance changed within a range ±18% during two weeks of immersion in PBS which is similar to the results reported in [122]. The 1 kHz impedance of the Au/Pt

recording sites (with passivation layer stack of SiO_2 and Si_3N_4) on the Si substrate of their device was $|Z|_{initial}$ = 1.87 MΩ and $|Z|_{after\ 2\ weeks}$ = 2.22 MΩ.

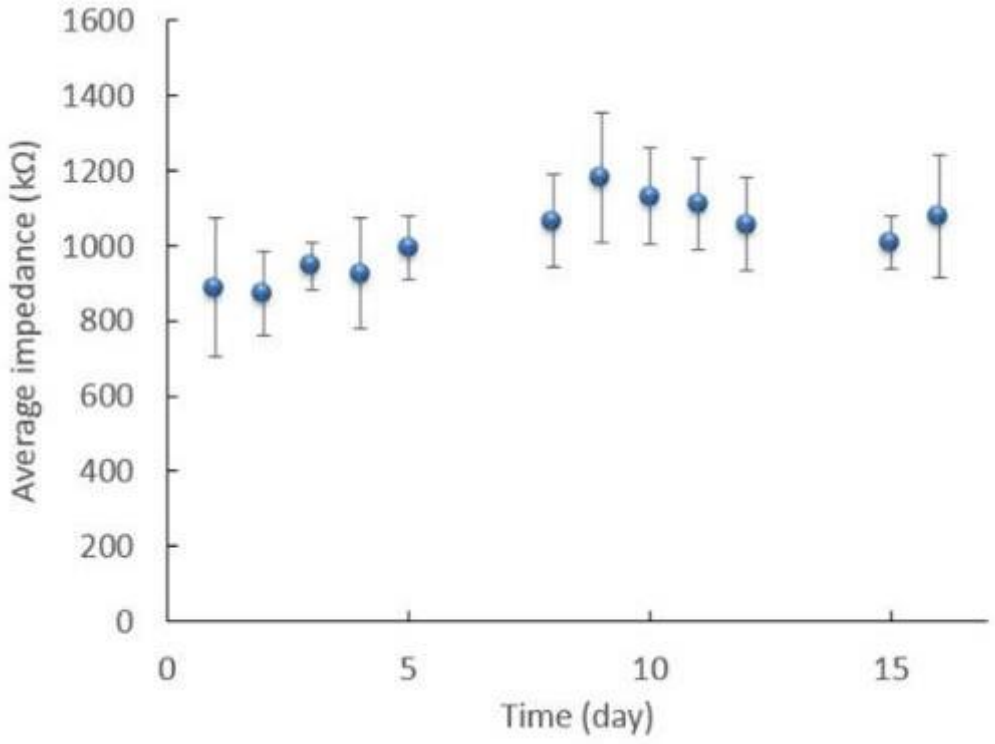

Figure 37: Average impedance values of four Pt recording sites located on the same optrode and measured in a 16 day long soaking test in saline at 1 kHz. The lack of any remarkable impedance decrease proves the fact that the passivating layer structure of the optrodes and the employed wet chemical post-processing steps result in leak-free dielectric stack appropriate for in vivo *experiments.* [24]

4.2.3 Thesis 2.

I determined the electrical characteristics of the electrophysiological recording sites of the IR optrode by electrochemical impedance spectroscopy. The initial impedance of the recording sites measured at 1 kHz can be reduced to 46±9 kΩ from 678±198 kΩ by electroplating porous platinum on top of the sputtered platinum sites. Utilizing long-term soaking tests, I proved that the applied dielectric layer structure can provide stable insulation of the platinum wiring. I determined that the average impedance values of the electrophysiological recording sites measured on a daily basis at 1 kHz changed less than 18% around the mean value of 1031 kΩ during a 16-day-long stability test in phosphate buffer solution.

Related publications:

Á.C. Horváth, Ö.C. Boros, S. Beleznai, Ö. Sepsi, P. Koppa, Z. Fekete, "A multimodal microtool for spatially controlled infrared neural stimulation in the deep brain tissue," *Sensors and Actuators B: Chemical*, vol. 263, pp. 77-86, June 2018., DOI: 10.1016/j.snb.2018.02.034

Á. C. Horváth, S. Borbély, Ö. C. Boros, L. Komáromi, P. Koppa, P. Barthó, Z. Fekete, "Infrared neural stimulation and inhibition using an implantable silicon photonic microdevice" in *Microsystems & Nanoengineering*, vol. 6, no. 44, 2020., DOI: 10.1038/s41378-020-0153-3

4.3 Optical performance of integrated waveguides

Boros et al. built the combined optical and thermal simulation model (ray tracing and scattering) of the optrode in question considering IR laser excitation with 1310 nm [112]. His optical model calculated the overall optical waveguiding efficiency of the IR optrode as 30.5±2.5%, including a calculated attenuation along the shaft like 0.15 dB/mm. (Dimensions of the shaft: L = 5 mm; t = 200 µm; w = 170 µm) To compare, the demonstrated waveguide loss of the 5 µm thick integrated SU-8 waveguide of Cho et al. was -0.22 dB/mm using 470 nm blue light [64]. They derived this value by measuring different length of SU-8 waveguide structures between 0-7 mm. The total coupling and transmission loss through the integrated dielectric waveguide presented by Wu et al. was 10.5±1.9 dB [66]. They also used blue (473 nm) light. The structure and geometric dimensions of this latter mentioned surface waveguide: the core material is a 5 µm thick SiON layer surrounded by a 3 µm thick cladding. The width of this surface waveguide is tapered along its total length, along the shaft (~5 mm) from 28 to 14 µm.

4.3.1 Relative beam power tests

Figure 38. shows the comprehensive results of experiments investigating the waveguide efficiency of optical dummy samples. As expected, coupling the light into wider shaft results in higher efficiency. Silicon-nitride layer on the top side has an observable effect on the operation of waveguides, lowering the overall efficiency. The potential reason behind this phenomenon is supposed to be induced by the increase in the refractive index

on the top side (n_{SiN} = 2.206), with respect to that of the air (n_{air} = 1). Nevertheless, the waveguide efficiency of nitride-covered samples is still reasonable.

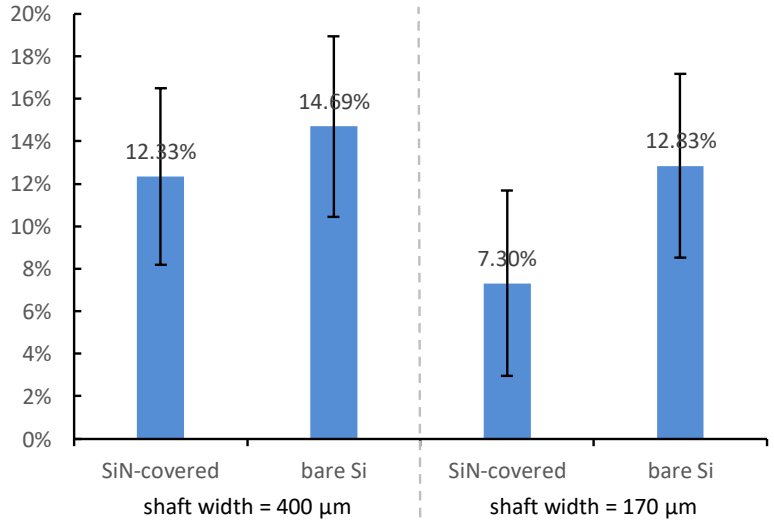

Figure 38: Average waveguide efficiencies (η_{chip}) with standard deviation of optical dummy samples. Number of samples: 4×6, repetition of measurement: 5 times with each sample.

Figure 39. A. shows the results of waveguide efficiency measurement of 9 individual optrode chips already holding the integrated functions. Their average waveguide efficiency is η_{chip} = 32.04 ± 4.10 % which is in a good agreement with the modelling results of Boros et al. [112]. This type of comparison is rather inadequate in case of assembled, fully functional IR optrode devices: the position of the fibre with respect to the chip is fixed in case of every sample and these fixed positions are not exactly the same due the alignment accuracy of the manual packaging process. The best and worst performance among the assembled optrodes was $\eta_{electrode}$ = 41.5 ± 3.29% and 9.07 ± 1.34%, respectively (see Figure 39. B). Apparently, the precision of manual assembly during the packaging process highly influences the overall waveguide efficiency, however, there was a significant improvement in the standard deviation of the repeatability from 17.75% to 7.18%.

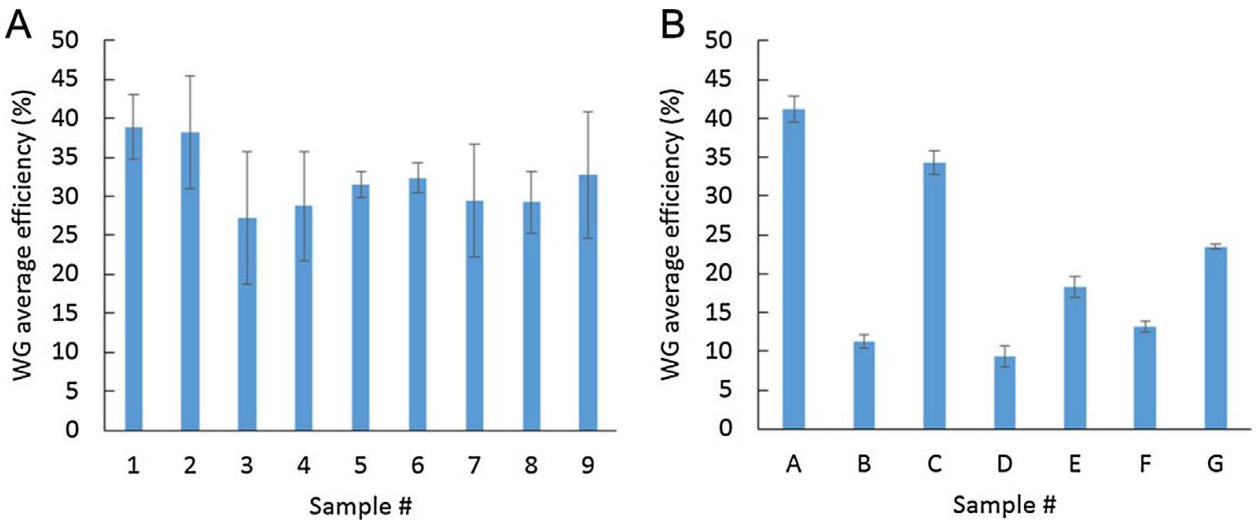

Figure 39: Average waveguide efficiencies of (A) functional optrode chips (η_{chip}) and (B) assembled optrode devices ($\eta_{electrode}$). Repetition of measurement: 5 times with each sample of (A)&(B). [24]

The abovementioned results on the waveguiding performance of the optrode in question presented on Fig. 39. A&B are comparable with some of the results in [68] (cf. Fig. 40. A&B). Both arrangements used an optical fibre with 50 µm core diameter and numerical aperture of 0.22 to deliver the 1550 nm IR light from the source to the Si waveguide.

My results on Fig. 39. A are derived from similar measurement conditions like that of the results marked with a grey rotated square ('◆') on Fig. 40. A&B. It means that surrounding medium between the optical fibre and the Si waveguide is the ambient air (n = 1.0). Note, that not only the length of the shafts is different in these two cases ($L_{my\ optrode}$ = 5 mm; $L_{Utah\ array}$ = 0.5–1.5 mm) but also the shape of the shafts: the shaft of my optrode is a rectangular cuboid with a constant cross-section of t × w = 200 × 170 µm^2, while the shafts of the Utah-type array are linearly tapered to a point from a base width of about 180 µm. So, because of the different geometric dimensions, more emitted light is expected from the blunt tip of my optrode than from one shaft of the Utah-type array. The mentioned graphs support this statement: the average waveguide efficiency of nine samples of my optrode is the abovementioned η_{chip} = 32.04 ± 4.10%, the smallest is 27.21 ± 8.46%, while all the normalized power values of the 10 rows within the Utah array are less than 0.25 (25%) (cf. Fig. 40. A).

My results on Fig. 39. B can be compared to the data marked with black circle ('●') and square ('■') on Fig. 40. A&B. These latter data are derived from measurements using two different kind of index matching fluid as the surrounding medium between the optical fibre and the Si waveguide ($n_{●}$=1.44 and $n_{■}$=1.66). In my case, I used an index-matching glue to fill the gaps between the Si and the fibre with a refractive index of n=1.56, as mentioned in 3.3. So, these results are less comparable than in case of Fig. 39. A., but it is apparent that the application of index-matching materials improved the efficiency, the normalized power. Another difference between the measurements introduced in [68] and my measurements is that the optical fibre was in contact with, but not attached to, the base of the Utah array in all cases showed on Fig. 40. A&B, while in the cases on Fig. 39. B the fibres were placed in fixed positions what are not exactly the same due the alignment accuracy of the manual packaging process. This causes the observable differences among the particular waveguide efficiencies on Fig. 39. B. However, none of the measured results on Fig. 40. A&B are as high as the highest one on Fig. 39. B. ($\eta_{electrode}$ = 41.5 ± 3.29%), all of their results remained below 0.4 (40%).

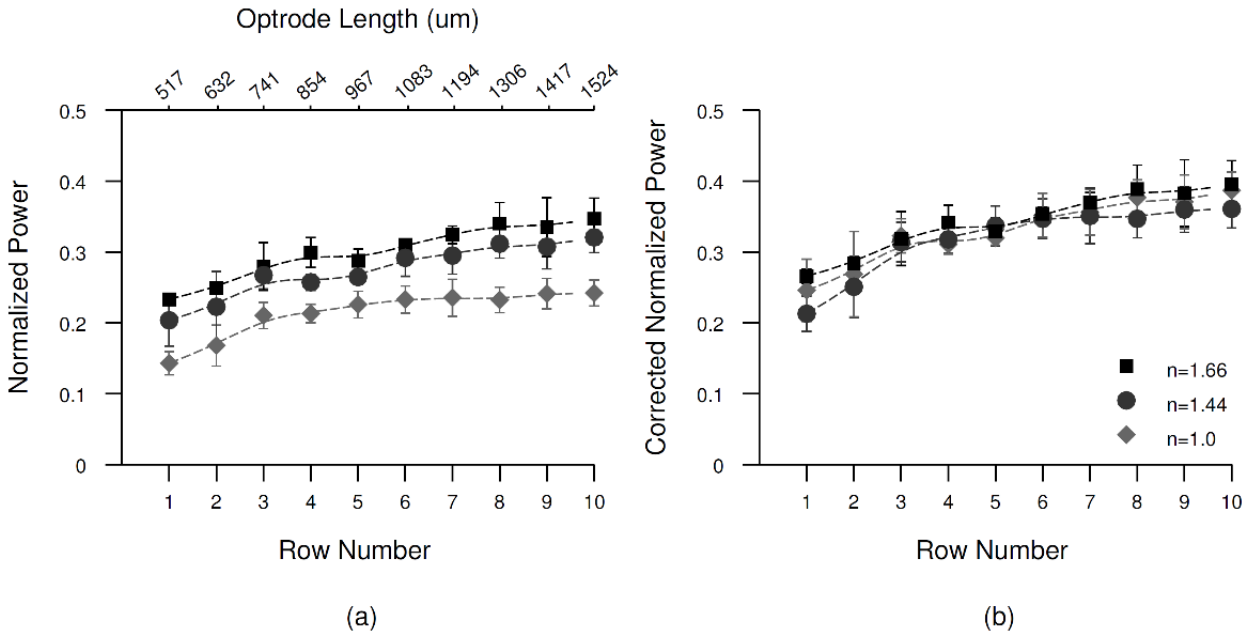

Figure 40: Normalized output power from the tips of the Utah slant optrode array with different shaft length, varying refractive index at the input interface using a 50 µm fibre with 0.22 NA, adapted from [68].

4.3.2 Beam divergence tests

Figure 41. A&B show the angle of beam divergence (δ) in vertical and horizontal directions, respectively, as defined in chapter 3.6.2. In vertical direction (perpendicular to the plane of the electrode), diffraction maxima are $12.1 \pm 1.7°$ and $38.4 \pm 4.7°$. In horizontal direction, the neighbours of diffraction maxima could be evaluated with statistical significance, as $6.3 \pm 2.3°$, while the other pairs were only visible in case of one electrode (16.6°). In view of these findings, the beam is widening more significantly in the out-of-plane direction compared to the in-plane direction. In my opinion, it is probably the effect of difference in sidewall smoothness between the double-side polishing of the initial substrate (top and bottom) and the sidewalls of the shaft, which were smoothed by wet etch process after the DRIE release and are still little bit uneven. Beam divergence is primarily determined by diffraction at the emitting surface. It can be deduced that the smaller the aperture diameter, the larger the size of the diffraction spot. So, the light emitted from the shaft has broader divergence along the shorter side. Sidewalls along the longer side are not perfectly smooth, scattering, and reduce the anisotropy of diffraction, but do not eliminate it; the topside and the bottom side of the Si wafer (and the chips) are smooth with atomic precision. The cylindrical lens does not play a role in this respect, its only function is to couple the light emitted from the fibre into the shaft. The shaft then acts as a multimode waveguide, where the phases are averaged, so that the phase front can be considered homogeneous, and the effect of the lens no longer prevails.

The full-angle beam divergence in air of a 1.5 mm-long Si shaft on the Utah-type optrode array is about $17 \pm 2°$ [88]. Note, that in their case the geometric dimensions and the shape of the Si waveguide are different, however, the rotationally symmetric (somewhat conic) shape of each shaft on the Utah array anticipates this symmetric output beam.

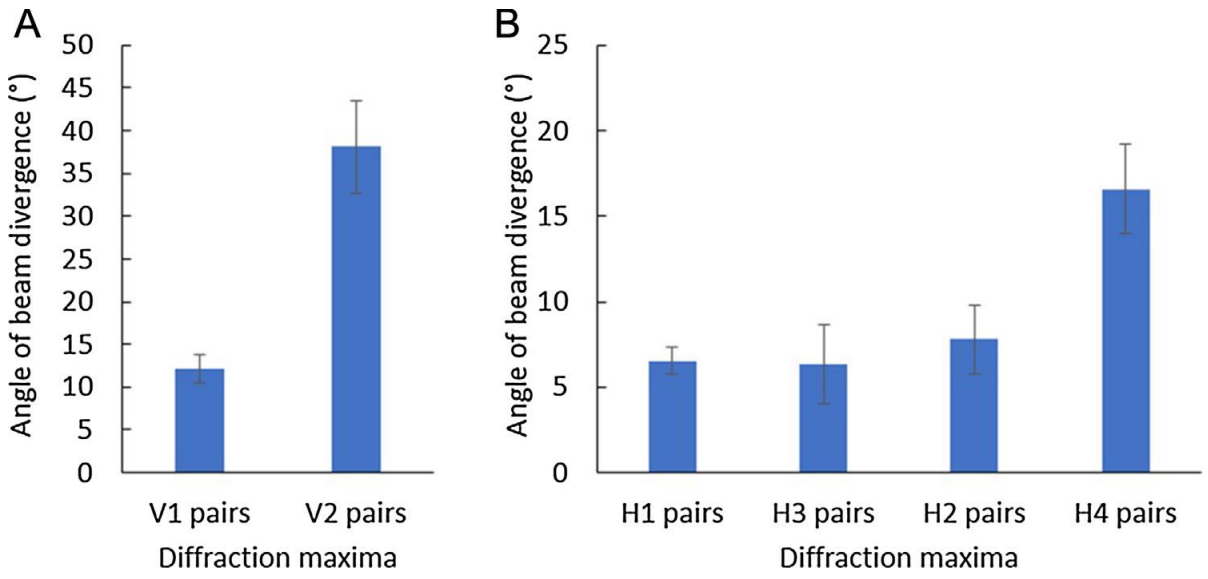

Figure 41: Summarized angle of beam divergence (δ) values. The definitions of each class is detailed above in chapter 3.6.2. [24]

4.3.3 Comparison of relative and absolute power

Figure 42. shows similar trends in the results of relative (a) and absolute (b) optical power measurement of 6 optrode devices assembled with fibre having an LC-type optical connector. This implies that most of the optical power is coupled out from the probe tip, and the propagation loss is not significant.

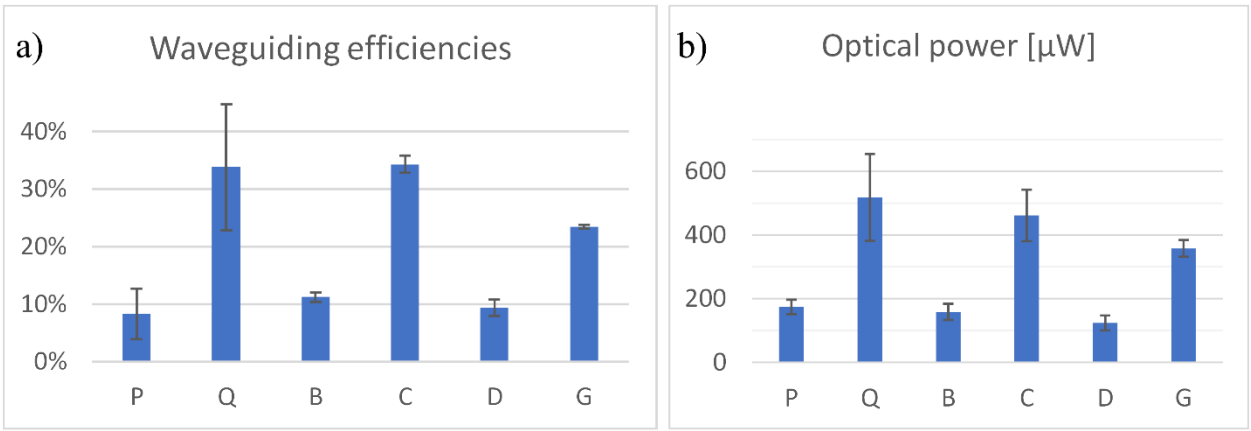

Figure 42: Comparison of (a) waveguiding efficiency and (b) optical power measurements in case of optrodes with LC connector ending. Output power of the IR light source: P = 1.5 mW. Number of repetition: n = 5 and n = 9, respectively. [96]

4.3.4 Effect of fibre optic core and connector

In this chapter, I present comprehensive results on the relation of optical connector, diameter of fibre core and waveguiding efficiency ($\eta_{electrode}$) of the optrode devices. As it was mentioned above, in chapter 3.3, I worked with three different types of optical fibres: mounted with LC, ST (core diameter: 50 µm) and SMA connector (core diameter: 105 µm). Figure 43 compares the waveguide efficiency results of these mentioned types measured by the beam profiler.

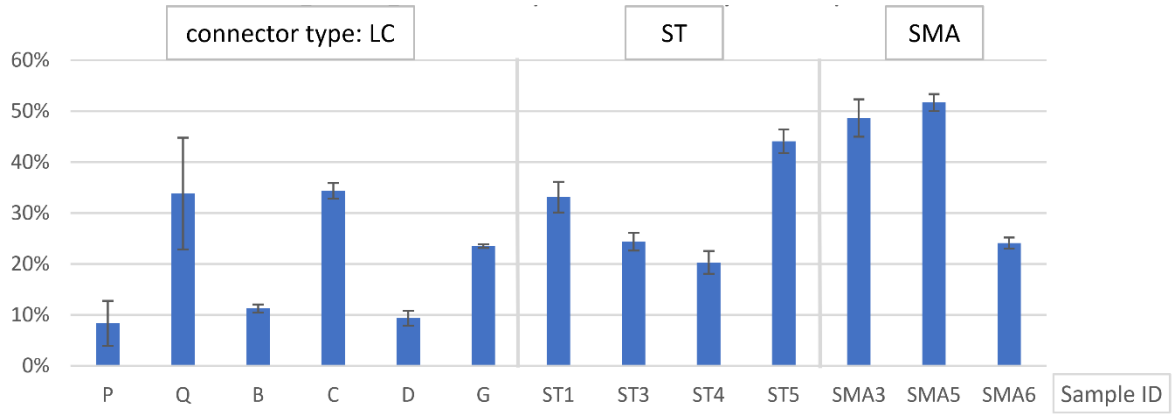

Figure 43: Effect of optical fibre's core diameter (LC and ST connector: 50 µm; SMA connector: 105 µm) on waveguide efficiency measured by beam profiler. Number of repetition: n_{LC} = 5, n_{ST} = 5 and n_{SMA} = 6.

Thinner fibre core diameter optrodes with LC and ST connectors have 20.09 ± 12.12% and 30.46 ± 10.53% average waveguiding efficiencies, respectively. The optrode devices assembled with SMA connector (thicker fibre core), resulted in a 10% increase in this parameter up to 46.11 ± 15.45%. This improvement is probably partially due to the core diameter of the fibre, since both the connector type and the length of the fibres were changed in latter case.

Figure 44 shows waveguide efficiency results of optrodes assembled with ST and SMA optical connector measured by laser power meter. The results of optrodes with ST connector are presented with mean values (orange columns) and range (minimal and maximal values marked with green dashes). The results of optrodes with SMA connector are presented with mean values (orange columns) and standard deviation (black markers). The remarkable improvement of measurement repetition is clearly observable on this figure. The smallest range among optrodes with ST connector is about 14% (in case of

sample ST4), while the largest standard deviation among optrodes with SMA connector is less than 2.5% (in case of sample SMA1).

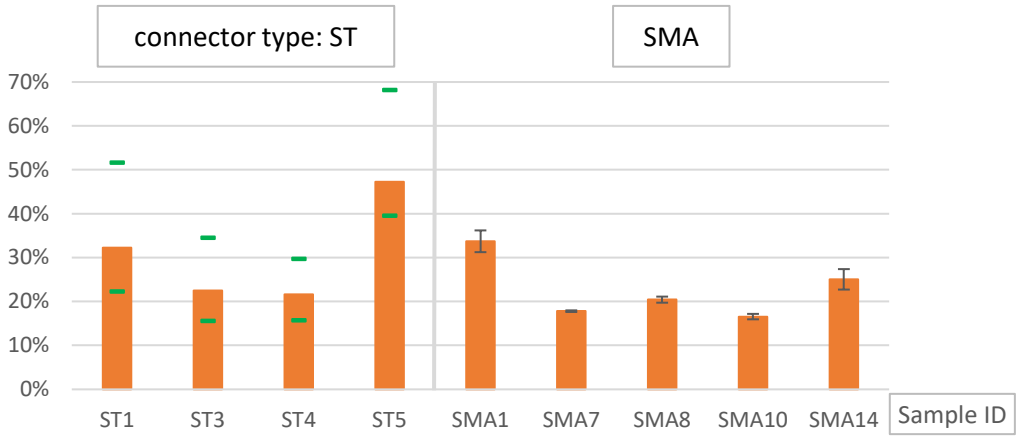

Figure 44: Effect of optical fibre's core diameter (ST connector: 50 µm; SMA connector: 105 µm) on waveguide efficiency measured by laser power meter. Number of repetition: n_{ST} = 4 and n_{SMA} = 10.

Figure 45. A&B show similar comparison on the effect of the core diameter of the optical fibre (50 or 105 µm) on waveguiding efficiency in case of the Utah array [68] with an n=1.66 index-matching material between the fibre and Si. The different curves on the graphs represent different measurement arrangements investigating the role of different parts of the tapered Si waveguides on overall efficiency. They found that the most remarkable difference is discernible in the radiation loss along the tapered shaft and its amount is depending on the shaft length. Reason behind this feature is that shorter shafts have tips of steeper tapering profile resulting in a larger tapering angle with respect to the propagation direction of rays, which means that more rays will not satisfy the conditions of total internal reflection at the boundary of Si and surrounding medium (e.g. air or tissue) causing leaking radiation (cf. Fig. 45. A&B '■'). Additionally, another interesting ascertainment is the effect of fibre core diameter on the previously discussed phenomena. Thicker fibre core resulted in weaker efficiency, less variation with optrode length and smaller standard deviation of measurement repetition (see Fig. 45. B '■'). They supposed that the light beam from a thicker core fibre have smaller radiation angle with respect to the surface boundaries resulting in less out-scattered rays thanks to the improved probability of total internal reflection.

My results are in good agreement with the abovementioned ones, as the standard deviation of measurement repetition on Fig. 44. is remarkably smaller in cases of 105 µm core SMA fibres than the 50 µm core ST fibres. There are also differences between the cases presented in [68] and the optrode in question. The shaft of my optrode is not tapered, it has parallel sidewalls (and the index-matching material between the fibre and Si has a refractive index of n=1.56), so the IR light coupled from a thicker fibre core results in better waveguiding efficiency (cf. Fig. 43.).

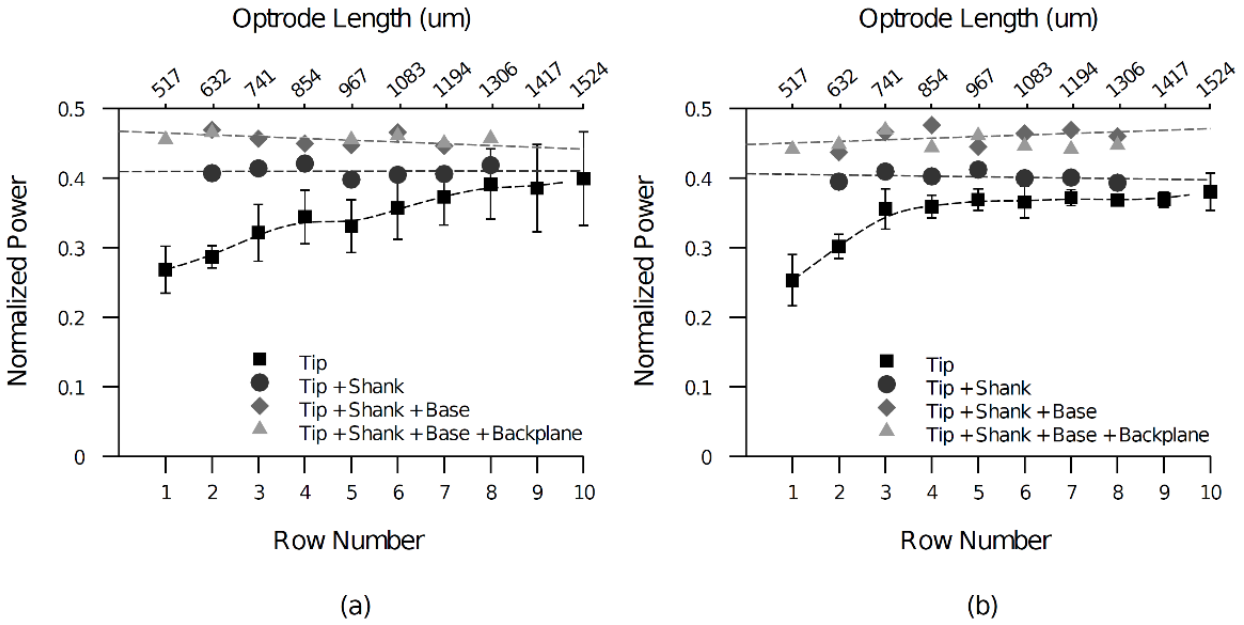

Figure 45: Normalized optical measurement results for the different shaft lengths of the Utah slant optrode array coupled to (a) 50 and (b) 105 µm fibres and using an n=1.66 index-matching material between fibre and Si, adapted from [68].

Figure 46 shows a qualitative comparison of IR detector images taken on optrodes assembled with ST and SMA connector, respectively. As it can be seen on Fig. 46. B, thicker, 105 µm fibre core leads to more even light distribution in the Si waveguide.

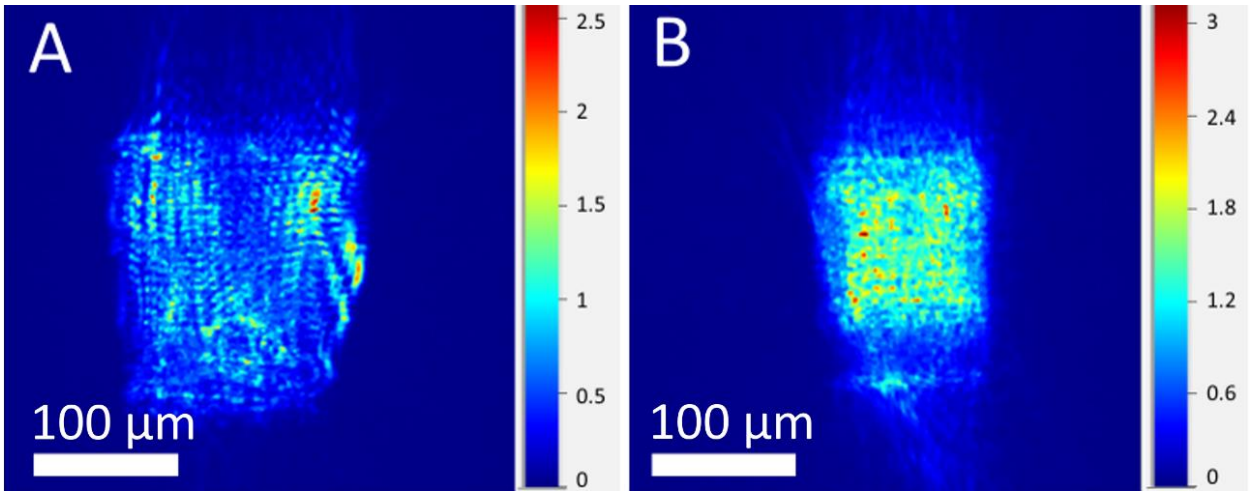

Figure 46: IR detector images on tip of IR optrodes assembled with fibre with (A) 50 and (B) 105 µm core diameter. Labelled pixel intensity on the right is in arbitrary units. [96]

Beam spot size measurement according to ISO 11146 standard was made on optrodes assembled with thinner, 50 µm fibre core. The seven optrodes with LC type connector have a 0.024 ± 0.006 mm^2, the four ones with ST type connector have a 0.03 ± 0.002 mm^2 average beam spot size. The geometrical surface of the tip of the optrode's waveguiding shaft is 0.0323 mm^2. These quantitative results support the qualitative results shown by detector images.

4.3.5 Thesis 3.

I developed an experimental arrangement to characterize the absolute optical power and beam profile emitted from the end facet of the waveguide integrated on the optrode chip. In the case of chip-scale measurements, I showed that the waveguiding efficiency of the optrode chips is 32.04±4.10%, using a light source with 1310 nm wavelength. I developed an encapsulation process to facilitate the testing of all integrated functionalities of the chips. Due to the precision of the assembly method, the repeatability of optical measurements increased, the standard deviation was reduced below 4% in case of individual assembled devices. The overall optical efficiency of the assembled optrodes can be as high as 41.5±3.29%.

Related publications:

Á. C. Horváth, Ö. Sepsi, C. Ö. Boros, S. Beleznai, P. Koppa, and Z. Fekete, "Multimodal Neuroimaging Microtool for Infrared Optical Stimulation, Thermal Measurements and Recording of Neuronal Activity in the Deep Tissue," *Proceedings*, vol. 1, no. 4, p. 494, Aug. 2017., DOI: 10.3390/proceedings1040494

Á.C. Horváth, Ö.C. Boros, S. Beleznai, Ö. Sepsi, P. Koppa, Z. Fekete, "A multimodal microtool for spatially controlled infrared neural stimulation in the deep brain tissue," *Sensors and Actuators B: Chemical*, vol. 263, pp. 77-86, June 2018., DOI: 10.1016/j.snb.2018.02.034

Á. C. Horváth, C. Ö. Boros, Ö. Sepsi, S. Beleznai, P. Koppa and Z. Fekete, "Optical characterization of an infrared neural optrode," *2018 Symposium on Design, Test, Integration & Packaging of MEMS and MOEMS (DTIP)*, Roma, pp. 1-4, 2018., DOI: 10.1109/DTIP.2018.8394242

4.4 Thermal properties of the devices

Integrated resistive temperature sensors of the optrodes were calibrated individually before *in vitro* and *in vivo* use. Figure 47 shows characteristic curves of these sensors of five optrode devices. It is clear, that their resistance response to thermal changes (the slopes of the curves) are very similar – as expected from a Pt thermal sensor. The average temperature coefficient of the integrated temperature sensors is $\alpha = 2636 \pm 75$ ppm/K. Although their zero-point resistances are not the same, they are close to each other in the same range. This fact highlights the importance of a preceding calibration of the integrated temperature sensor of each optrode device before *in vivo* application. To compare, the temperature coefficient of the on-shaft integrated Pt RTD demonstrated in [60] is 1500 ppm/K, which means that their RTD has less change in resistance due to a unit change in temperature. Note that the geometric dimensions (layout) of the integrated RTDs are different for these mentioned devices.

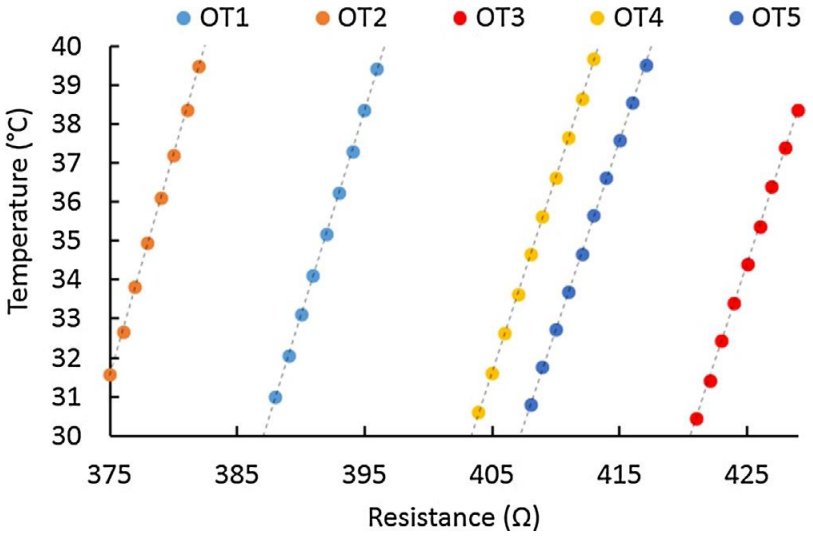

Figure 47: Calibration curves of integrated temperature sensors of five optrode devices. [24]

4.4.1 Calibration results of external temperature measurements

Figure 48. A shows calibration curves of optical heating *in vitro*. These curves show the temperature elevation as a function of optical power coupled into the surrounding medium. Temperature measurements in these cases were made by the temperature sensor of another optrode simultaneously immersed into the liquid with the illuminating one. The distance between the tips of the two immersed shafts was x = 200 µm in all cases (cf. Figure 29). Each plotted datapoint represents the average of five heating cycles of similar parameters (see Fig. 48. B): after 30 s recording of initial temperature, the output of the current source of the laser diode was switched on for 60 s then it was switched off to ensure time for cooling down. The maximum temperature was probed at the plateau of five consecutive cycles to evaluate the average rise in temperature in response to a particular excitation scheme.

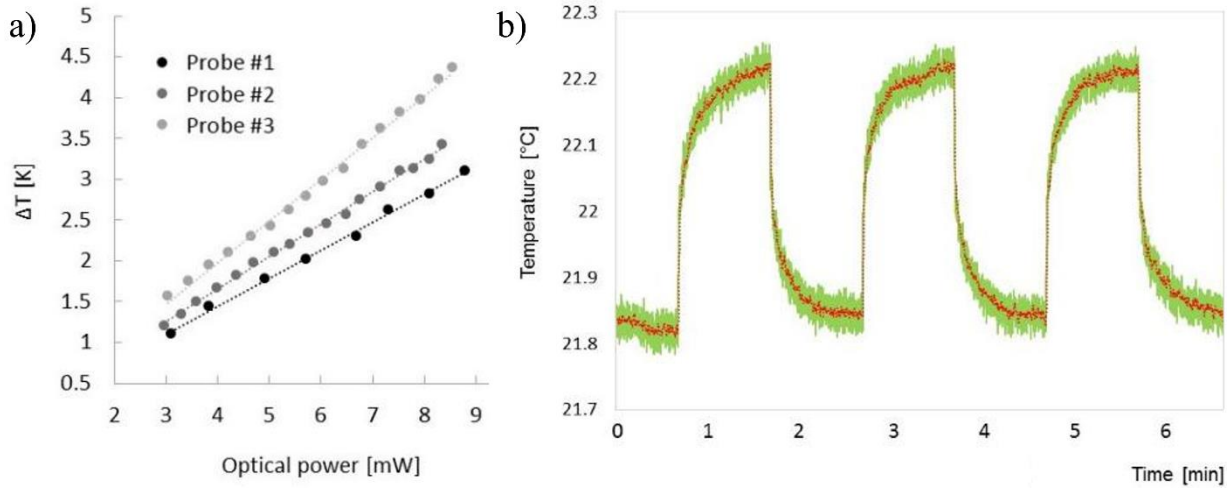

Figure 48: a) Temperature elevation as a function of optical power: calibration curves of optical heating measurement in vitro. *b) Time domain representation of recorded data during optically induced heating with cycles of square wave signals (T=2 min, P=4.16 mW). Each point of a heating curve on (a) is derived as the average of five heating steps, like the three ones on (b).* [95]

4.4.2 Integrated vs. external temperature

Since all thermometer measures its own temperature, the displayed value depends on the circumstances of the measurement. To ensure the precision of the upcoming *in vitro* measurements, the measurement values of the integrated temperature sensors were compared to both an external Pt sensor and an optical fibre-based temperature sensor as well. Figure 49 A compares the displayed temperature values measured by the integrated sensor of the illuminating optrode (called as 'Integrated sensor') and by the simultaneously immersed other optrode (called as 'External sensor') (cf. Figure 29). To check the reliability of external temperature measurement, the arrangement of optical heating setup was calibrated by a fibre optic temperature sensor (see Figure 49 B). The result of this investigation presents that the integrated sensor underestimates the temperature by 24 ± 6%. Since the relation is linear, the difference can be handled by a simple coefficient to express the 'real' temperature values measured by the on-chip integrated temperature sensor. This underestimation is probably caused by the fact that Si is a very good heat-conducting material, and the thin shaft is connected to a relatively large Si backbone substrate, which contributes a strong heat dissipation effect in the experimental arrangement.

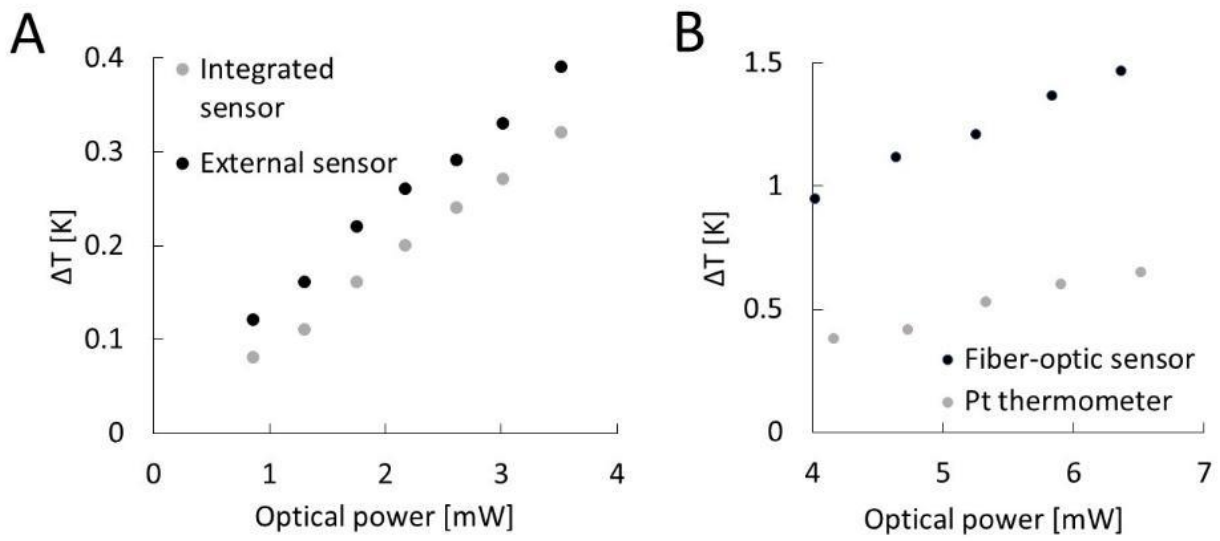

Figure 49: Representative curves to compare the performance of (a) integrated with external temperature sensor and (b) external Pt temperature sensor with fibre-optics based temperature sensor. The distance between (a) the two shafts and (b) the shaft and the fibre was x = 200 µm (cf. Figure 29). [95]*suppl.*

4.4.3 Spatial distribution of temperature

It is essential to determine the spatial distribution of temperature around the light emitting tip, precisely. The measurement results carried out in the *in vitro* setup introduced in chapter 3.7.2 are shown on Figure 51. These experiences on one hand help to ensure the safety limit of optical stimulation during *in vivo* application avoiding any harmful overheat of the tissue, on the other hand, they also help to estimate the optically affected volume of the tissue, which measure is estimated also through the aforementioned multi-physical simulation of my colleagues. Figure 50. shows a simulated temperature distribution around the optrode's shaft in case of implantation in 1300 µm depth in rat somatosensory cortex.

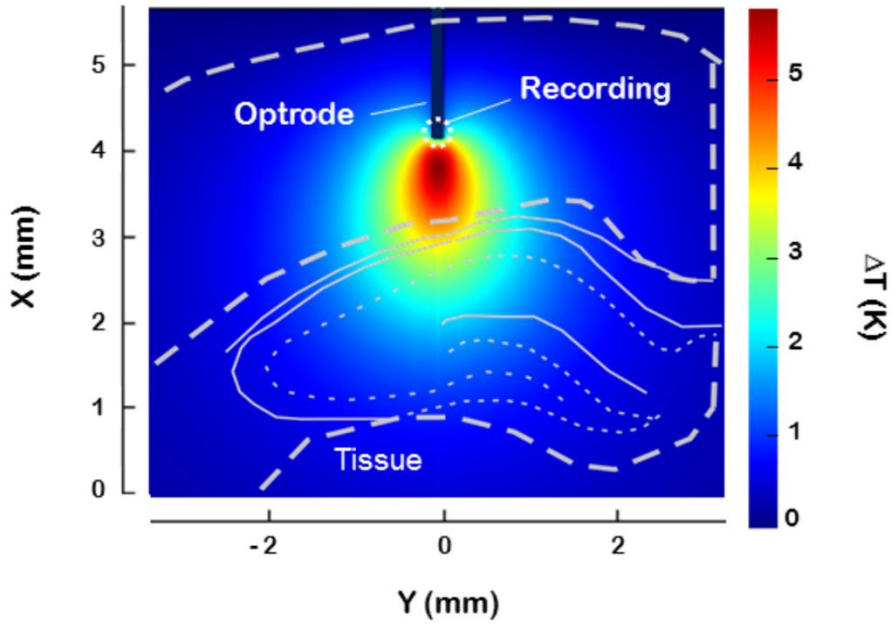

Figure 50: Simulated temperature distribution during stimulus onset around the excited region at 10.5 mW [95].

The full width at half maximum (FWHM) of the distribution of local radiant heating is measured 1020 ± 184 µm along the y axis (x = 200 µm) perpendicular to the shaft (see Fig. 51. A). Figure 51 B shows the distribution of the radiant heating along the axis of the waveguide shaft of the illuminating optrode. Figure 51 C compares the distribution of temperature along two perpendicular axes. The result is in good agreement with the expectations regarding the experiences of optical investigations of the waveguiding. Figure 51 D shows a 2D representation of the distribution of the temperature rise along the two perpendicular axes of Fig. 51. A&B.

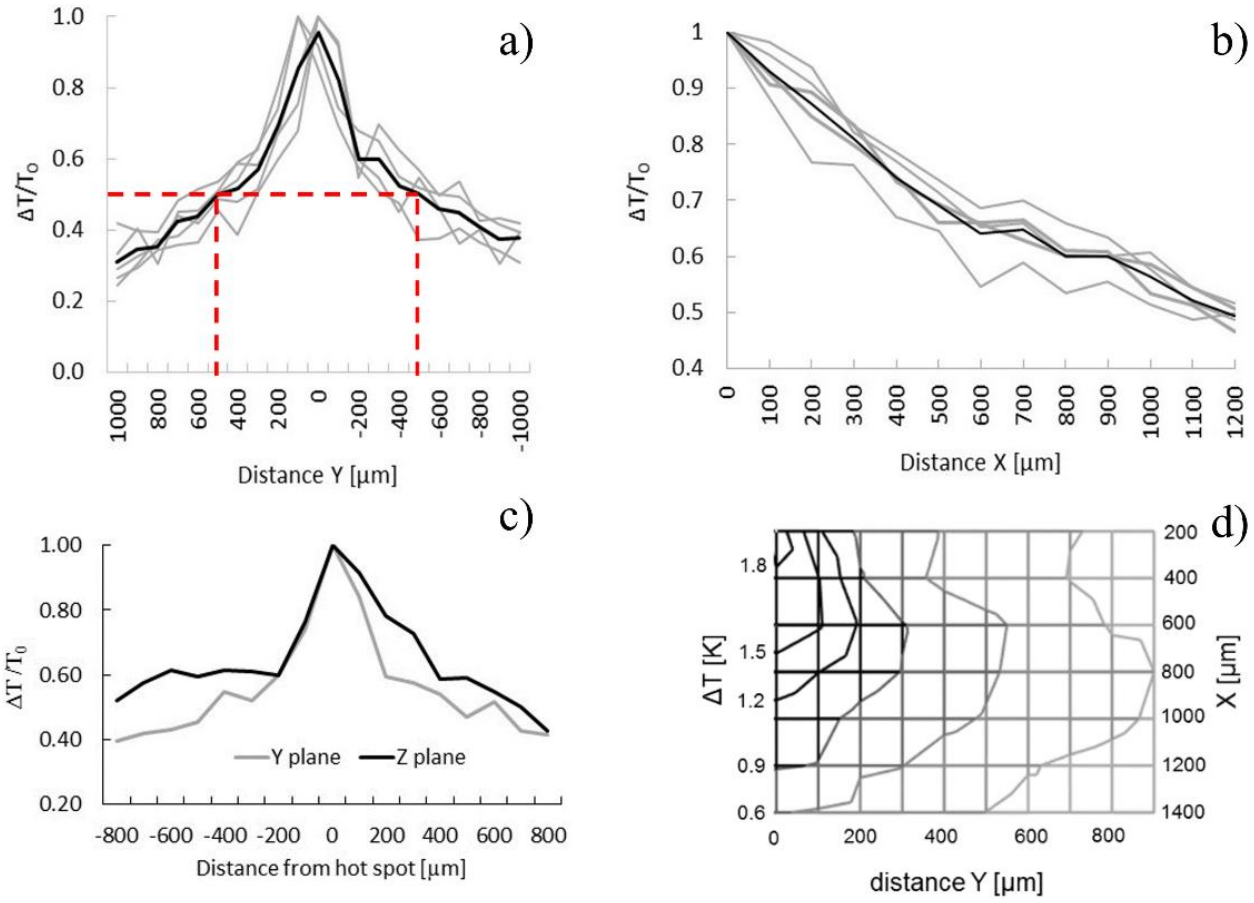

Figure 51: a) Normalized distribution of the temperature elevation along the y axis. Red dashed line helps to recognize the FWHM. b) Normalized distribution of the temperature increase as a function of distance between the tips of the immersed optrode and the external temperature sensor. c) Normalized spatial distribution of optical heating along two perpendicular axes y and z according to Figure 29. d) 2D representation of the distribution of temperature rise along two perpendicular axes x and y. The location of the tip of the shaft is considered the origin of the coordinate system (upper left corner). [95]

4.4.4 Calibration of individual probes for *in vivo* tests

Another important step before *in vivo* application of the optrodes is to calibrate their radiant heating performance. To achieve the desired amount of stimulating light power, adjustment of supply current of the IR light source is necessary. For this reason, I switched a broad range of supply current levels – obviously within the tolerance of the applied instruments – and made a series of absolute optical power measurements of each optrode with a 10 mA resolution. Figure 52 shows representative calibration curves. The combination of these results and the ones plotted on Figure 48 helps to estimate the suitable current level to induce a desired temperature increase in the vicinity of the shaft.

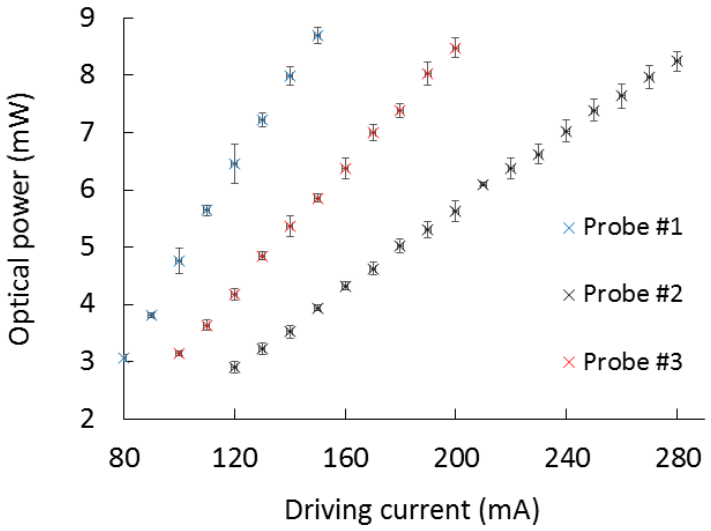

Figure 52: Representative calibration curves of three individual optrodes (averages and standard deviation due to repetition): emitted absolute optical power as a function of supply current of the IR light source. [95]*suppl.*

4.4.5 *In vivo* performance of temperature sensor

Figure 53 shows representative curves of brain temperature measurement during *in vivo* IR stimulation experiment. The excitation waveform was similar to those applied during *in vitro* characterization: after 30 s recording of initial state, the output of the current source of the laser diode was switched on for 60 s then it was switched off to ensure time for cooling down. In the presented case, the level of maximum supply current was set to 315 mA, which produced 13.19 mW optical power emitted from the tip of the implanted optrode. This amount of light stimulus caused about 5 °C maximal temperature elevation in the brain tissue of the rat subject measured by the integrated temperature sensor of the implanted optrode.

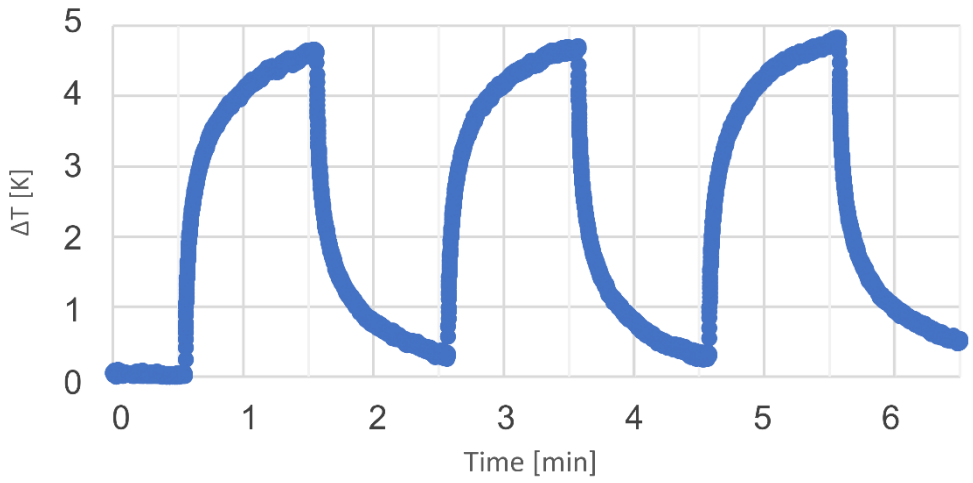

Figure 53: Representative curves of optically induced temperature elevation in rat brain tissue measured by the integrated temperature sensor of the implanted optrode.

4.4.6 Thesis 4.

I developed an automated environment to measure the effective cross-section of optical heating induced by optical absorption in liquid medium. I determined that the full width half maximum of the effective cross-section in perpendicular to the axis of the probe shaft is 1020±184 µm considering a 2.17–3.5 mW optical power range. I proved that the temperature increase (1–4 °C) in the thermally affected region shows a linear dependence on the optical heating power (between 3–9 mW).

Related publication:

Á. C. Horváth, S. Borbély, Ö. C. Boros, L. Komáromi, P. Koppa, P. Barthó, Z. Fekete, "Infrared neural stimulation and inhibition using an implantable silicon photonic microdevice" in *Microsystems & Nanoengineering*, vol. 6, no. 44, 2020., DOI: 10.1038/s41378-020-0153-3

4.5 *In vivo* optical stimulation

In this section, experimental results of *in vivo* IR optical stimulation are discussed. First, comparable investigations are introduced from the relevant literature, which will be followed by my results. *In vivo* validation of the optrodes were carried out in collaboration with colleagues in RCNS, who have also contributed significantly to data analysis and

representation of the results. These data are presented here to show the reliable functionality of the optrodes during acute *in vivo* experimental conditions.

Unit activity recording can be found on Fig. 54. Xia and Nyberg applied 1550 nm CW laser illumination to investigate safety, efficiency and mechanism of it in rat cortical neural networks cultured *in vitro* [90]. Their observed optical power levels are 2, 28, 56, 83 and 111 mW, most of them are much higher (at least twice) than the optical power levels used by our group (cf. Fig. 61.). Figure 54. shows that both the number and amplitude of spikes likewise decrease when the illumination power is larger than 83 mW.

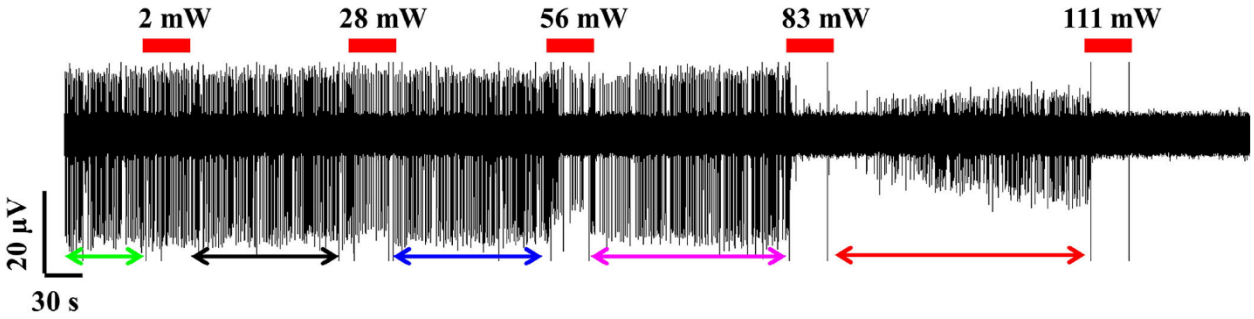

Figure 54: Example of unit activity responses of rat cortical neurons to IR illumination recorded in vitro. *Red rectangle bars show the presence of IR light. Remarkable changes are discernible in case of 83 mW or higher power laser illumination. Adapted from* [90]

Figure 55. compares the shape of the *in vitro* action potential signals before and after the laser illumination with different optical power levels presented in [90]. Light green marks the reference shape before any illumination (called baseline by Xia & Nyberg), and black, blue, magenta and red mark the shapes after illumination with the different optical power levels (2, 28, 56 and 83 mW, respectively). As clearly observable, illumination with the three lower optical power levels resulted in action potential shapes similar to that of the original, while after the 83 mW illumination the signal did not recover to the baseline. Comparing these results with the unit activity recording shown on Fig. 54. (colours help to find correspondences), shows the reason why the shape after 111 mW illumination is not depicted on Fig. 55.: this level of optical power caused damages to neurons.

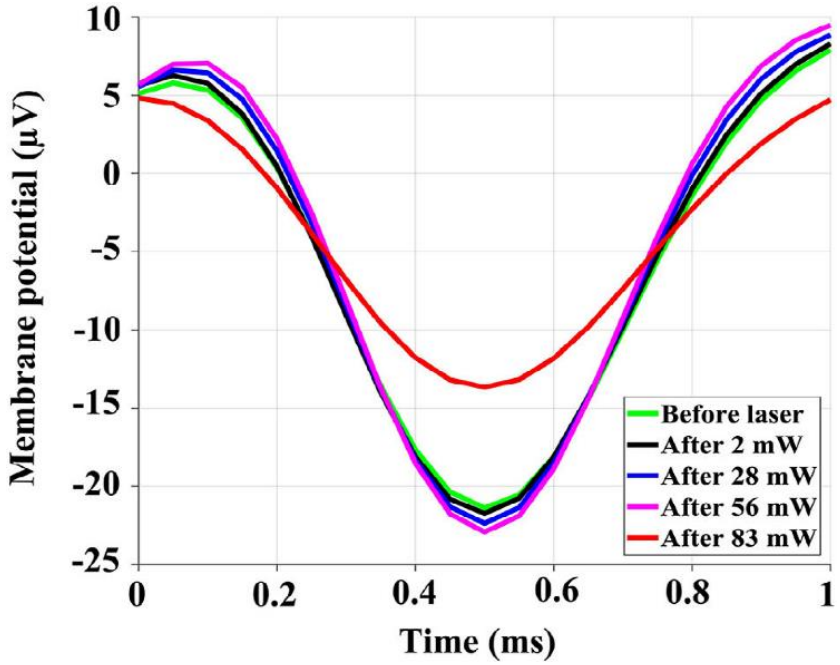

Figure 55: Comparison of the average shape of the spikes in vitro *before and after laser illumination with the labelled different optical power levels, adapted from* [90].

Figure 56. shows the *in vivo* results of Cayce et al. [123]. They illuminated the somatosensory cortex of anaesthetized rats with 1875 nm laser pulses. They found an immediate inhibitory effect, which appeared to remain present over many (400) trials.

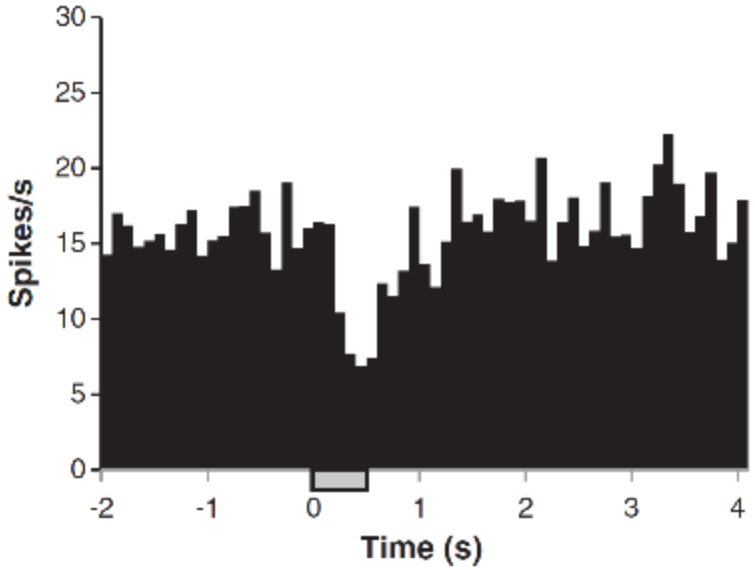

Figure 56: Inhibitory effect of IR pulses in rat somatosensory cortex (PSTH summation of 400 trials). Laser parameters: λ=1.875 μm, repetition rate=200 Hz, pulse train duration=500 ms, pulse width=250 μs, radiant exposure=0.0549 J/cm^2, spot size=850 μm. Inter-trial interval was 15 s. Rectangle bar represents the timing of IR stimulus. Adapted from [123]

Figure 57. also shows reversible suppression of neural activity [91]. These *in vitro* results are recorded from rat cortical cell culture, using a CW laser of 1550 nm. One clear conclusion of these results (on Fig. 54–57.) is the confirmation of the well-known statement of the discoverers of INS [22] that IR illumination has no harmful effect on neural activity within a certain range of optical stimulation power. Xia and Nyberg highlighted their findings on Fig. 57. C&D. Inset pictures show that 5 s after the immediate suppression, the degree of inhibition was attenuated a bit. Note that after a period 1.5 times longer than the duration of laser stimulus, the level of neural activity returns to its initial state from inhibition (cf. Fig. 61 b): after 90 s on Fig. 57. C&D (around 150 s on time scale).

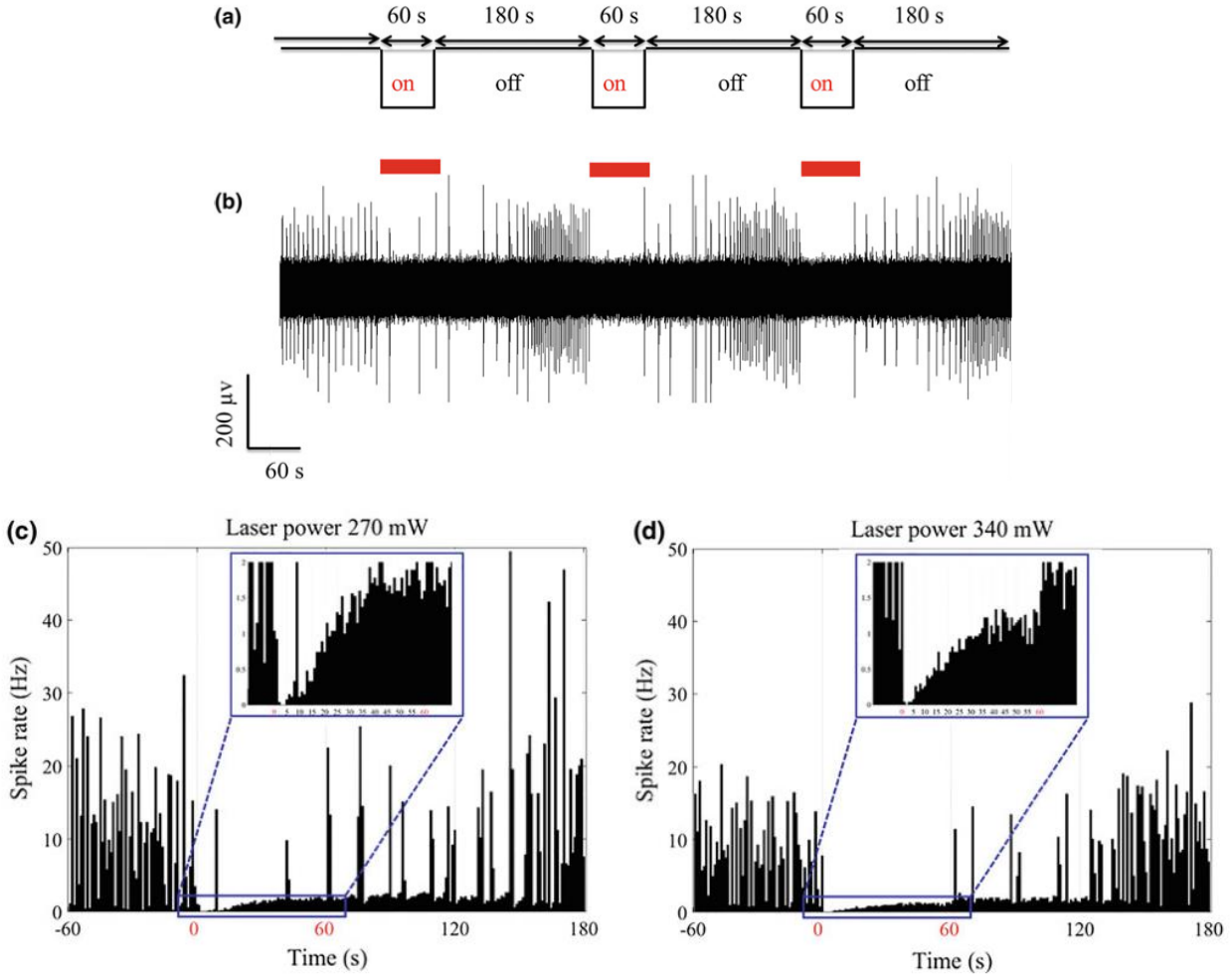

Figure 57: a) Schematic of 3 times repeated laser irradiation. b) Raw data of repeating suppression of spontaneous neural firing from a single electrode in vitro *(power of 1550 nm CW laser: 270 mW). c-d) Spike rate plots for neurons exposed to 60 s CW IR laser at different optical power levels (recording electrodes: n=9; stimulation repetition: 3 times; red fonts 0 and 60: laser ON and laser OFF; bin size: 1 s.). The insets in c) and d) magnify the time period 0–60 s during the IR illumination. Adapted from* [91]

Figure 58. shows a graph, which details the degree of inhibition caused by different optical power illumination of 1550 nm CW laser *in vitro* [91]. Please note the illumination power levels corresponding to each degree of inhibition, the importance of it will be discussed later in this chapter.

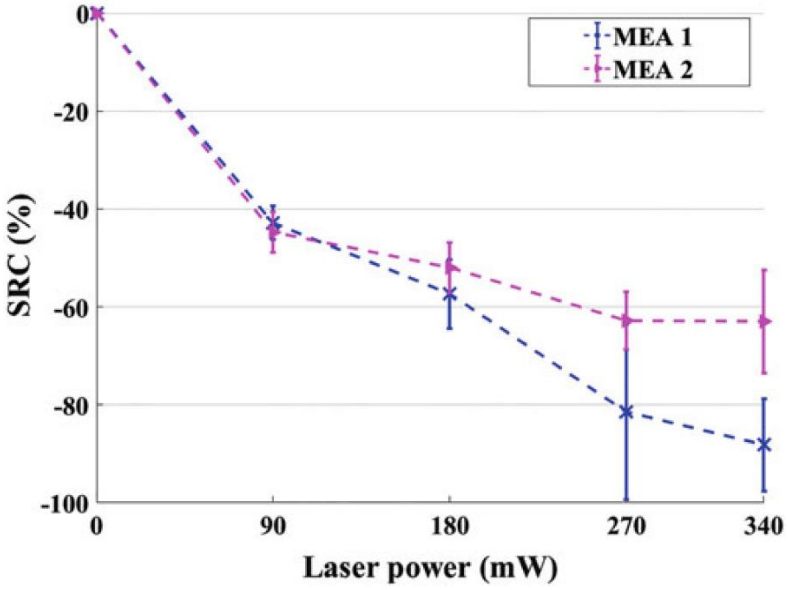

Figure 58: Quantification of spike rate changes in vitro *(SRC, mean ± SD) measured by two microelectrode array (MEA) samples at the different laser power, adapted from* [91].

In the following section, I will present the experimental results obtained by the *in vivo* application of the IR optrode. The compared data shown (Figure 59, 60 and 61), are originated from the brain tissue at depths of 1300, 1600 and 2600 µm, (a-c) on each figure, respectively. Recordings in 1600 µm depth was realized by the commercial Si laminar probe, the other two cases were made by the IR optrode in question. Optical power values are derived from similar absolute optical power measurements like described in chapter 3.6.3, when the optical power of the IR light emitted from the tip of the optrode was measured.

Figure 59. shows LFP and unit activity signal waveforms recorded from different depths of the rat brain using the optrode in question. The presented sections show the signals before and during the thermal stimulus. The lack of any significant changes in the waveforms after stimulus onset proves that the optical stimulation with the applied 1550 nm wavelength does not produce any artefact in the *in vivo* recordings.

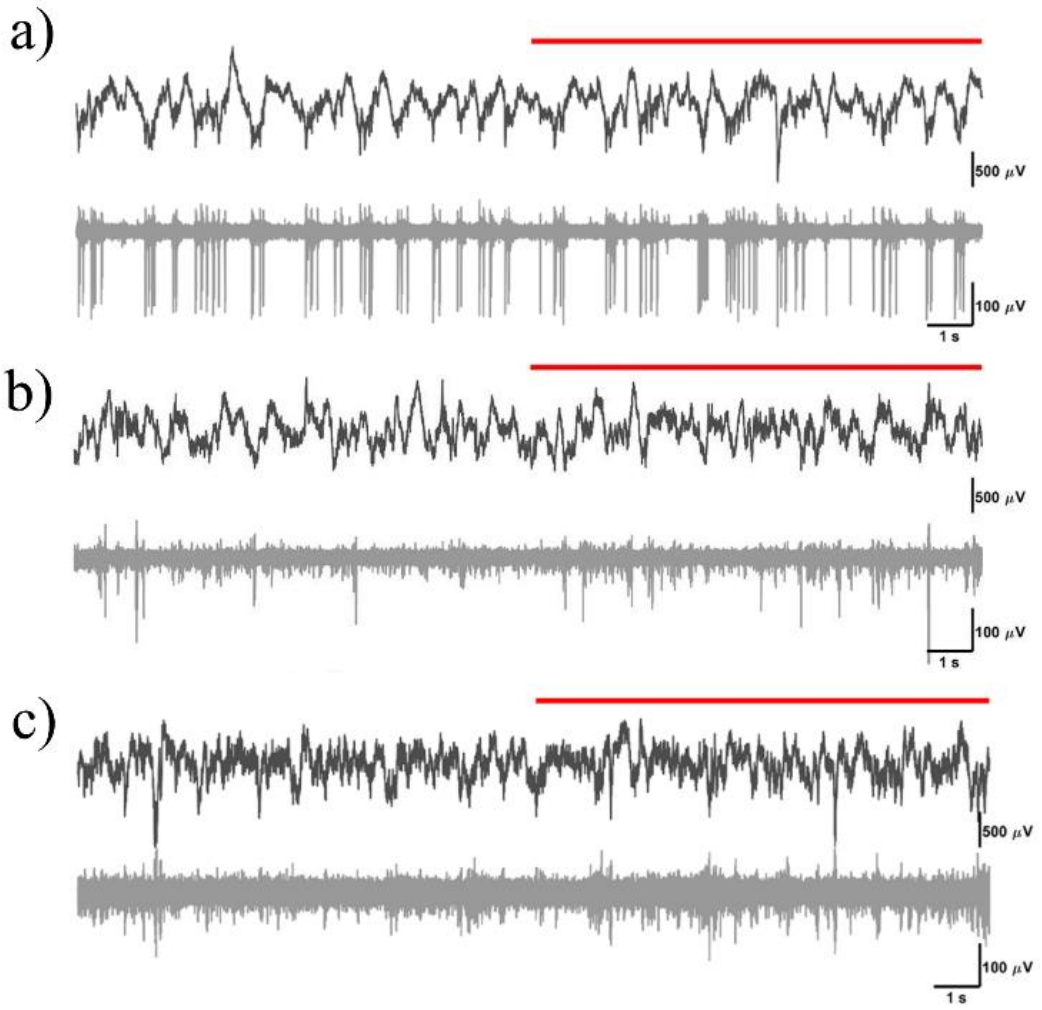

Figure 59: Local field potential (top, black) and unit activity (bottom, grey) waveforms before and during optical heating. Red line on each figure shows the presence of heating stimulus with P_a=6.9 mW, P_b=8.5 mW and P_c=13.4 mW. Implantation depths: (a) 1300 μm, (b) 1600 μm (cortex) and (c) 2600 μm (hippocampus). Data on (a) and (c) are recorded from the optrode while (b) shows the recordings of the commercial Si probe. [95]

The top line on Fig. 60. compares the shape of the action potential signals before, during and after the thermal stimulus *in vivo*. The fact that all shapes are very similar proves that the applied way of deep-brain stimulation remained within the stimulation power range which has no harmful effect on the neural cells (cf. Fig. 55.). Another conclusion of Fig. 60. is that the signal on the IR optrode seems to be less noisy than the signal on the commercial Si probe (cf. Fig. 60. B&C). In the showed cases, cell-probe distance may have also prevalent effect on the noise conditions of the recordings not only the structural and fabrication differences between the two devices. However, it is observable that the signal-

to-noise ratio of the IR optrode is in a similar order of magnitude as that of the commercially available Si electrode. The bottom line on Fig. 60. shows the autocorrelograms of the activity of three single neurons clustered from the corresponding recording sites on Fig. 59. An autocorrelogram is used to investigate whether the clustered signals are really originated from the same neuron or not. To validate the goodness of signal sorting, we may just check the short time period before and after the zero instant (a few milliseconds around 0 ms): within this short period we should not find any action potentials because of the refractory period of the neurons (when sodium channels are in the inactive state). So, if we can plot an ordinary autocorrelogram from the unit activity recorded by the neural implant in question, it means that the inspected device is able to record the activity of a single neuron. These mentioned autocorrelograms in the bottom line of Fig. 60. verify that the recording sites with their increased specific surface area make the recording of individual spikes possible.

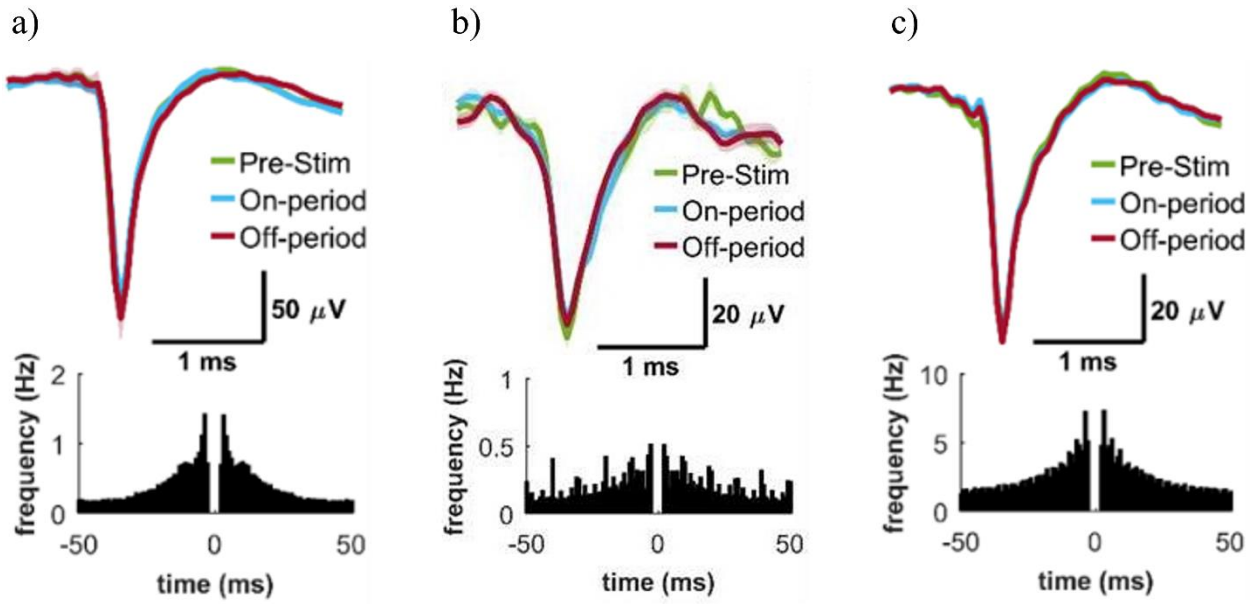

Figure 60: Waveforms (top, coloured) and autocorrelograms (bottom, black) of single units clustered from the same recording sites on Figure 59. Implantation depths: (a) 1300 μm, (b) 1600 μm (cortex) and (c) 2600 μm (hippocampus). Data on (a) and (c) are recorded from the optrode while (b) shows the recordings of the commercial Si probe. [95]

Left column on Fig. 61 shows changes in firing rate of *in vivo* multiunit activity for various excitation powers (in other words, the time series of normalized spike rate changes as a function of IR optical power). Right column on Fig. 61 shows average spike rate difference

across trials. (This type of representation is often referred as ‘heat map’ of the trials which nomenclature might be confusing in our case when the observation of thermal modality is also proceeded but this is not the case here.) Each row of the large rectangular field represents one of the 12–15 trials in which colours indicate different levels of neural activity induced by the IR illumination. The last row means the average of the others. Multiunit activity at 1300 μm depth in the cortex showed a significant increase at all optical power values ($p < 0.01$ for 6.9, 8.5, 10.5 mW, Fig. 61 a). However, the multiunit activity at 1600 μm, was suppressed throughout the stimulus at high optical power ($p < 0.01$ for 6.9, 8.5, 10.5 mW, Fig. 61 b) up to 50% suppression rate. A similar protocol at 2600 μm in the hippocampus caused an increase in multiunit activity at high power stimuli ($p < 0.01$ for 2.8, 7.1, 10.7, 13.4 mW, Fig. 61 c). These results also prove that the applied IR stimulation has no harmful effect on the tissue, as all modulation was found to be reversible. Another important conclusion of Fig. 61. b) is that the equivalent degree of optically induced neural inhibition was reached in our case with less than a tenth of the laser power used by Xia and Nyberg (cf. Fig. 58.). And also, as it is highlighted on Fig. 57. C&D, the level of neural activity returned to its initial state from inhibition similarly after a period 1.5 times longer than the duration of laser stimulus: after 3 min on Fig. 61. b) (around 5 min on time scale). It is discernible on the figures that the neural response to the IR stimulus is diverse and based on the type of affected neural group. On top of that, these results show that the IR optrode is definitely able to investigate this dependence of neural activity on local temperature, and furthermore, at a single cell resolution.

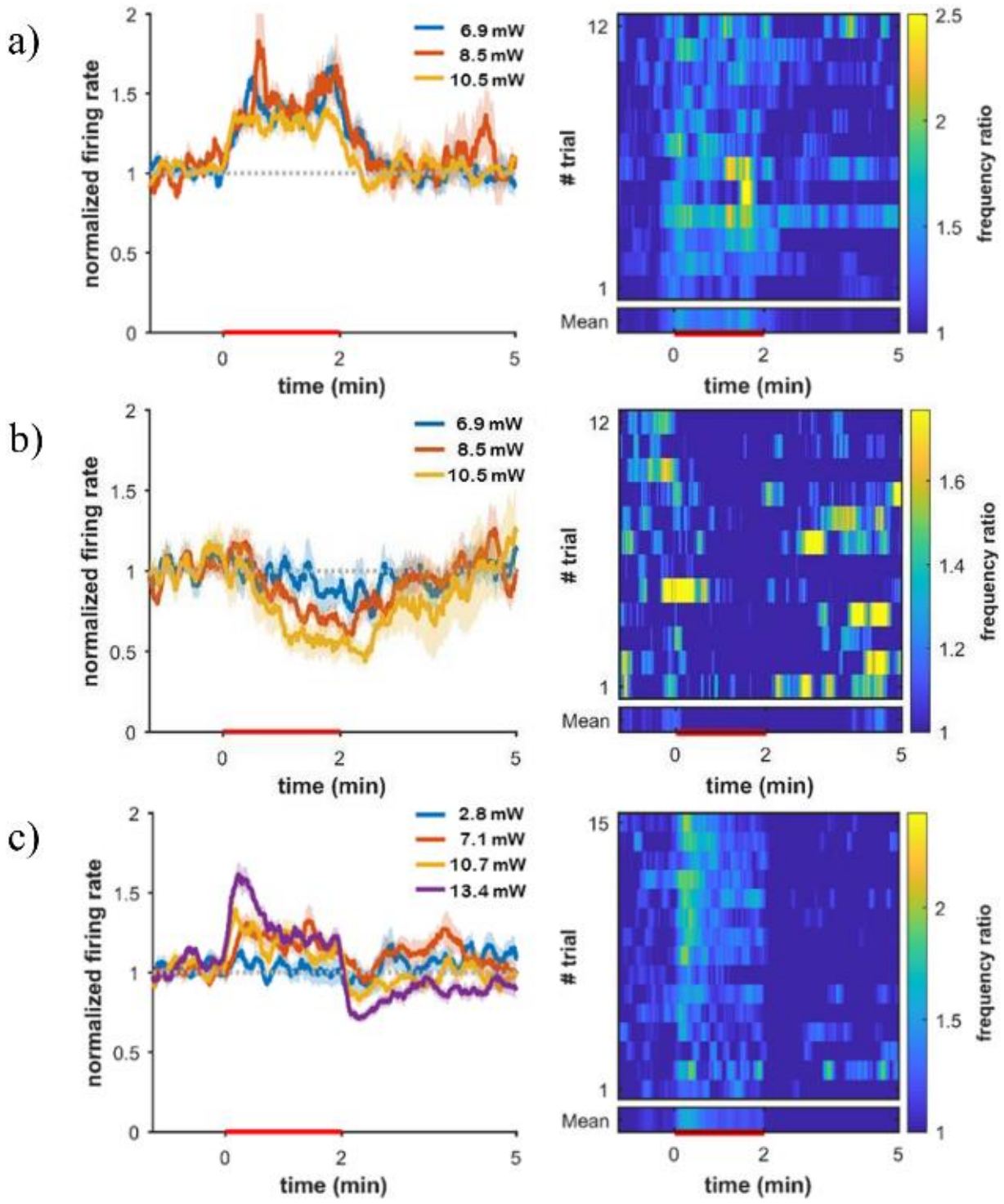

Figure 61: Left: changes in firing rate of multiunit for various excitation powers. Right: average spike rate difference across trials (PSTH). Red line on each figure shows the presence of heating stimulus. Implantation depths: (a) 1300 μm, (b) 1600 μm (cortex) and (c) 2600 μm (hippocampus). Data on (a) and (c) are recorded from the optrode while (b) shows the recordings of the commercial Si probe. [95]

Based on the abovementioned graphs and diagrams (Fig. 59, 60 and 61) on neural recordings from the optrodes and the commercial Si laminar probe, there is no doubt that the novel optrode demonstrated here is competitive with other commercially available deep brain implants.

4.5.1 Thesis 5.

I carried out the *in vivo* validation of the device to test all functionalities of the IR optrode. I proved that the recording sites are able to capture single unit activity, and the operation of optical stimulation, concurrently with recording of neuronal signals, causes no electric artefact in the electrophysiological data. I determined that operating a light source of 1550 nm wavelength coupled to the optrode at an optical power between 2.8–13.4 mW, modulation of the spike rate of particular neurons is possible in a safe and, repeatable manner.

Related publication:

Á. C. Horváth, S. Borbély, Ö. C. Boros, L. Komáromi, P. Koppa, P. Barthó, Z. Fekete, "Infrared neural stimulation and inhibition using an implantable silicon photonic microdevice" in *Microsystems & Nanoengineering,* vol. 6, no. 44, 2020., DOI: 10.1038/s41378-020-0153-3

5 Potential applications and benefits

Some recent studies in the literature has shown similar observations, however, these experiments were limited to *in vitro* subjects [90], [124], [125], [126]. For example, in our experiments, the activity of CA1 neurons was recorded during *in vivo* stimulation. There is a growing literature debating the expression, presence and function of thermosensitive receptors and ion channels in the hippocampus [127], [128], however, the in-depth investigation of the underlying phenomena and sensitivity to temperature was out of the scope of my work. Nevertheless, the very recent results of Xia et al [90] suggests that safety limits are far beyond the range we used, therefore the toolset based on the IR optrode in question is definitely able to address questions on cell excitability modulated with tissue temperature.

Besides the above works on the response of brain cells to hyperthermia, studies on infrared neural stimulation (INS) and infrared neural inhibition (INI) may also benefit from the use of this photonic microdevice. In particular, the above introduced results indicate that low-energy (in the range of a few mW) irradiation of the intracortical and hippocampal neurons is able to either boost or suppress the firing activity of neurons without creating high spatial or temporal gradient of temperature increase. Nevertheless, the degree of inhibition (decrease in firing rate) in our case of infragranular cells (see Fig. 61. B.) are in the same range as demonstrated *in vitro* by Xia et al at 1550 nm with continuous wave laser light (see Fig. 58.) [90] and *in vivo* by Cayce et al at 1875 nm with pulsed infrared irradiation (see Fig. 56.) [123].

The work presented here contributed the successful developments of research projects supported by the National Research, Development and Innovation Office (grant IDs: KTIA NAP B 3 2015-0004; 2017_1.2.1_NKP-2017-00002) and the New National Excellence Program of Hungary (ÚNKP-18-3-I-OE-90; ÚNKP-19-3-I-OE-36).

6 Conclusion

The aim of my PhD work was to develop a multimodal Michigan-type (in-plane) IR optrode capable for simultaneous deep-brain electrophysiological recording and temperature sensing. In this thesis, I presented my research from the motivations and concepts to functional testing of the prototypes through the introduction and explanation of applied methods and completed experiments. I determined the electrical characteristics of the electrophysiological recording sites of the IR optrode by electrochemical impedance spectroscopy. Based on optical measurements, I gave evidence on the functionality of the integrated waveguides even holding sensors to record electrical and thermal signals from the tissue. The final validation of the microtool in the rat brain provided further insights into device operation, and along this unique test, the proper, high-quality recording of cellular activity, tissue temperature and concurrent delivery of IR light to target tissue was demonstrated first time. It can be confidently stated in the light of the literature and the showed results, that the novel optrode demonstrated here is competitive with other commercially available deep brain implants.

7 Acknowledgement

First, I would like to thank my supervisor, Dr. Zoltán Fekete, not only for his professional guidelines and advices but his acting as an empathetic boss during these four years of my PhD and the seven years of my scientific career.

I thank the colleagues of Department of Atomic Physics, Budapest University of Technology & Economics, Budapest, Hungary for the four-year-long and hopefully continuing cooperation, especially:

- Dr. Csanád Örs Boros, who built the indispensable simulation of the IR optrode;
- his supervisors, Dr. Pál Koppa, the head of department and Dr. Szabolcs Beleznai for their useful suggestions that advanced our common cause;
- Dr. Örs Sepsi, who helped me getting to know optical measurement methods and theories, and had influential role in optical experimental setup assembly.

I would like to express my thanks to the cleanroom personnel of the Microsystems Laboratory of the Institute for Technical Physics & Material Science (MFA) in the Centre for Energy Research of the Eötvös Loránd Research Network, Budapest, Hungary for their necessary work on micro-machining. I specially thank:

- Károlyné Payer for her valuable proposals on perfecting wet chemical polishing process;
- Gabriella Bíró for her assistance and in some cases substitution during wet chemical tasks.

I thank their support and cooperation of my colleagues in MFA, namely:

- Dr. Anita Zátonyi for teaching me the electroplating of porous platinum and her assistance during soaking tests;
- Attila Nagy for assembling the microimplants and tiny connectors for my measurements with inimitable precision;
- Csaba Lázár for preparing those numerous custom-made stuffs, essential for lab work.

I thank the colleagues of Sleep Oscillations Research Group of the Research Centre for Natural Sciences of the Eötvös Loránd Research Network, Budapest, Hungary for the more than four-year-long and hopefully continuing cooperation, especially:

- Dr. Péter Barthó group leader for welcoming my research and for his encouraging words during evening periods of long workdays of *in vivo* experiments;

- Dr. Sándor Borbély for making surgeries and his high-quality contribution in processing and evaluation of recorded electrophysiological data;
- Dr. Márton Csernai for his assistance in calibration of integrated temperature sensors.

I thank Attila János Chalupa, Imre Tóth and Márton Pesztránszki for their assistance in optical fibre polishing, Borisz Juhász for contribution in PCB design and Iván Gresits for providing the fibre-optics based temperature sensor.

I also thank my supervised students (Szabolcs Kiss, Alina Ivanenko, Márton Pesztránszki) for asking questions what helped me concentrating on the essence.

And last but not least I thank my family and friends for keeping and affirming private life background without which not only the presented work but a life worthy for a human is unthinkable.

8 References

[1] M. Rizzone *et al.*, "Deep brain stimulation of the subthalamic nucleus in Parkinson's disease: effects of variation in stimulation parameters," *J. Neurol. Neurosurg. Psychiatry*, vol. 71, no. 2, pp. 215–219, Aug. 2001.

[2] P. Temperli, J. Ghika, J.-G. Villemure, P. R. Burkhard, J. Bogousslavsky, and F. J. G. Vingerhoets, "How do parkinsonian signs return after discontinuation of subthalamic DBS?," *Neurology*, vol. 60, no. 1, pp. 78–81, 2003.

[3] S. L. F. Owen, A. L. Green, J. F. Stein, and T. Z. Aziz, "Deep brain stimulation for the alleviation of post-stroke neuropathic pain," *Pain*, vol. 120, pp. 202–206, 2006.

[4] R. Fisher *et al.*, "Electrical stimulation of the anterior nucleus of thalamus for treatment of refractory epilepsy," *Epilepsia*, vol. 51, no. 5, pp. 899–908, 2010.

[5] T. Chen *et al.*, "Clinical outcomes following awake and asleep deep brain stimulation for Parkinson disease," *J. Neurosurg.*, vol. 16, pp. 1–12, 2018.

[6] S. Martinoia, L. Bonzano, M. Chiappalone, and M. Tedesco, "Electrophysiological activity modulation by chemical stimulation in networks of cortical neurons coupled to microelectrode arrays: A biosensor for neuropharmacological applications," *Sensors Actuators, B Chem.*, vol. 108, no. 1–2 SPEC. ISS., pp. 589–596, Jul. 2005.

[7] V. Oldfield, G. M. Keating, and C. M. Perry, "Rasagiline," *Drugs*, vol. 67, pp. 1725–1747, 2007.

[8] M. A. Nitsche, F. Müller-Dahlhaus, W. Paulus, and U. Ziemann, "The pharmacology of neuroplasticity induced by non-invasive brain stimulation: building models for the clinical use of CNS active drugs," *J. Physiol.*, vol. 590, no. 19, pp. 4641–4662, Oct. 2012.

[9] C. Liu, N. Lin, Y. Song, and X. Cai, "A planar microelectrode array modified by nanoparticles for monitoring of electrophysiological activity of cortical neurons modulated by chemical stimulation," *Proc. IEEE Conf. Nanotechnol.*, pp. 980–984, 2013.

[10] S. Borbély *et al.*, “Arctigenin reduces neuronal responses in the somatosensory cortex via the inhibition of non-NMDA glutamate receptors,” *Neurochem. Int.*, vol. 97, pp. 83–90, Jul. 2016.

[11] M. Vandecasteele *et al.*, “Optogenetic activation of septal cholinergic neurons suppresses sharp wave ripples and enhances theta oscillations in the hippocampus,” *Proc. Natl. Acad. Sci. U. S. A.*, vol. 111, no. 37, pp. 13535–13540, Sep. 2014.

[12] Y. Son *et al.*, “In vivo optical modulation of neural signals using monolithically integrated two-dimensional neural probe arrays,” *Sci. Rep.*, vol. 5, p. 15466, Oct. 2015.

[13] M. H. Wang *et al.*, “Three-dimensional drivable optrode array for high-resolution neural stimulations and recordings in multiple brain regions,” *Biosens. Bioelectron.*, vol. 131, pp. 9–16, Apr. 2019.

[14] M. S. George *et al.*, “Brain stimulation for the treatment of psychiatric disorders,” *Curr. Opin. Psychiatry*, vol. 20, no. 3, pp. 250–254, May 2007.

[15] S. Eljamel and K. V. Slavin, *Neurostimulation: Principles and Practice*. Wiley-Blackwell, 2013.

[16] S. Shoham and K. Deisseroth, “Special issue on optical neural engineering: advances in optical stimulation technology,” *J. Neural Eng.*, vol. 7, no. 4, p. 040201, Aug. 2010.

[17] E. Iseri and D. Kuzum, “Implantable optoelectronic probes for in vivo optogenetics,” *J. Neural Eng.*, vol. 14, no. 3, p. 031001, Mar. 2017.

[18] S. B. Goncalves, J. F. Ribeiro, A. F. Silva, R. M. Costa, and J. H. Correia, “Design and manufacturing challenges of optogenetic neural interfaces: a review,” *J. Neural Eng.*, vol. 14, no. 4, p. 041001, 2017.

[19] M. Chernov and A. W. Roe, “Infrared neural stimulation: a new stimulation tool for central nervous system applications,” *Neurophotonics*, vol. 1, no. 1, 2014.

[20] M. G. Shapiro, K. Homma, S. Villarreal, C.-P. Richter, and F. Bezanilla, “Infrared light excites cells by changing their electrical capacitance,” *Nat. Commun.*, vol. 3, p. 736, 2012.

[21] S. L. Jacques, “Optical properties of biological tissues: a review,” *Phys. Med. Biol.*, vol. 58, 2013.

[22] J. Wells *et al.*, “Optical stimulation of neural tissue in vivo,” *Opt. Lett.*, vol. 30, no. 5, p. 504, Mar. 2005.

[23] J. M. Cayce, R. M. Friedman, G. Chen, E. D. Jansen, A. Mahadevan-Jansen, and A. W. Roe, “Infrared neural stimulation of primary visual cortex in non-human primates,” *Neuroimage*, vol. 84, pp. 181–190, Jan. 2014.

[24] Á. C. Horváth, Ö. C. Boros, S. Beleznai, Ö. Sepsi, P. Koppa, and Z. Fekete, “A multimodal microtool for spatially controlled infrared neural stimulation in the deep brain tissue,” *Sensors Actuators, B Chem.*, vol. 263, pp. 77–86, 2018.

[25] M. Mehregany, “High-aspect-ratio photolithography for MEMS applications,” *J. Microelectromechanical Syst.*, vol. 4, no. 4, pp. 220–229, 1995.

[26] I. W. Rangelow, “Dry etching-based silicon micro-machining for MEMS,” *Vacuum*, vol. 62, no. 2–3, pp. 279–291, Jun. 2001.

[27] O. Sneh, R. B. Clark-Phelps, A. R. Londergan, J. Winkler, and T. E. Seidel, “Thin film atomic layer deposition equipment for semiconductor processing,” *Thin Solid Films*, vol. 402, no. 1–2, pp. 248–261, Jan. 2002.

[28] T. M. Adams and R. A. Layton, *Introductory MEMS: Fabrication and applications*. Springer US, 2010.

[29] S. M. Sze and M.-K. Lee, *Semiconductor Devices: Physics and Technology*. Wiley, 2012.

[30] Z. Fekete, “Recent advances in silicon-based neural microelectrodes and microsystems: a review,” *Sensors Actuators B Chem.*, vol. 215, pp. 300–315, Aug.

2015.

[31] K. D. Wise, J. B. Angell, and A. Starr, “An Integrated-Circuit Approach to Extracellular Microelectrodes,” *IEEE Trans. Biomed. Eng.*, vol. BME-17, no. 3, pp. 238–247, 1970.

[32] K. Wise and J. Angell, “A microprobe with integrated amplifiers for neurophysiology,” pp. 100–101, Mar. 2005.

[33] J. L. Shobe, L. D. Claar, S. Parhami, K. I. Bakhurin, and S. C. Masmanidis, “Brain activity mapping at multiple scales with silicon microprobes containing 1,024 electrodes,” *J. Neurophysiol.*, vol. 114, no. 3, pp. 2043–2052, Sep. 2015.

[34] A. Tooker *et al.*, “Towards a Large-Scale Recording System: Demonstration of Polymer-Based Penetrating Array for Chronic Neural Recording,” *2014 36th Annu. Int. Conf. IEEE Eng. Med. Biol. Soc. EMBC 2014*, pp. 6830–6833, Nov. 2014.

[35] A. Zátonyi *et al.*, “A softening laminar electrode for recording single unit activity from the rat hippocampus,” *Sci. Rep.*, vol. 9, no. 1, Dec. 2019.

[36] A. Schander *et al.*, “Design and fabrication of novel multi-channel floating neural probes for intracortical chronic recording,” *Sensors Actuators, A Phys.*, vol. 247, pp. 125–135, Aug. 2016.

[37] B. C. Raducanu *et al.*, “Time Multiplexed Active Neural Probe with 1356 Parallel Recording Sites,” *Sensors*, vol. 17, no. 10, p. 2388, Oct. 2017.

[38] K. Najafi and K. D. Wise, “An Implantable Multielectrode Array with On-Chip Signal Processing,” *IEEE J. Solid-State Circuits*, vol. 21, no. 6, pp. 1035–1044, 1986.

[39] S. Spieth *et al.*, “A floating 3D silicon microprobe array for neural drug delivery compatible with electrical recording,” *J. Micromechanics Microengineering*, vol. 21, no. 12, Dec. 2011.

[40] A. Pongrácz, Z. Fekete, G. Márton, Z. Bérces, I. Ulbert, and P. Fürjes, “Deep-brain

silicon multielectrodes for simultaneous in vivo neural recording and drug delivery," *Sensors Actuators, B Chem.*, vol. 189, pp. 97–105, 2013.

[41] M. D. Johnson, R. K. Franklin, K. A. Scott, R. B. Brown, and D. R. Kipke, "Neural Probes for Concurrent Detection of Neurochemical and Electrophysiological Signals in vivo," *Annu. Int. Conf. IEEE Eng. Med. Biol. - Proc.*, vol. 7 VOLS, pp. 7325–7328, 2005.

[42] G. Xiao *et al.*, "In situ detection of neurotransmitters and epileptiform electrophysiology activity in awake mice brains using a nanocomposites modified microelectrode array," *Sensors Actuators, B Chem.*, vol. 288, pp. 601–610, Jun. 2019.

[43] S. Kanno *et al.*, "Multiple Optical Stimulation to Neuron Using Si Opto-Neural Probe with Multiple Optical Waveguides and Metal-cover for Optogenetics," in *35th Annual International Conference of the IEEE EMBS*, 2013, pp. 253–256.

[44] K. Kampasi *et al.*, "Fiberless multicolor neural optoelectrode for in vivo circuit analysis," *Sci. Rep.*, vol. 6, no. 1, p. 30961, 2016.

[45] J. Blakeley, "Drug delivery to brain tumors," *Curr. Neurol. Neurosci. Rep.*, vol. 8, no. 3, pp. 235–241, May 2008.

[46] R. K. Upadhyay, "Drug Delivery Systems, CNS Protection, and the Blood Brain Barrier," *Biomed Res. Int.*, vol. 2014, 2014.

[47] K. H. Lee *et al.*, "WINCS Harmoni: Closed-loop dynamic neurochemical control of therapeutic interventions," *Sci. Rep.*, vol. 7, 2017.

[48] H. N. Schwerdt *et al.*, "Subcellular Probes for Neurochemical Recording from Multiple Brain Sites," *Lab Chip*, vol. 17, no. 6, pp. 1104–1115, Mar. 2017.

[49] A. L. Benabid, S. Chabardes, J. Mitrofanis, and P. Pollak, "Deep brain stimulation of the subthalamic nucleus for the treatment of Parkinson's disease," *Lancet Neurol.*, vol. 8, no. 1, pp. 67–81, Jan. 2009.

[50] G. Bonmassar, S. W. Lee, D. K. Freeman, M. Polasek, S. I. Fried, and J. T. Gale, "Microscopic magnetic stimulation of neural tissue," *Nat. Commun.*, vol. 3, p. 921, 2012.

[51] M. D. Menz, Ö. Oralkan, P. T. Khuri-Yakub, and S. A. Baccus, "Precise neural stimulation in the retina using focused ultrasound," *J. Neurosci.*, vol. 33, no. 10, pp. 4550–4560, Mar. 2013.

[52] A. M. Aravanis *et al.*, "An optical neural interface: in vivo controlof rodent motor cortex with integrated fiberoptic and optogenetic technology," *J. Neural Eng.*, vol. 4, no. 3, 2007.

[53] A. R. Adamantidis, F. Zhang, A. M. Aravanis, K. Deisseroth, and L. De Lecea, "Neural substrates of awakening probed with optogenetic control of hypocretin neurons," *Nature*, vol. 450, no. 7168, pp. 420–424, Nov. 2007.

[54] F. Zhang *et al.*, "Optogenetic interrogation of neural circuits: technology for probing mammalian brain structures," *Nat. Protoc.*, vol. 5, no. 3, pp. 439–456, Mar. 2010.

[55] P. Anikeeva *et al.*, "Optetrode: a multichannel readout for optogenetic control in freely moving mice," *Nat. Neurosci.*, vol. 15, no. 1, pp. 163–170, Jan. 2012.

[56] M. R. Warden, J. A. Cardin, and K. Deisseroth, "Optical Neural Interfaces," *Annu. Rev. Biomed. Eng.*, vol. 16, no. 1, pp. 103–129, Jul. 2014.

[57] M. Schwaerzle, O. Paul, and P. Ruther, "Compact silicon-based optrode with integrated laser diode chips, SU-8 waveguides and platinum electrodes for optogenetic applications," *J. Micromechanics Microengineering*, vol. 27, no. 6, p. 065004, Jun. 2017.

[58] H. Cao, L. Gu, S. K. Mohanty, and J. C. Chiao, "An Integrated μLED Optrode for Optogenetic Stimulation and Electrical Recording," *IEEE Trans. Biomed. Eng.*, vol. 60, no. 1, pp. 225–229, 2013.

[59] F. Wu, E. Stark, P. C. Ku, K. D. Wise, G. Buzsáki, and E. Yoon, "Monolithically Integrated μLEDs on Silicon Neural Probes for High-Resolution Optogenetic Studies

in Behaving Animals," *Neuron*, vol. 88, no. 6, pp. 1136–1148, 2015.

[60] S. B. Goncalves *et al.*, "LED Optrode with Integrated Temperature Sensing for Optogenetics," *Micromachines*, vol. 9, no. 9, 2018.

[61] S. Royer, B. V. Zemelman, M. Barbic, A. Losonczy, G. Buzsáki, and J. C. Magee, "Multi-array silicon probes with integrated optical fibers: Light-assisted perturbation and recording of local neural circuits in the behaving animal," *Eur. J. Neurosci.*, vol. 31, no. 12, pp. 2279–2291, 2010.

[62] H. Park *et al.*, "The First Neural Probe Integrated with Light Source (Blue Laser Diode) for Optical Stimulation and Electrical Recording," in *33rd Annual International Conference of the IEEE EMBS*, 2011, pp. 2961–2964.

[63] T. Morikawa, T. Harashima, H. Kino, T. Fukushima, and T. Tanaka, "Evaluation of insertion characteristics of less invasive Si optoneural probe with embedded optical fiber," *Jpn. J. Appl. Phys.*, vol. 56, no. 4S, p. 04CM08, Apr. 2017.

[64] I.-J. Cho, H. W. Baac, and E. Yoon, "A 16-SITE NEURAL PROBE INTEGRATED WITH A WAVEGUIDE FOR OPTICAL STIMULATION," in *IEEE 23rd In. Conf. on Micro Electro Mechanical Systems (MEMS)*, 2010, pp. 995–998.

[65] R. Kobayashi *et al.*, "Development of Si Neural Probe with Optical Waveguide for Highly Accurate Optical Stimulation of Neuron," in *Proceedings of the 5th International IEEE EMBS Conference on Neural Engineering*, 2011, pp. 294–297.

[66] F. Wu *et al.*, "An implantable neural probe with monolithically integrated dielectric waveguide and recording electrodes for optogenetics applications," *J. Neural Eng.*, vol. 10, no. 5, p. 056012, 2013.

[67] J. Lee, I. Ozden, Y.-K. Song, and A. V. Nurmikko, "Transparent intracortical microprobe array for simultaneous spatiotemporal optical stimulation and multichannel electrical recording," *Nat. Methods*, pp. 1157–1162, 2015.

[68] T. V. F. Abaya *et al.*, "Characterization of a 3D optrode array for infrared neural stimulation," *Biomed. Opt. Express*, vol. 3, no. 9, p. 2200, 2012.

[69] J. A. Cardin *et al.*, “Targeted optogenetic stimulation and recording of neurons in vivo using cell-type-specific expression of Channelrhodopsin-2,” *Nat. Protoc.*, vol. 5, no. 2, pp. 247–254, 2010.

[70] T. D. Y. Kozai and A. L. Vazquez, “Photoelectric artefact from optogenetics and imaging on microelectrodes and bioelectronics: new challenges and opportunities,” *J. Mater. Chem. B*, vol. 3, no. 25, pp. 4965–4978, 2015.

[71] K. Svoboda and R. Yasuda, “Principles of Two-Photon Excitation Microscopy and Its Applications to Neuroscience,” *Neuron*, vol. 50, no. 6, pp. 823–839, Jun. 2006.

[72] V. Krasnoholovets, “On the theory of the anomalous photoelectric effect stemming from a substructure of matter waves,” *Indian J. Theor. Physic*, vol. 49, no. 1, pp. 1–32, 2001.

[73] A. Forli *et al.*, “Two-Photon Bidirectional Control and Imaging of Neuronal Excitability with High Spatial Resolution In Vivo,” *Cell Rep.*, vol. 22, no. 11, pp. 3087–3098, Mar. 2018.

[74] J. Wells, C. Kao, E. D. Jansen, P. Konrad, and A. Mahadevan-Jansen, “Application of infrared light for in vivo neural stimulation,” *J. Biomed. Opt.*, vol. 10, no. 6, p. 064003, 2005.

[75] J. Wells *et al.*, “Biophysical Mechanisms of Transient Optical Stimulation of Peripheral Nerve,” *Biophys. J.*, vol. 93, no. 7, pp. 2567–2580, Oct. 2007.

[76] E. H. Lothet *et al.*, “Selective inhibition of small-diameter axons using infrared light,” *Sci. Rep.*, vol. 7, no. 1, Dec. 2017.

[77] A. R. Duke, M. W. Jenkins, H. Lu, J. M. McManus, H. J. Chiel, and E. Duco Jansen, “Transient and selective suppression of neural activity with infrared light,” *Sci. Rep.*, vol. 3, no. 2600, 2013.

[78] A. J. Walsh, G. P. Tolstykh, S. Martens, B. L. Ibey, and H. T. Beier, “Action potential block in neurons by infrared light,” *Neurophotonics*, vol. 3, no. 4, 2016.

[79] M. Ganguly, M. W. Jenkins, H. J. Chiel, and E. Duco Jansen, “Modeling the effects of elevated temperatures on action potential propagation in unmyelinated axons,” in *Clinical and Translational Neurophotonics; Neural Imaging and Sensing; and Optogenetics and Optical Manipulation*, 2016, p. 96901O.

[80] M. Ganguly, M. W. Jenkins, E. D. Jansen, H. J. Chiel, E. Duco Jansen, and H. J. Chiel, “Thermal block of action potentials is primarily due to voltage-dependent potassium currents: a modeling study,” *J. Neural Eng.*, vol. 16, no. 3, p. 036020, Jun. 2019.

[81] E. S. Albert *et al.*, “TRPV4 channels mediate the infrared laser-evoked response in sensory neurons,” *J. Neurophysiol.*, vol. 107, no. 12, pp. 3227–3234, 2012.

[82] A. Szallasi, Ed., *TRP Channels as Therapeutic Targets: From Basic Science to Clinical Use*. Academic Press, 2015.

[83] F. N. Hamada *et al.*, “An internal thermal sensor controlling temperature preference in Drosophila,” *Nature*, vol. 454, pp. 217–220, 2008.

[84] S. A. Stanley, J. E. Gagner, S. Damanpour, M. Yoshida, J. S. Dordick, and J. M. Friedman, “Radio-Wave Heating of Iron Oxide Nanoparticles Can Regulate Plasma Glucose in Mice,” *Science (80-.).*, vol. 336, no. 6081, pp. 604–608, 2012.

[85] Y. G. Ermakova *et al.*, “Thermogenetic neurostimulation with single-cell resolution,” *Nat. Commun.*, vol. 8, 2017.

[86] S. Dutz and R. Hergt, “Magnetic nanoparticle heating and heat transfer on a microscale: basic principles, realities and physical limitations of hyperthermia for tumour therapy,” *Int. J. Hyperth.*, vol. 29, no. 8, pp. 790–800, 2013.

[87] A. N. Bashkatov, E. A. Genina, V. I. Kochubey, and V. V. Tuchin, “Optical properties of human skin, subcutaneous and mucous tissues in the wavelength range from 400 to 2000 nm,” *J. Phys. D. Appl. Phys.*, vol. 38, 2005.

[88] T. V. F. Abaya, M. Diwekar, S. Blair, P. Tathireddy, L. Rieth, and F. Solzbacher, “Deep-tissue light delivery via optrode arrays,” *J. Biomed. Opt.*, vol. 19, no. 1, p.

015006, Jan. 2014.

[89] D. M. Johnstone, C. Moro, J. Stone, A.-L. Benabid, and J. Mitrofanis, “Turning On Lights to Stop Neurodegeneration: The Potential of Near Infrared Light Therapy in Alzheimer’s and Parkinson’s Disease.,” *Front. Neurosci.*, vol. 9, no. January, p. Article 500, 2015.

[90] Q. Xia and T. Nyberg, “Inhibition of Cortical Neural Networks Using Infrared Laser,” *J. Biophotonics*, vol. 12, no. 7, Jul. 2019.

[91] Q. Xia and T. Nyberg, “Photothermal Inhibition of Cortex Neurons Activity by Infrared Laser,” *IFMBE Proc.*, vol. 68, no. 3, pp. 99–104, 2019.

[92] K. Podgorski and G. Ranganathan, “Brain heating induced by near-infrared lasers during multiphoton microscopy,” *J. Neurophysiol.*, vol. 116, no. 3, pp. 1012–1023, Sep. 2016.

[93] Z. Fekete, M. Csernai, K. Kocsis, Á. C. Horváth, A. Pongrácz, and P. Barthó, “Simultaneous in vivo recording of local brain temperature and electrophysiological signals with a novel neural probe,” *J. Neural Eng.*, vol. 14, no. 3, p. 034001, Jun. 2017.

[94] M. Kiss, P. Földesy, and Z. Fekete, “Optimization of a Michigan-type silicon microprobe for infrared neural stimulation,” *Sensors Actuators, B Chem.*, vol. 224, pp. 676–682, 2016.

[95] Á. C. Horváth *et al.*, “Infrared neural stimulation and inhibition using an implantable silicon photonic microdevice,” *Microsystems Nanoeng.*, vol. 6, no. 44, 2020.

[96] A. C. Horvath, C. O. Boros, O. Sepsi, S. Beleznai, P. Koppa, and Z. Fekete, “Optical characterization of an infrared neural optrode,” in *Symposium on Design, Test, Integration and Packaging of MEMS/MOEMS, DTIP 2018*, 2018, pp. 1–4.

[97] Á. C. Horváth, Ö. Sepsi, C. Ö. Boros, S. Beleznai, P. Koppa, and Z. Fekete, “Multimodal Neuroimaging Microtool for Infrared Optical Stimulation, Thermal Measurements and Recording of Neuronal Activity in the Deep Tissue,”

Proceedings, vol. 1, no. 4, p. 494, Aug. 2017.

[98] G. Buzsáki, C. A. Anastassiou, and C. Koch, "The origin of extracellular fields and currents-EEG, ECoG, LFP and spikes," *Nature Reviews Neuroscience*, vol. 13, no. 6. pp. 407–420, Jun-2012.

[99] S. Perel *et al.*, "Single-unit activity, threshold crossings, and local field potentials in motor cortex differentially encode reach kinematics," *J. Neurophysiol.*, vol. 114, no. 3, pp. 1500–1512, Sep. 2015.

[100] S. F. Cogan, "Neural Stimulation and Recording Electrodes," *Annu. Rev. Biomed. Eng.*, vol. 10, no. 1, pp. 275–309, Aug. 2008.

[101] Z. Fekete, Á. C. Horváth, Z. Bérces, and A. Pongrácz, "Black poly-silicon: A nanostructured seed layer for sensor applications," *Sensors Actuators, A Phys.*, vol. 216, pp. 277–286, Sep. 2014.

[102] N. A. Alba, Z. J. Du, K. A. Catt, T. D. Y. Kozai, and X. T. Cui, "In Vivo Electrochemical Analysis of a PEDOT/MWCNT Neural Electrode Coating," *Biosensors*, vol. 5, no. 4, pp. 618–646, 2015.

[103] W. Franks, I. Schenker, P. Schmutz, and A. Hierlemann, "Impedance characterization and modeling of electrodes for biomedical applications," *IEEE Trans. Biomed. Eng.*, vol. 52, no. 7, pp. 1295–1302, Jul. 2005.

[104] V. Sankar, E. P. R. Dieme, J. C. Sanchez, A. Prasad, and T. Nishida, "Electrode impedance analysis of chronic tungsten microwire neural implants: understanding abiotic vs. biotic contributions," *Front. Neuroeng.*, vol. 7, no. MAY, May 2014.

[105] H. Park, P. Takmakov, and H. Lee, "Electrochemical Evaluations of Fractal Microelectrodes for Energy Efficient Neurostimulation," *Sci. Rep.*, vol. 8, no. 1, Dec. 2018.

[106] J. C. Williams, J. A. Hippensteel, J. Dilgen, W. Shain, and D. R. Kipke, "Complex impedance spectroscopy for monitoring tissue responses to inserted neural implants," *J. Neural Eng.*, vol. 4, no. 4, pp. 410–423, Dec. 2007.

[107] Y. Nam, “Material considerations for in vitro neural interface technology,” *MRS Bull.*, vol. 37, no. 6, pp. 566–572, Jun. 2012.

[108] R. C. Gesteland, J. Y. Lettvin, B. Howland, B. Howland, and W. H. Pitts, “Comments on Microelectrodes,” *Proc. IRE*, vol. 47, no. 11, pp. 1856–1862, 1959.

[109] S. F. Lempka, M. D. Johnson, M. A. Moffitt, K. J. Otto, D. R. Kipke, and C. C. McIntyre, “Theoretical analysis of intracortical microelectrode recordings,” *J. Neural Eng.*, vol. 8, no. 4, p. 045006, Aug. 2011.

[110] J. B. Johnson, “Thermal agitation of electricity in conductors,” *Phys. Rev.*, vol. 32, no. 1, pp. 97–109, 1928.

[111] H. Nyquist, “Thermal agitation of electric charge in conductors,” *Phys. Rev.*, vol. 32, pp. 110–113, 1928.

[112] Ö. C. Boros *et al.*, “Optical and thermal modeling of an optrode microdevice for infrared neural stimulation,” *Appl. Opt.*, vol. 57, no. 24, pp. 6952–6957, 2018.

[113] L. B. Hunt, “The Origin of the Platinum Resistance Thermometer,” *Platin. Met. Rev.*, vol. 24, no. 3, pp. 104–112, 1980.

[114] T. 65/SC 65B IEC, “Industrial platinum resistance thermometers and platinum temperature sensors,” *IEC 60751 Int. Stand.*, 2008.

[115] H. E. Sostmann and J. P. Tavener, “Fundamentals of thermometry Part II,” *Isotech J. Thermom.*, 1990.

[116] H. E. Sostmann and J. P. Tavener, “Fundamentals of thermometry Part V,” *Isotech J. Thermom.*, 1992.

[117] NIMT, “Standard Procedure for Calibration of Industrial Platinum Resistance Thermometers,” *National Institute of Metrology (Thailand) Calibration Network Laboratories*, 2004. [Online]. Available: http://www.nimt.or.th/nimt/upload/linkfile/CalibrationProcedure/CP_No.401-IPRT_Calibration.pdf. [Accessed: 17-Dec-2015].

[118] E. A. Clement, A. Richard, M. Thwaites, J. Ailon, S. Peters, and C. T. Dickson, "Cyclic and Sleep-Like Spontaneous Alternations of Brain State Under Urethane Anaesthesia," *PLoS One*, vol. 3, no. 4, p. e2004, Apr. 2008.

[119] J. E. Ferguson, C. Boldt, and A. D. Redish, "Creating low-impedance tetrodes by electroplating with additives," *Sensors Actuators, A Phys.*, vol. 156, no. 2, pp. 388–393, Dec. 2009.

[120] C. Boehler, T. Stieglitz, and M. Asplund, "Nanostructured platinum grass enables superior impedance reduction for neural microelectrodes," *Biomaterials*, vol. 67, pp. 346–353, Oct. 2015.

[121] M. Chamanzar, M. Borysov, M. M. Maharbiz, and T. J. Blanche, "High-density Optrodes for Multi-scale Electrophysiology and Optogenetic Stimulation," in *Proc. Annu. Int. Conf. IEEE Eng. Med. Biol. Soc.*, 2014, pp. 6838–6841.

[122] S. Kisban, P. Janssen, S. Herwik, T. Stieglitz, O. Paul, and P. Ruther, "Hybrid microprobes for chronic implantation in the cerebral cortex.," *Conf. Proc. IEEE Eng. Med. Biol. Soc.*, vol. 2008, pp. 2016–2019, 2008.

[123] J. M. Cayce, R. M. Friedman, E. D. Jansen, A. Mahavaden-jansen, and A. W. Roe, "Pulsed infrared light alters neural activity in rat somatosensory cortex in vivo," *Neuroimage*, vol. 57, no. 1, pp. 155–166, 2011.

[124] K. Shibasaki, M. Suzuki, A. Mizuno, and M. Tominaga, "Effects of body temperature on neural activity in the hippocampus: regulation of resting membrane potentials by transient receptor potential vanilloid 4," *J. Neurosci.*, vol. 27, no. 7, pp. 1566–1575, Feb. 2007.

[125] T. Hedrick and J. Waters, "Spiking patterns of neocortical L5 pyramidal neurons in vitro change with temperature," *Front. Cell. Neurosci.*, no. JANUARY, pp. 1–6, Jan. 2011.

[126] D. Radzicki *et al.*, "Temperature-sensitive Cav1.2 calcium channels support intrinsic firing of pyramidal neurons and provide a target for the treatment of febrile

seizures.,” *J. Neurosci.*, vol. 33, no. 24, pp. 9920–31, Jun. 2013.

[127] J. A. Kim and B. W. Connors, “High temperatures alter physiological properties of pyramidal cells and inhibitory interneurons in hippocampus,” *Front. Cell. Neurosci.*, vol. 6, p. 27, Jul. 2012.

[128] J. I. Hurtado-Zavala *et al.*, “TRPV1 regulates excitatory innervation of OLM neurons in the hippocampus,” *Nat. Commun.*, vol. 8, Jul. 2017.

9 Appendices

9.1 Comparison of phase plot of recording sites' impedance before and after electroplating

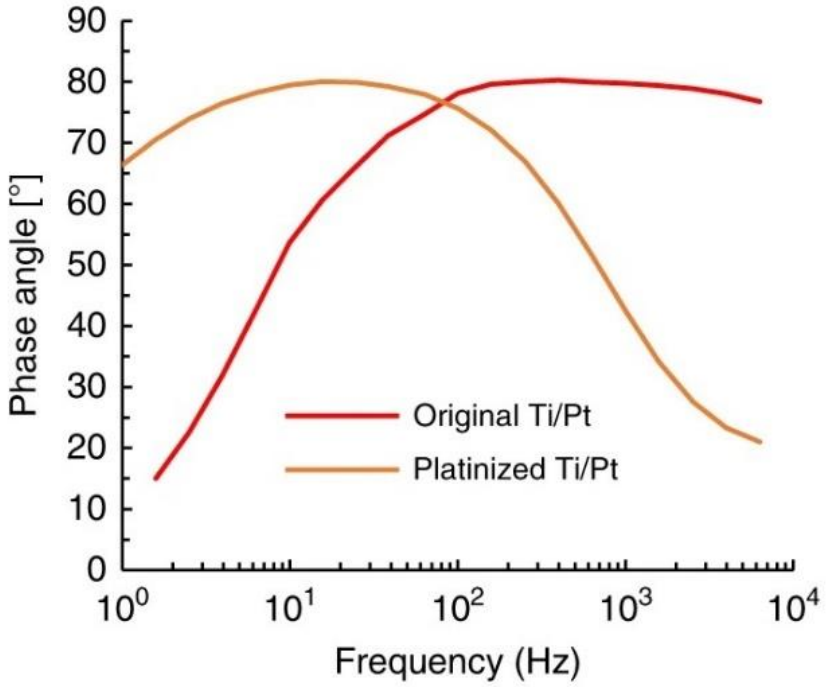

Figure 62: Phase characteristics of the electrophysiological recording sites recorded during EIS tests before (red) and after (yellow) porous Pt deposition. [95]

9.2 List of acronyms

- AC: alternating current
- ChR-2: channelrhodopsin-2
- CMOS: complementary metal-oxide semiconductor
- CVD: chemical vapour deposition
    - APCVD: CVD at normal ambient air pressure
    - LPCVD: low-pressure CVD
- CW: continuous wave
- DBS: deep brain stimulation
- DRIE: deep reactive ion etching
- EIS: electrochemical impedance spectroscopy
- FWHM: full width at half maximum

- ICP: inductively coupled plasma
- INS: infrared neural stimulation
- IR: infrared
- ITO: Indium tin oxide
- KOH: potassium hydroxide
- LED: light emitting diode
- LFP: local field potential
- MEMS: micro electro-mechanical systems
- MOA: micro-optoelectrode array
- NA: numeric aperture
- NTC: negative temperature coefficient
- PBS: phosphate buffered saline
- PCB: printed circuit board
- PD: Parkinson's disease
- PMMA: poly(methyl methacrylate), also known as acrylic, acrylic glass, or plexiglass
- PSTH: peri-stimulus time histogram
- RCNS: Research Centre for Natural Sciences
- RMS: root mean square
- RTD: resistance temperature detector, resistance thermometer
- Sccm: standard cubic centimetres per minute (cm^3/min), a flow measurement term
- SEM: scanning electron microscope
- SNR: signal-to-noise ratio
- SRC: spike rate changes
- TMS: Transcranial magnetic stimulation
- USEA: Utah Slant Electrode Array